UNIVERSITÉ DE STRASBOURG

ÉCOLE DOCTORALE Mathématiques, Sciences de l'information et de l'ingénieur

Laboratoire des sciences de l'ingénieur, de l'informatique et de l'imagerie

THÈSE présentée par :

Tianyan HAN

soutenue le : **30 Novembre 2017**

pour obtenir le grade de : **Docteur de l'université de Strasbourg**

Discipline/ Spécialité : Physiques des semi-conducteurs et dispositifs organiques

Bulk heterojunction solar cells based on solution-processed triazatruxene derivatives

THÈSE dirigée par :
  M. HEISER Thomas   Professeur, université de Strasbourg, France

RAPPORTEURS :
  Mme. LUDWIGS Sabine   Professeur, université de Stuttgart, Allemagne
  M. LMIMOUNI Kamal   Professeur, université de Lille 1, France

AUTRES MEMBRES DU JURY :
  M. ULRICH Gilles   Directeur de recherches, université de Strasbourg, France

谨以此文，致我的父母。
To my parents

ACKNOWLEDGEMENTS

I would like to express my gratitude to those who have helped, supported and accompanied me during last three years in ICube.

I would like to sincere thank my supervisor Professor Thomas HEISER for offering me the opportunity to pursue my PhD research in ICube and providing me the guidance and invaluable suggestions throughout my PhD study. I could not finish this thesis without him. He kindly helped me improve my scientific skills and his positive attitude always encouraged me.

I would also like to thank Dr. Patrick Levêque, for sharing his vast knowledge with me, offering valuable help in my writings, and giving enormous support on the charge transport measurements.

Thanks to all my colleagues in ICube: Dr. Sadiara Fall for useful discussions on charge carrier transport and for coffee hours, Dr. Olzhas Ibraikulov for the discussion in scientific and help not only in my work but also in my daily life, Dr. Thomas Regrettier, who finished PhD almost at the same time with me, for his help in capacitance measurements and for all the papers he send to me. As well as Dr. Emilie Steveler for discussions and support.

I also want to thank the technical staff in the lab: Nicolas Zimmermann, Stephan Roques, Sebastian Schmitt, Nicolas Colin and Florent Dietrich for their

Tianyan HAN

Bulk heterojunction solar cells based on solution-processed triazatruxene derivatives

Résumé

La conception de cellules solaires organiques de type hétérojonction en volume a été proposée pour la première fois en 1990. Ces dispositifs sont composés d'un mélange de polymères conjugués, donneurs d'électrons, et de fullerènes, accepteur d'électrons, et ont pour la première fois permis d'atteindre un rendement de conversion énergétique significatif (de l'ordre de 2%) avec des semi-conducteurs organiques. Dans ce contexte, cette thèse a porté sur l'étude approfondie d'une série de molécules donneurs d'électrons de forme d'haltère, dont le groupement planaire est l'unité triazatruxène (TAT) et le cœur déficient en électrons le thienopyrroledione (TPD). Les molécules de cette série se différencient par la nature des chaînes alkyles, attachées à l'unité centrale et aux unités TAT. Plus précisément, la relation entre la nature des chaînes latérales et les propriétés moléculaires et thermiques de ces molécules en forme d'haltère ont été étudiées en détail. L'impact des chaînes alkyles sur la morphologie en film mince à l'échelle nanométrique a également été étudié. Afin de mieux comprendre l'influence de la microstructure des films minces (constitués soit uniquement des molécules donneuses soit de mélanges molécules/fullerènes), le transport de charge dans le plan du film et perpendiculairement au plan ont été mesurées en fonction de la phase (amorphe, cristalline, …) du matériau. Des cellules solaires BHJ en mélange avec le dérivé de fullerène ont également été réalisées.

Mot-clé : cellules solaires organiques, transport de charges, semi-conducteurs organiques, transistors organiques à effet de champ, diodes à courant limité à charge spatiale

Résumé en anglais

The prospective conception of electron-donor/electron-acceptor (D/A) bulk heterojunction solar cells was first reported in 1990s, which blended the semiconducting polymer with fullerene derivatives, enhancing the power conversion efficiency. Since then, interests on this domain has been increasing continuously, and the efficiencies of BHJ solar cells have been increased dramatically. In this context, this thesis focuses on the study of a series of dumbbell-shaped small molecule donors, based on a highly planar unit called triazatruxene. The only difference between those molecules is the side-chains attached to central units and TAT units. As a consequence, the relationship between side chains nature and optoelectronic and structural properties of our TAT-based dumbbell-shaped molecular architecture will be investigated in detail. The impact of the alkyl chains on the molecular and thin film properties was also studied, with a particular emphasis put on microstructure and charge transport aspects. In-plane and out-of-plane charge carrier transport, with pure molecules and blend with fullerene, are measured in different systems. BHJ solar cells in blend with fullerene derivatives were also realized.

Keywords: organic solar cells, charge transport, organic semiconductors, organic field-effect transistors, space-charge-limited-current diodes

Contents

List of variables and abbreviations

A	Electron acceptor
Abs	Absorption
A/D	Acceptor/Donor Interface
A:D	Donor:Acceptor mixture
AFM	Atomic Force Microscopy
Ag	Silver
Al	Aluminum
ANR	Agence National de la Recherche
Au	Gold
AM1.5G	The global standard spectrum
BHJ	Bulk heterojunction
BODIPY	Bore-dipyromethene
C_{60}	Fullerene-60
C-AFM	Conductive-Atomic Force Microscopy
C_i	Capacitance of gate dielectric in OFET
CV	Cyclic Voltammetry
D	Electron donor
D_{col}	Lateral spacing of TAT columns
DBP	Tetraphenyldibenzoperiflanthen

DIO	1,8-diiodooctane
DSC	Differential Scanning Calorimetry
DOS	Density of states
Ea	Activation energy
EA	Electron affinity
E_g	Band gap energy
E_{ox}	Potential of oxidation
E_{red}	Potential of reduction
ETL	Electron Transport Layer
FF	Fill Factor
GIWAXS	Grazing Incidence Wide-angle X-ray Scattering
h	Plank constant
HTL	Hole Transport Layer
HMDS	Hexamethyldisilazane
HOMO	Highest Occupied Molecular Orbital
I_{ds}	Drain current
L_D	Exciton diffusion length
IP	Ionization potential
ITO	Indium Tin Oxide
J	Current density
J_m	Current density of point of maximum power
J_{sc}	Short circuit current density
k	Boltzmann constant
L	Thickness of active layer
LUMO	Lowest Unoccupied Molecular Orbital
MoO_3	Molybdenum trioxide
oDCB	Orth-dichlorobenzene
OFET	Organic Field Effect Transistor
p_o	Charge density
P3HT	Poly(3-hexylthiophene)
PCBM	[6,6]-phenyl-C61-butyric acid methyl ester
PCE	Power Conversion Efficiency
PEDOT:PSS	Poly(3,4-ethylenedioxythiophene) polystyrene sulfonate

P_{in}	Power of incident light
P_m	Point of maximum power
R_C	Contact resistance
R_{ch}	Channel resistance
R_{total}	Total resistance
S	Surface of single solar cell
SAXS	Small-Angle X-ray Scattering
SCLC	Space-Charge-Limited-Current
Si	Silicon
SiO_2	Silicon oxide
SVA	Solvent vapor annealing
T	Temperature
TAT	Triazatruxene
T_{iso}	Temperature of isotropic state
TLM	Transfer Line Method
UV	Ultra-Violet
V_{ds}	Drain voltage
V_{gs}	Gate voltage
V_m	Voltage of point of maximum power
V_{th}	Threshold voltage
V_{oc}	Open circuit voltage
W	Channel width
ZnO	Zinc oxide
ε_o	Vacuum permittivity
ε_r	Relative permittivity
η	Power Conversion Efficiency
λ	Wavelength
μ	Charge carrier mobility
μ_o	Mobility at infinite temperature
μ_{lin}	Linear mobility of OFET
μ_{sat}	Saturation mobility of OFET
σ	Conductivity
γ	Corrective factor
ξ	Correlation length from Scherrer formula

CHAPTER 1
Introduction

1.1 General introduction

Fast economy development, along with the explosive growth of population, has led to a huge energy demand. The International Energy Agency (IEA) reported that in 2014 the total final consumption by fuel was 9425 Mtoe[a]. Among all the energy sources, fossil fuels like oil, natural gas and coal account for 66.4 %[1]. The release of greenhouse gases attributed to the over-consumption of fossil fuels has been considered as one of the main causes of global warming and climate change. In addition, fossil fuels are finite resources, once we use them up, the world will fall into crisis. Nuclear power, another widely used energy source, can reduce carbon emission, however, it requires very careful management of the nuclear plant and nuclear waste, to avoid severe threats to human life. In 2011, the nuclear disaster in Fukushima has led to over 100,000 people evacuated from their hometowns and tons of contaminated water flowing into the Pacific Ocean. Even today, six years after the accident, impacts of nuclear waste still

---

[a] Mtoe stands for Million tonnes of oil equivalent, and 1 toe equals to 11.63 MWh.

remain in the east Japan. Therefore, tremendous efforts have been devoted to the development and employment of clean and renewable energy technologies, such as solar energy, wind power, hydropower and geothermal energy, etc.

Solar energy is an attractive alternative energy source, because it converts electricity directly by using solar cells, without either producing greenhouse gases or requesting huge power plants. Another advantage of using solar energy is that, the amount of energy provided by the sun per hour to the earth, satisfies the human uses for a whole year.

The process that generates electricity by absorbing light is called photovoltaic effect and was first observed by Alexandre-Edmond Becquerel in 1839[2]. However, the first useable solar cell was fabricated at Bell's lab only in 1954[3]. Since then, more and more researchers put their efforts into the photovoltaic technology, and designed many types of solar cells, such as silicon, perovskite, dye sensitized, and organic cells. These solar cells can be divided into two catalogues: inorganic and organic. The current solar cell industry is dominated by inorganic solar cells, especially silicon-based solar cells. They have already reached a power conversion efficiency (PCE) of 34 % (GaAs thin film cell), which is the highest efficiency for single-junction terrestrial solar cells to date[4]. However, electricity supply by inorganic solar cells is still limited by their prohibitive prices, rigidity and fragility drawbacks.

As compared to inorganic solar cells, the organic solar cells, which are relatively new, possess several advantages. First of all, organic semiconductors are inexpensive and can be processed by printing, which further lowers the fabrication cost. In addition, the light-weight, semi-transparency and flexibility suit them more than conventional silicon solar cells to some applications, such as portable cellphone modules, and those where the cells are needed to be attached to windows or curved surfaces, *etc*.

There are several different types of organic semiconductors among which the π-conjugated polymers are the most widely investigated ones. They were first synthesized by Hideki Shirakawa, Alan G. MacDiarmid and Alan J. Heeger in 1977, three winners of the Nobel Prize in Chemistry in 2000[5]. In 1995, Alan J.

Heeger reported a prospective conception of the so-called electron-donor/electron-acceptor (D/A) bulk heterojunction, which blends semiconducting polymers with C_{60} (buckminsterfullerene) or its functionalized derivatives, enhancing the efficiency dramatically[6]. Through efforts into the molecular design, processing techniques enhancement, morphology control and device architecture improvement in the last two decades, polymer-based solar cells have achieved a PCE over 13 % for laboratory single-junction cells[7].

Compared to polymers, π-conjugated small molecules are also promising for the photovoltaic technology. The PCE of small molecule solar cells has been increasing continuously over the last decade and has recently reached the benchmark value of 11% with a single D/A bulk heterojunction (BHJ)[8,9]. Although the solar cells based on solution-processed small molecules are still less efficient than polymer-based cells, they in principle have several distinctive advantages, such as better control of the molecular structure, easier purification and accordingly lower batch-to-batch variations. Optimization of the chemical structure of the photon absorbing molecules has been a key to this successful endeavor.

1.2 The project ORION

This thesis focuses on the photovoltaic application of soluble small molecules, and it is a part of the project ORION, which was co-funded by the Agence Nationale de la Recherche (ANR) and the Région Alsace. The name ORION stands for <efficient s**O**luble small molecules fo**R** photovolta**I**c applicati**ON**s>. This multidisciplinary project is being realized by the collaboration of different groups. The group of N. Leclerc from the ICPEES[b] designed and synthesized all the small molecules investigated in this thesis. Dr. B. Heinrich from the IPCMS[c]

---

[b] Institut de Chimie et Procédés pour l'Energie, l'Environnement et la Santé, Strasbourg, France

[c] Institut de Physique et Chimie des Matériaux de Strasbourg, Strasbourg, France

worked on structure analysis using Grazing-incidence wide angle X-Ray scattering (GIWAXS). And the group of T. Heiser from the ICube[d] is specialized in the elaboration and characterization of organic photovoltaic devices.

The objective of the project ORION is to improve the efficiency and the stability of organic solar cells by using bore-dipyromethene (BODIPY) and triazatruxene (TAT) derivatives as electron-donor material (shown in Figure 1-1). The BODIPY derivatives exhibit very high molar extinction coefficients and easily modifiable absorption spectra, which allow efficient photon absorption. And the TAT units exhibit both an optimal solubility due to the alkylation of indole, and a high planarity enabling efficient π-π stacking. In order to obtain a high efficiency, good solubility, wide absorption spectra, matched energy levels and efficient charge transport are essential features for organic semiconductors. Both BODIPY and TAT have been used as constituents of organic semiconductors for photovoltaic applications, and PCE values above 5% have already been obtained with bulk heterojunction devices, and we expect a PCE up to 9 % under optimized conditions[10–12]. Another goal of this project has been to understand the main factors that limit the efficiency of BODIPY and TAT platforms and to find ways to circumvent them.

As a part of this project, the objective of my thesis work is to improve the efficiency of TAT based small molecules solar cells through the investigation on their molecular structures and charge carrier transport, and understanding the relationships between the molecular structure and the molecular opto-electronic properties. Therefore, a series of TAT-based molecule donors with specific chemical structures (so-called dumbbell-shaped molecules) are in-depth studied. Their molecular and bulk material properties, thin-film properties, charge carrier transport and their applications in bulk heterojunction solar cells have been investigated. Particularly, the charge carrier

---

[d] Laboratoire des sciences de l'ingénieur, de l'informatique et de l'imagerie, Strasbourg, France

transport has been studied in detail, since it is a key factor limiting the performance of photovoltaic devices.

BODIPY

TAT
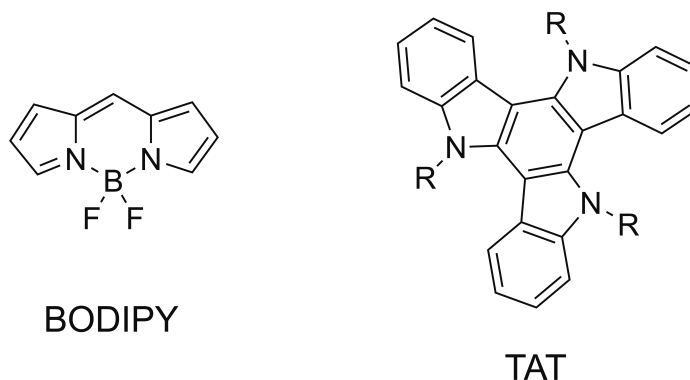
Figure 1-1 Chemical formula of BODIPY and TAT.

1.3 Thesis structure

Chapter 2 introduces the scientific background of organic semiconductors and organic solar cells. A detailed literature review is presented and key factors that influence the performance of organic solar cells are discussed.

In Chapter 3, a state-of-art of soluble electron donor small molecules is presented.

Chapter 4 details the molecules and experimental techniques used in this work.

Chapters 5 to 8 report the experimental results including molecular and bulk material properties, thin-film, charge transport and photovoltaic properties.

Chapter 9 summarizes this thesis and prospects future work.

CHAPTER 2
Scientific Background

This chapter will focus on the introduction of organic semiconductors and on the operation principles of organic solar cells. First, the physics of organic semiconductors are briefly introduced. The next section presents the detailed processes that converts solar energy into electrical energy. Different solar cell device structures are described as well. Then the characterization of organic solar cells and main parameters are recited. The chapter ends with presenting several methods that could promote the performance of the organic solar cells.

2.1 Organic semiconductors

The term "organic semiconductor" refers to organic materials that exhibit semiconducting behaviors. The first studies on organic semiconductors date bake to the early 20th century, when the photoconductivity of anthracene crystals was investigated[13]. Later, electroluminescence was discovered in the 1960's, which encouraged many researchers to investigate molecular crystals. In the 1970's, another important class of organic semiconductors, conjugated polymers, was successfully synthesized[14]. However, reasonably efficient photovoltaic performances could not be achieved until the demonstration of

bulk heterojunction solar cells that incorporated electron-donor and electron-acceptor materials in the 1990s[6].

The driving force to study devices based on organic materials comes from potential advantages over silicon or other traditional semiconductors: organic semiconductor devices can be fabricated with bottom-up approaches instead of top-down methods, and open the possibility to produce devices with reduced costs. Moreover, as the physical and electronic properties of organic semiconductors depend on factors like conjugation length or the presence of electron-donating or withdrawing groups, their optoelectronic properties can be tuned by chemical methods: the researchers can design and synthesize new organic semiconductors with desired properties [15,16].

2.1.1 Origin of semiconducting behavior

2.1.1.1 Electronic property

Organic semiconductors are also called π-conjugated materials, because their electronic and optical properties are caused by the π-orbitals of sp^2-hybridized carbon atoms. One carbon atom has six electrons, its ground-state electron configuration expresses as $1s^2 2p^2 2s^2$, where s and p represent the atomic subshells. The sp^2-hybridization leads to double covalent bonds between carbon atoms. In this case, three sp^2-orbitals are formed by mixing $2s$ with $2p_x$ and $2p_y$ orbitals, while one p_z-orbital remains unchanged. The three sp^2-orbitals are co-planar and point towards the corners of a triangle at an angle of 120°. The overlap of the sp^2-orbitals of two neighboring atoms forms a σ-bond. And the electrons in σ-bonds are localized along the axes bridging both atoms. One the other hand, the overlap of the remaining p_z-orbitals lead to delocalized π-molecular orbitals or π-bonds. An electron in this state is referred to as π-electron (illustrated in Figure 2-1a).

The distance between two neighboring atoms (in one π-conjugated molecule) changes periodically by a few percent due to the periodic distortion of molecular bond length. This situation is represented as an alternation between single and double bonds (as shown in Figure 2-1b), whereas an overlap of the π-orbitals

exists within all neighboring C atoms. Therefore, the conjugation of π-bonds gives rise to delocalized π-electron states that support intramolecular charge transport, and result in high electronic polarizability[17].
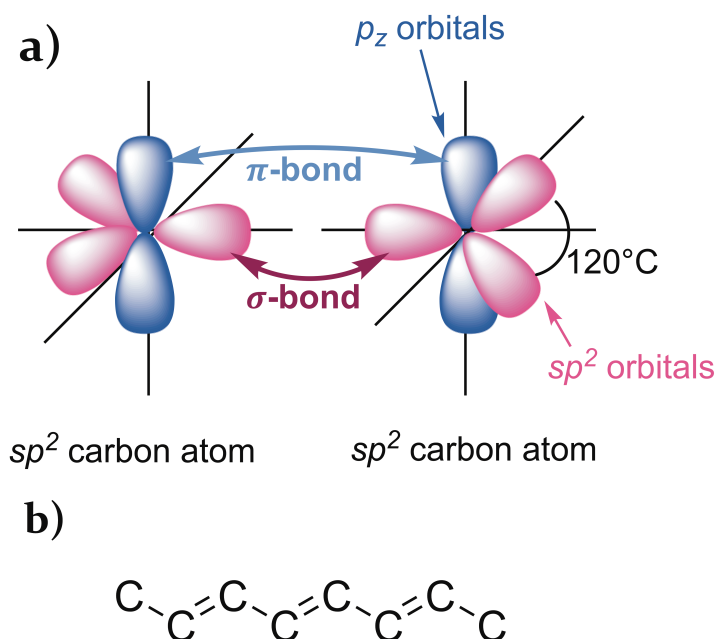
Figure 2-1: (a) two sp2 hybridized carbon atoms showing overlapping of *p* orbitals; (b) π-conjugated carbon chain: alternating single and double bonds.

2.1.1.2 Absorption property

According to the molecular orbital (MO) theory, the overlap of two p_z-orbitals forms two molecular orbitals: π-orbital and π*-orbital (shown in Figure 2-2). The electrons in the p_z orbitals are stabilized by occupying the lower energy π orbitals. In the ground state, the occupied orbitals are also known as bonding orbitals, whereas unoccupied orbitals are known as antibonding orbitals. The bonding orbitals have lower in energy than the antibonding orbitals.

The benzene molecule (C_6H_6) which includes 6 p_z and 18 sp^2 hybridized orbitals can be considered as an example. The 6 p_z orbitals form three occupied π molecular orbitals and three unoccupied π* molecular orbitals. At the same time, 18 sp^2 hybridized orbitals form nine occupied σ molecular orbitals and nine unoccupied σ* molecular orbitals. All the twelve bonding orbitals are fully occupied by 24 valence electrons (illustrated in Figure 2-2a). For more complex conjugated molecules (like conjugated polymers), the long chain of C atoms lead to more occupied and unoccupied molecular orbitals.

In the solid state, the energy bands corresponding to the occupied states are referred to as "Highest Occupied Molecular Orbital (HOMO) band" (or "Valence band"), and those corresponding to the unoccupied molecular orbitals are referred to as "Lowest Unoccupied Molecular Orbital (LUMO) band" (or "Conduction band") (Figure 2-2b). The HOMO and LUMO bands are characterized by two key parameters: the electron affinity (*EA*) and the ionization potential (*IP*). *EA* is the amount of energy released when an electron transfers from vacuum to the lowest energy level in the conduction band, and *IP* is defined as the least energy spent to release an electron from the LUMO band. The energy gap between the HOMO and LUMO bands is generally close to the optical energy band gap (Eg), which can be estimated from the optical absorption measurements edge. However, this approximation does not take into account the exciton binding energy (see §2.2.1). Under illumination, photons with energy higher than E_g can be absorbed by exciting electrons from the LUMO band to the HOMO band. For π-conjugated molecules, E_g is generally low enough for photons of the visible light to be absorbed (i.e. Eg of an organic semiconductor is typically below 3 eV).
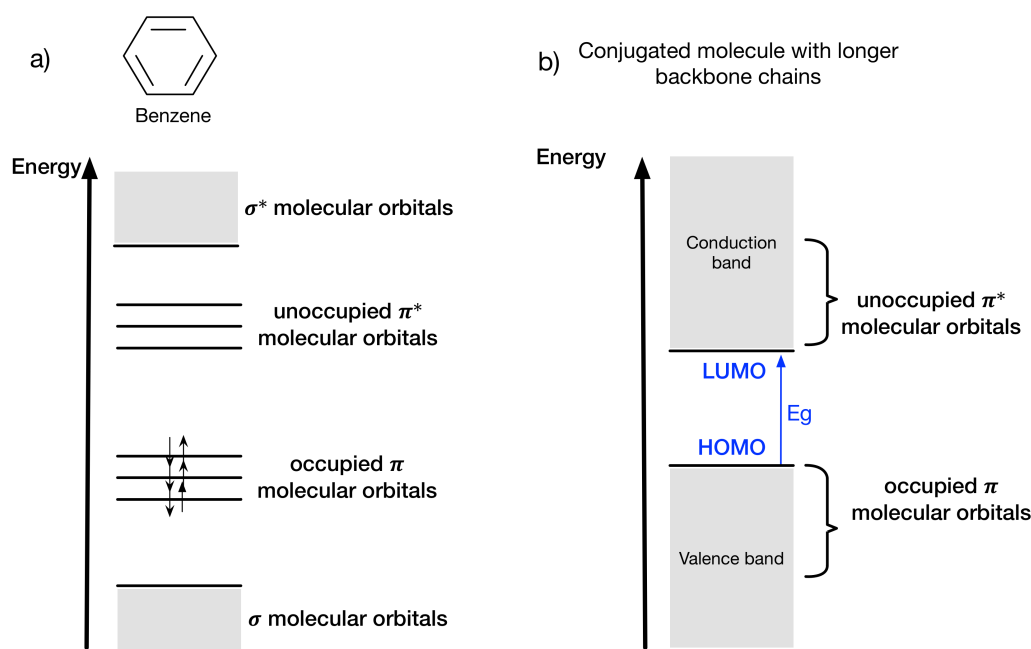
Figure 2-2: Diagram of the molecular orbitals of a π-conjugated molecule. The electron at HOMO will excite to LUMO when it absorbs energy higher than E_g.

2.1.2 Different types of organic semiconductors

There are two major classes of organic semiconductors: polymers and small molecules. Generally speaking, small molecules have lower molecular weight than polymers and they are mono-disperse[18]. At present, polymeric semiconductors are the most widely investigated organic semiconductors and have already achieved over 13% efficiencies[7]. Solar cells based on solution-processed small molecules lag behind polymer-based solar cells in terms of PCE, but benefit in principle from several distinctive advantageous: better control of the molecular structure, easier purification and therefore lower batch-to-batch variations[19–21]. Figure 2-3 shows several examples of some important conjugated polymers and small molecular semiconductors.

Organic semiconductors are also often classified into "p-type" and "n-type" based on the relative location of their HOMO and LUMO bands. P-type semiconductors are electron-donor materials (D) and are characterized by relatively high lying LUMO and HOMO levels in comparison to N-type semiconductors.

The currently most widely used electron-acceptors for solar cells, are methyl [6,6]-phenyl-C61-butyrate, also called $PC_{61}BM$, and [6,6]-phenyl-C71-butyrate, named $PC_{71}BM$. Due to the symmetrical shape of C61 fullerene, $PC_{61}BM$ has a much weaker optical absorption coefficient than $PC_{71}BM$, Both fullerene derivatives often serve as a standard for testing electron donor materials.[22,23]

Polymers:

poly(3-hexylthiophene-2,5-diyl)
(P3HT)

polypyrrole

poly(*p*-phenylene vinylene)
(PPV)

Small molecules:

Copper(II) phthalocyanine
(CuPC)

Fullerene
(C_{60})

Pentacene
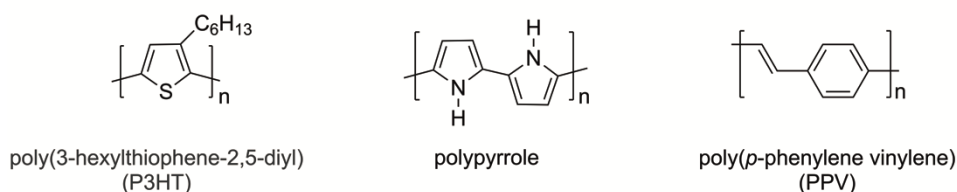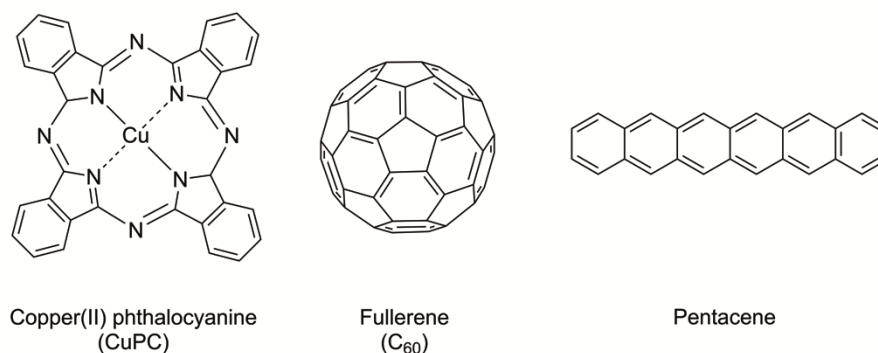
Figure 2-3: molecular structures of some prototypes of organic semiconductors.

2.2 Operating principles of organic solar cells

Organic solar cells are composed of a photo-active layer sandwiched between two electrodes with different work functions. The active layer is formed of an electron donor material (D) and an electron acceptor material (A). Both organic semiconductors are differentiated by their respective frontier orbital energy positions: the molecule possessing the lowest ionization potential is referred to as the electron donor (it has a higher HOMO level). On the contrary, the electron-accepting molecule corresponds to the organic semiconductor having the lowest LUMO level and therefore highest electronic affinity. There are several architectures of the active layer, which will be discussed in more detail in section 2.3.

Converting solar energy into electricity includes five steps (summarized in Figure 2-4):

1) Light absorption and exciton generation;
2) Exciton diffusion to donor/acceptor interface;
3) Exciton dissociation;

4)   Free charge transport or charge recombination;

5)   Charge collection at the electrode.

Each process involved in the photovoltaic effect will be discussed in more detail below.
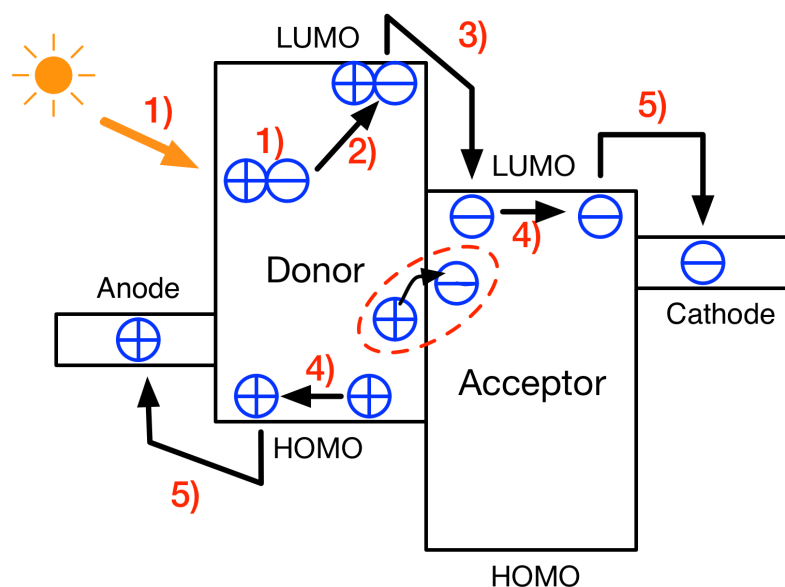
Figure 2-4: Energy level diagram of donor and acceptor in an organic solar cell: six steps of photovoltaic effect.

2.2.1 Light absorption and exciton generation

The first step is to absorb light by the semiconducting layer, leading to the generation of singlet excitons (see Figure 2-4 step 1). The generation of excitons occurs only when photons with energy equal to or higher than the optical band gap of the organic semiconductor are absorbed. As mentioned in section 2.1.1, the energy band gap of organic semiconductors must be below 3 eV to absorb in the visible to near infra-red spectrum. Moreover, according to Shockley-Queisser theory, the optimal energy band gap for single junction solar cells is around 1.3 eV for a theoretical maximum efficiency of 33%[24] (shown in Figure 2-5).
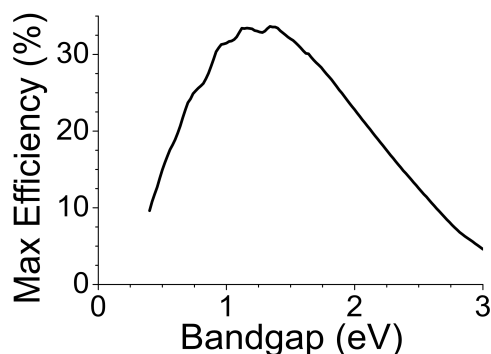
Figure 2-5: The Shockley-Queisser limit for the efficiency of a solar cell. Adapted from https://en.wikipedia.org/wiki/Shockley–Queisser_limit

Organic semiconductors have often very high absorption coefficients in comparison to inorganic semiconductors and can exceed 10^5 cm^{-1}. Thus, the photo-active layer can be as thin as 100 – 200 nm and still ensure sufficient light absorption[17].

Excitons can be considered as strongly bounded electron-hole pairs, which cannot be separated due to the poor screening of the strong coulombic interactions (low dielectric constant). The excitons can be divided into Wannier-Mott or Frenkel types depending on the properties of medium materials. For the materials with high dielectric constants (inorganic semiconductors, $\varepsilon_r > 10$), the binding energy is low (in the order of 0.01 eV), such excitons are called Wannier-Mott excitons[25]. In crystalline silicon for example, the electron-hole binding energy is as low as 14 meV. On the other hand, in the materials of low dielectric constant, such as organic semiconductors, ε_r is around 3 and the exciton binding energy is significantly larger, of the order of ~0.3-0.5 eV. This kind of exciton is noted as Frenkel excitons. The thermal energy at room temperature (~26 meV) is insufficient to separate the electron-hole pair.

2.2.2 Exciton diffusion and dissociation

During the short lifetime of photo-generated excitons (in the range of nanoseconds), they may diffuse towards the donor/acceptor interface (see Figure 2-4 step 2), and dissociate into free charges through a charge transfer process at the D/A interface. The transfer process is induced by the energy offsets between the LUMO bands and HOMO bands (HOMO$_D$ – HOMO$_A$).

When an exciton generated in the D material reaches the D/A interface, it may transfer the excited electron to the acceptor molecule, since the latter provides an energetically favorable environment, whereas the hole remains on the electron donor. This phenomenon is called intermolecular charge transfer (CT). This process is ultrafast, on the order of tens of femtoseconds (fs) and competes efficiently with exciton recombination (that takes place in the ns range). For instance, for the most used donor:acceptor combination Poly(3-hexylthiophene):$PC_{61}BM$ (or P_3HT:$PC_{61}BM$), the charge transfer process has been reported to take place in less than 120 fs[26,27]. To guarantee that excitons can reach the D/A interface, the exciton diffusion length L_D must be long enough (of the order of the average domain size). L_D of organic semiconductors are typically in the range of 5-20 nm[28-34]. For structurally ordered organic semiconductors, L_D can be very high[28]. For instance, L_D values as high as 68 nm have been reported for copper phthalocyanine (CuPc) derivatives.[32]

After a successful charge transfer progress, electrons and holes reside on different molecules. However, they are still Coulomb bounded. Although less strongly bounded as the initial exciton, the charge transfer state has to be separated to participate to the photocurrent. To date, the physical origin that allows for the very efficient charge generation observed experimentally, is still under discussion. An in-depth review of charge generation in donor-acceptor blends can be found in reference [35-37].

2.2.3 Charge transport

After the dissociation of excitons, the separated charges can drift or diffuse towards the respective electrodes (see Figure 2-4 step 4). The latter are characterized by their respective work functions, which in turn depend on the Fermi-level (or chemical potential) position in the metal. When a solar cell system is in thermal equilibrium, it tends to get the chemical potentials to be the same across the whole system. Therefore, the system will tend to have some charge redistribution increasing the chemical potential of anode while decreasing the potential of cathode. As a result, a built-in electrical field

appears, which will make photo-generated electrons and holes drift towards the cathode and the anode, respectively.

In crystalline inorganic semiconductors with 3D crystal lattice, the atoms are strongly coupled via covalent bonds, that form the conduction band (CB) and valance band (VB). The charge carriers are in delocalized states and their transport is characterized by high mobility values (above 1 cm²/Vs). Such charge carrier transport is called band transport mechanism[38,39] and shows a temperature dependence which follows a power law :

$$\mu \propto T^{-n} \quad with\, n = 1 \dots 3 \qquad\qquad (\,2\text{-}1\,)$$

One the other hand, the intermolecular interactions of organic semiconductors are weak van der Waals forces and charge carriers are generally highly localized. The charge carrier transport occurs mostly by hopping between localized states, whose density of the states (DOS) is often described by Gaussian distribution (Figure 2-6).[40–42].

The mobility determines the drift velocity of charge carriers under an electric field and is an important factor influencing the performances of solar cells. If the mobilities are too low, electron-hole recombination limits the charge collection and leads to poor power conversion efficiency. The charge carrier mobilities of organic semiconductors are often lower than 10^{-3} cm^{-2} V^{-1} s^{-1}, which is orders of magnitude less than the mobilities of crystalline inorganic semiconductors (1 to 10^4 cm^{-2} V^{-1} s^{-1})[43–45]. Instead of a power law temperature dependence, they show an activated behavior which follows the Arrhenius expression:

$$\mu \propto exp(-\frac{E_a}{kT}) \qquad\qquad (\,2\text{-}2\,)$$

where E_a is the activation energy and k is the Boltzmann constant.

In organic semiconductors, the hopping transport is highly influenced by the intermolecular interactions and structural order.
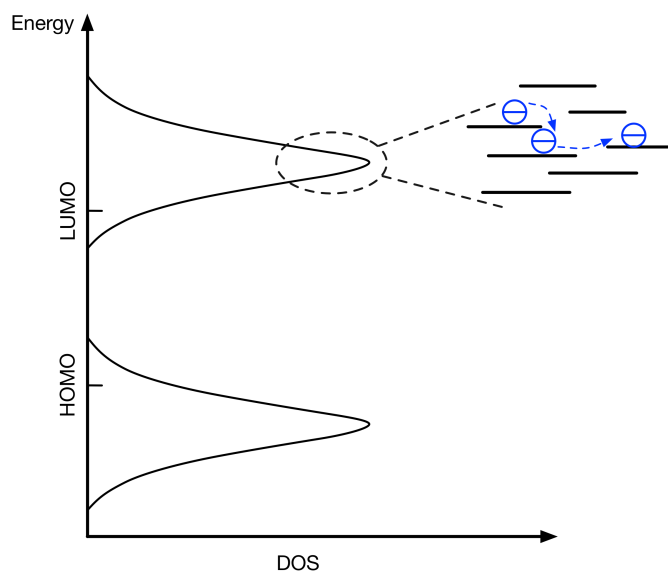
Figure 2-6: Gaussian Density of States and charge carriers transport by hopping.

2.2.4 Charge-carrier recombination

When charge transport is not efficient, opposite charges may recombine, leading to poor solar cells performances (see Figure 2-4 step 5).

Two different processes of charge-carrier recombination can be distinguished. If the charge transfer state (i.e. the still bound electron-hole pair generated after exciton dissociation) decays to the ground state before dissociation, this is considered as geminate recombination[46].

In contrast to geminate recombination, the non-geminate recombination refers to the recombination of electron and holes, which were created by different absorbed photons. The dissociated opposite charges recombine with each other on their way towards the electrodes. The amount of charges in the device depends on the external electrical field, thus, non-geminate recombination strongly depends on the applied voltage due to its impact on the current flow and charge carrier density. The studies on polymer and small molecule based solar cells have shown, that both non-geminate[47] and geminate losses[48,49] can have a strong impact on the device performance, depending mainly on the photoactive material.

Non-geminate recombination of free charge carriers in materials with low mobility can be described with the Langevin recombination rate, established by Paul Langevin in 1903[46]. The recombination rate R is given as:

$$R = \gamma n p \qquad (2\text{-}3)$$

where n, p are the electron and hole concentrations, and γ is the Langevin recombination constant.

$$\gamma = \frac{q}{\varepsilon}(\mu_e + \mu_h) \qquad (2\text{-}4)$$

where q is the elementary charge, ε represent the effective dielectric constant and μ_e, μ_h the mobility of electrons and holes respectively.

Non-geminate recombination is found to be one of the limiting factors of the open-circuit voltage[50,51], and the fill factor[52] of many solar cells. However, charge recombination is still not fully understood, and further investigations are needed to reduce these losses in solar cells.

2.2.5 Charge extraction

Finally, the photo-generated charges are extracted at the electrodes (see Figure 2-4 step 6).

The free charges will be collected by their respective electrodes to complete the process of solar energy conversion. As presented in the previous section, the electrons will be collected at the cathode and holes will be collected at the anode because of the built-in electrical field. Moreover, at the maximum power point, the electrical field is very low, and carrier diffusion has also a very strong impact on charge collect. Therefore, selective electrodes, which favor either electron transfer or hole transfer, are needed and presented below.

The selection of electrode materials is crucial for charge extraction. The electrode materials must have a proper work-function which needs to be close to the HOMO level of the electron donor material and the LUMO level of the acceptor material, respectively, and avoid the appearance of an energy barrier Φ.

A large barrier Φ lowers the extraction rate, leads to charge accumulation near the contact, and results in a low fill factor (FF) and low device performance[53,54]. Electrode materials for the anode (electron collecting contact) of organic solar cells require low work-function, such as Aluminum (Al), Calcium (Ca). Whereas for the cathode (hole collecting contact), materials with high workfunction like silver (Ag) and gold (Au) are preferred. Bottom electrodes have to be transparent, or at least partly transparent for the good light absorption. Therefore, transparent conducting layers like Indium Tin Oxide (ITO), comprising 90% Indium oxide (In_2O_3) and 10% Tin oxide (SnO_2) with a large bandgap of 3.7 eV and workfunction of 4.4 – 4.9 eV are used. ITO on glass or plastic substrates, covered by a thin hole transport layer such as Poly(3,4-ethylenedioxythiophene):poly(4-styrenesulfonate) (or PEDOT:PSS), is widely used as electrodes.[55,56].

When the solar cell operates at the maximum power point condition, the build-in electric field is significantly reduced, increasing the risk that the charges are collected at the wrong electrodes.[57]. To overcome this issue, an electron transport layer (ETL) and/or a hole transport layer (HTL) are used as interlayers between the active layer and the respective electrodes. ETL has a high electron affinity and high electron mobility, it allows electrons to flow across the layer, while holes cannot pass through. On contrast, HTL allows holes to flow through while electrons cannot pass[37,58–60]. Thus, charge extraction efficiency is increased and bimolecular recombination is reduced at the electrodes. PEDOT:PSS is the most commonly used organic hole transport layer, other materials, such as oxides (i.e. Molybdenum trioxide or MoO3), also have potential for anode interlayer. On the other hand, oxides like Zinc oxide (ZnO) and Titanium oxide (TiO_x), and organic interlayer such as 80% ethoxylated polyethylenimine (PEIE) are excellent electron transport layer materials.

2.3 Device structure and active layer architectures of organic solar cells

2.3.1 Device structures

The two most investigated structures of organic solar cells: the standard structure and the inverted structure are shown in Figure 2-7. In the standard structure, electrons are collected at the top electrode and holes are collected at the transparent ITO/glass substrate. Thus, metals with low work-function like Al or Ca/Al, are used as top electrodes. These metals are however easily oxidized in air resulting in poor device stability (in the absence of efficient encapsulation). PEDOT:PSS is commonly used as HTL between ITO and active layer. It blocks electrons and reduces the surface roughness of the ITO layer.

On the other hand, in an inverted structure, electrons are collected at the transparent conducting substrate and holes are collected at the top electrode. For devices with an inverted structure, the anode is on the top, so metals with a high work-function like Ag and Au are used, along with MoO_3 as the HTL. In this thesis, we use PEIE, a non-conjugated polymer bearing ionic groups (i.e. a poly-electrolyte), as ETL. It forms a layer of electrical dipoles that reduce the workfunction of ITO and turns ITO into cathode. It also blocks hole transfer efficiently, although the underlying mechanism is still poorly understood.
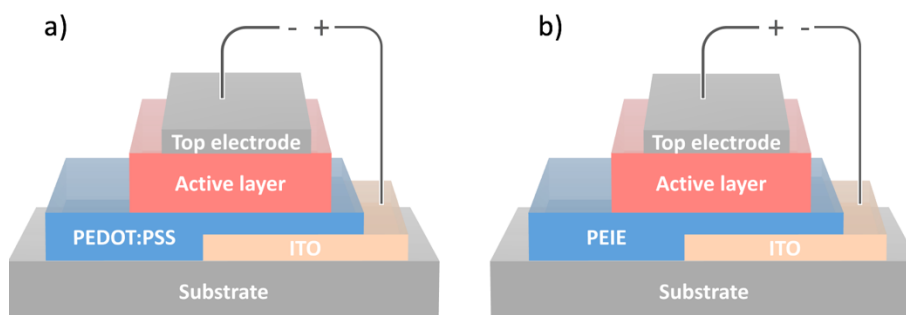
Figure 2-7: Solar cell with (a) standard structure and (b) inverted structure.

2.3.2 Active layer architectures

The basic structure of a photovoltaic device shown in Figure 2-7 above consists of an active layer sandwiched between two electrodes. In the following part, an overview of possible active layer architectures is presented.

2.3.2.1 Single layer structure

The first organic solar cells consisted of a single polymer layer sandwiched between two electrodes of different work function (simplified schematic shown in Figure 2-8a)[61–63]. As presented previously, because of the low exciton diffusion length and high binding energy in organic semiconductors, the charge dissociation only occurs at the interfaces between the active layer and the electrodes. As a result, the photovoltaic efficiency is quite low (PCE ~ 0.1 %)[64,65].

2.3.2.2 Bilayer structure

The limitation of poor charge dissociation was overcome by Tang's group in 1986 who introduced the concept of bilayer solar cell. The bilayer heterojunction architecture consists of an electron donor (D) layer and an electron acceptor (A) layer (shown in Figure 2-8b). In this case, exciton dissociation occurs at the D/A interface because of the energy offset of the frontier energy levels between donor and acceptor. At the same time, both electrons and holes diffuse to their respective electrodes in separated domains so that the recombination of the photo-excited charges is reduced. However, the photo-generation of charges is still limited because of the low D/A interface area.

Tang reported a bilayer heterojunction solar cell fabricated from copper phthalocyanine (CuPC) and a perylene tetracarboxylic derivative (PV). The structure of the cell was therefore as follow: ITO/CuPc/PV/Ag. A power conversion efficiency of about 1 % has been achieved with a fill factor as high as 0.65[66].

In the early 1990's, S. N. Sariciftci and A. J. Heeger demonstrated the transfer of ultra-fast photo-inducted electrons (on the order of the picosecond) in the solid state between a donor polymer, poly[2-methoxy-5-(2-ethylhexyloxy)-1,4-

phenylenevinylene] (MEH-PPV) and an acceptor fullerene, C_{60}. A two-layer system involving these two semiconductors allowed them to achieve the efficiency of 0,04%.[67] Just a year before, Yoshino et al. demonstrated the same type of phenomenon between poly (3-hexylthiophene) (P3HT) and C_{60}[67]. P3HT later became a standard electron-donor material.

2.3.2.3 Bulk heterojunction structure

A bulk heterojunction (BHJ) architecture consists of a blend of donor and acceptor materials for which spontaneous phase separation leads to a nanostructured morphology. Such a blend creates a bi-continuous interpenetrating network of D and A domains. Therefore, the D/A interface is increased and more excitons can be dissociated (Figure 2-8c)[6,68]. As a result, the power conversion efficiency increases. However, the bulk heterojunction devices are highly sensitive to the morphology of the active layer, which governs charge separation, recombination and transport.

Solution-processed BHJ solar cells were first reported by A. J. Heeger in 1995. They blended MEH-PPV with fullerenes derivative. The PCE increased by more than two orders of magnitude in comparison to a solar cell composed of pure MEH-PPV (single layer solar cell)[6]. Since this innovative work, the development of new organic semiconductors for BHJ applications has given rise to numerous studies. It is also with this bulk heterojunction architecture that the photovoltaic devices were realized in this thesis.
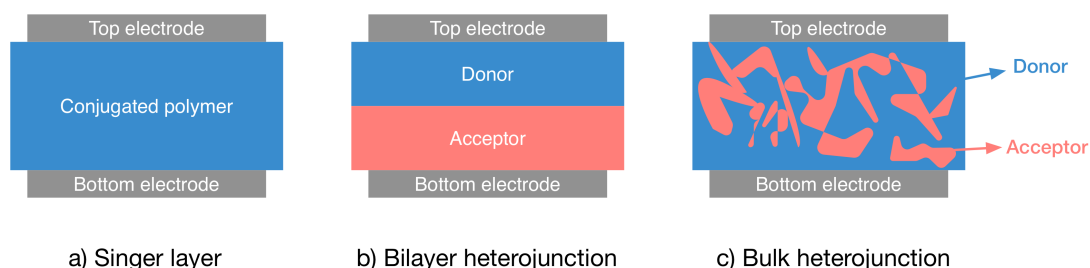
Figure 2-8: Simplified schematic of (a) single layer, (b) bilayer heterojunction and (c) bulk heterojunction architecture.

2.4 Characteristics of organic solar cells

Figure 2-9 shows a current-voltage (J-V) characteristic measured under dark and illumination of a solar cell investigated in this thesis. The main parameter that describes the performance of an organic solar cell is the power conversion efficiency (PCE), denoted as η. η is determined by the ratio between the useful electrical power output P_m and the power of incident light P_{in}.

$$\eta\ (\%) = \frac{P_m}{P_{in}} \qquad\qquad (\ 2\text{-}5\ )$$
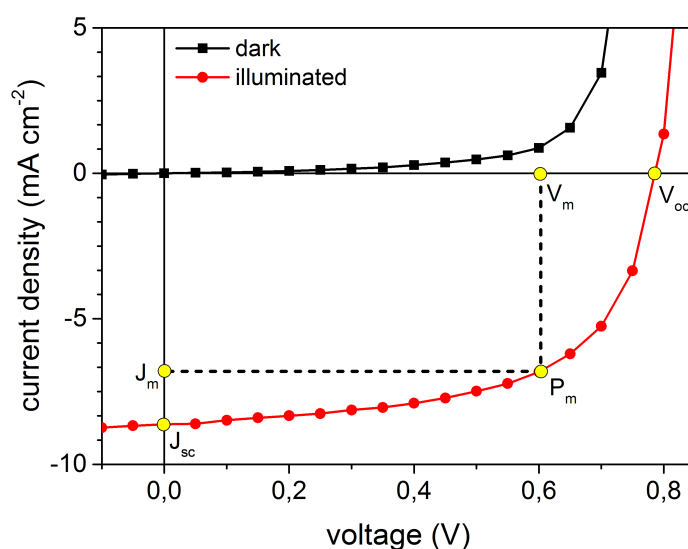
Figure 2-9 Dark and illuminated *J–V* characteristics of an organic solar cell investigated in this thesis. The point of maximum power (P_m), as well as the two characteristic parameters, the short circuit current density J_{sc} and the open circuit voltage V_{oc} are marked in yellow.

The parameters that influence the efficiency are:

i) J_{sc}.

J_{sc} represents the current density obtained by solar cells under short circuit condition (V= 0 V). It is determined by the amount of charge carriers that are collected at the electrodes, hence, it is also related to the number of photons absorbed in active layer. Optimization of the light absorption can increase J_{sc}. Another factor than can influence J_{sc} is the morphology of the active layer, since both the surface of D/A interface and the domain size have an impact on the amount of photo-generated charge carriers.

ii) V_{oc}.

The theoretical maximum value of V_{oc} is determined by the effective energy gap (E_g) defined as the difference between the HOMO of the donor ($HOMO_D$) and the LUMO of the acceptor ($LUMO_A$)[69-71]. However, the experimental value of V_{oc} is always lower due to loss mechanisms:

$$V_{oc} = \frac{1}{e}(E_g - E_{loss})$$

<div align="right">(2-6)</div>

where E_{loss} is an empirical factor of losses in solar cells. Scharber et al. analyzed the relationship between V_{oc} and E_g for over 26 different BHJ solar cells made of different donor or acceptor materials, and found that E_{loss} in BHJ solar cell using fullerene derivatives as acceptor is generally around 0.3 eV[72].

iii)   FF.

The maximum power point (P_m) of the solar cells corresponds to the voltage (V_m) and current (J_m) that maximizes electrical power output ($P_m = V_m \cdot J_m$). The solar cell fill factor FF is defined by:

$$FF = \frac{V_m \cdot J_m}{V_{oc} \cdot J_{sc}}$$

<div align="right">(2-7)</div>

Thus, according to equation 2-5 and 2-7 power conversion efficiency η can be expressed as:

$$\eta = \frac{V_{oc} \cdot J_{sc} \cdot FF}{P_{in}}$$

<div align="right">(2-8)</div>

High charge carrier mobilities and efficient charge extraction are necessary to minimize charge recombination, achieve a high FF, thus a high PCE.

2.5 Methods for improving the performance

To date, the highest efficiency for single junction organic solar cells is around 13 %[24,73-75] [7] . These promising results are the outcome of the synthesis of new organic materials and of the improved device architectures. In recent years, the better understanding of the solar cell operation mechanisms led to numerous

discussions about breaking the limits of the power conversion efficiency. It is important to be aware of the maximum attainable efficiencies in order to find the factors that limit the efficiency and formulate relevant strategies for reaching the limits.

To improve the performance of organic solar cells, several approaches have been suggested. Enhancement of light absorption by increasing further the absorption width of the conjugated molecules is still possible.

Increasing V_{oc} by controlling the LUMO and HOMO energy levels of donor and acceptor materials is also crucial for improving the PCE.

A better controlled nanomorphology of the BHJ active layer by choosing for instance proper solvents and post-processing methods can improve the efficiencies of the BHJ solar cells as well. Thermal annealing is a common strategy to improve the morphology of BHJ active layer. Another approach is solvent vapor annealing, by placing the solar cell samples in a solvent saturated environment.[76–78] Using processing additives, i.e. introducing small amounts of a solvent into the host solvent to solubilize the active materials, is another approach to control the BHJ morphology.

CHAPTER 3

State-of-the-art of soluble molecular donors

The last two decades have seen remarkable progress in the development of organic bulk heterojunction (BHJ) solar cells. During this period, the power conversion efficiency (PCE) of polymer-based organic solar cells (P-OSC) has reached 13 %[7], while small-molecule-based organic solar cells (SM-OSC) exceeds 10%[73,74]. This rapid progress was made possible through improved molecular design, reformative device architecture and better control of morphology.

In this chapter, I will give a short overview of the design strategies of small molecule donors that have been followed worldwide to improve the efficiency of SM-OSC devices.

3.1 Design strategy of small molecule donors

A most common strategy to design a small molecule donor is to associate electron-rich and electron-deficient moieties, referred to as donor (D) and acceptor (A) units, respectively, along the conjugated backbone in order to tune its frontier orbital energy levels and approach optimum values[79–81]. As shown in

Figure 3-1, when D and A units are associated together, the new hybrid HOMO level is close to (generally slightly higher than) the HOMO of the D unit while the new LOMO level is close to (or slightly deeper) than the A unit. As a result, the energy band gap can be adjusted.
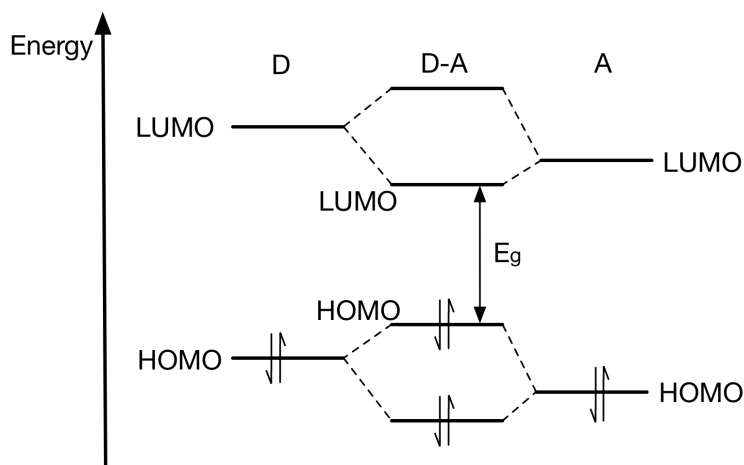
Figure 3-1: Illustration of the hybridization of energy levels of a conjugated molecule alternating donor (D) and acceptor (A) units.

Generally, these molecules are axisymmetric, that is, donor-acceptor (D-A) structures are symmetric about the central core, such as A-D-A, D-A-D, A-D1-D2-D1-A or D1-A-D2-A-D1 structures. An advantage of these structures is that the optoelectronic and molecular properties can be tuned by varying one of the moieties without changing the overall structure. The symmetry of the structures also assists the molecular self-assembly and often leads to well-developed ordered structures and correspondingly high photovoltaic performance.

The study on oligothiophene based molecule donors by Chen's group show that adding electron-withdrawing end-groups such as dicyanovinyl[82], alkylcyanoacetate or indenedione[83] to build A-D-A molecules improves the photovoltaic performance. The highest PCE results were obtained using dicyanovinyl-substituted rhodamine (RCN) as electron-withdrawing group (chemical structures shown in Figure 3-2). The results show that molecules with axisymmetric chemical structures (**DRCN5T**, **DRCN7T**, **DRCN9T** in Figure 3-2) exhibit much higher J_{sc} values (14-16 mA cm^{-2}) and thus higher PCEs than those with centrosymmetric chemical structures (**DRCN4T**, **DRCN6T**, **DRCN8T**) (J_{sc}~11 mA cm^{-2}). Maximum PCE of 10.08 % for **DRCN5T** and 9.4% for **DRCN7T**

have been obtained, which are among the highest PCE values for small molecule based BHJ solar cells obtained so far. Moreover, according to morphological investigations of the active layers by transmission electron microscopy (STM) and grazing incidence X-ray diffraction (GIXD), molecules with axisymmetric chemical structures exhibit more well-developed fibrillar networks, which is beneficial for charge carrier transport, and lead to high J_{sc} and FF[84].
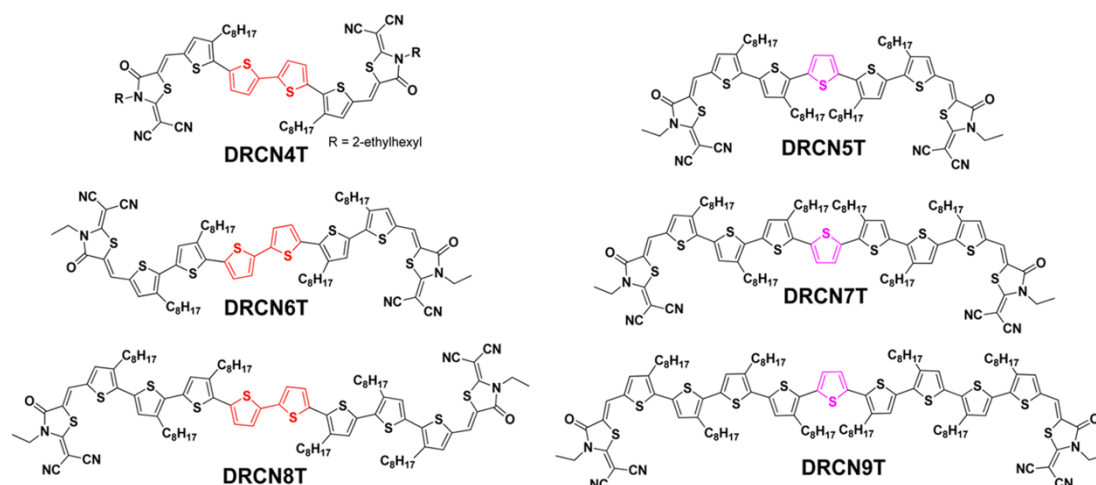
Figure 3-2: Chemical structures of **DRCN4T** - **DRCN8T**, adapted from Reference [84].

Table 3-1: Average OPV performance parameters for DRCN5T-DRCN9T BHJ devices under the optimized conditions. Adapted from Reference [84].

Molecules	Voc (V)	Jsc (mA cm-2)	FF	PCE (%)
DRCN5T	0.92	-15.66	0.68	9.8
DRCN6T	0.92	-11.45	0.58	6.1
DRCN7T	0.90	-14.77	0.68	9.1
DRCN8T	0.86	-10.80	0.68	6.4
DRCN9T	0.81	-13.77	0.68	7.6

Similar work has been done by Zhang *et al.* to synthesize A-D-A molecule using BDD units with strong electron-withdrawing ability. A quite deep HOMO level of -5.12 eV was obtained, as presented in Chapter 2, V_{oc} equals to the difference between HOMO level of the donor and the LUMO level of the acceptor, thus a deep HOMO level of the donor material leads to a high V_{oc}. Here, for BDD based molecules, a Voc as high as 0.96 V has been obtained and a maximum PCE of 9.53 was achieved[73].

Another important approach has been to address the molecular self-assembly in solid state by adding highly planar units. The planar units are expected to

increase intermolecular forces and allow a better charge extraction through improved charge carrier mobilities.

The investigation on the influence of highly planar units in molecule donors has been done first by Lee and co-workers[85]. They attached different electron-rich end-groups onto an electron-withdrawing core. Those end-groups have varying degrees of planarity (chemical structure shown in Figure 3-3). **Molecule 1** has non-planar triphenylamine (TPA) as end-groups, while end-groups of **molecules 2** is benzo[1,2-b;4,5-b']dithiophene (BDT), which contains a planar fused ring but has no-coplanar alkoxy substituents. **Molecule 3** and **4** has highly planar pyrene end-groups, but the sites of pyrene substituents are different.
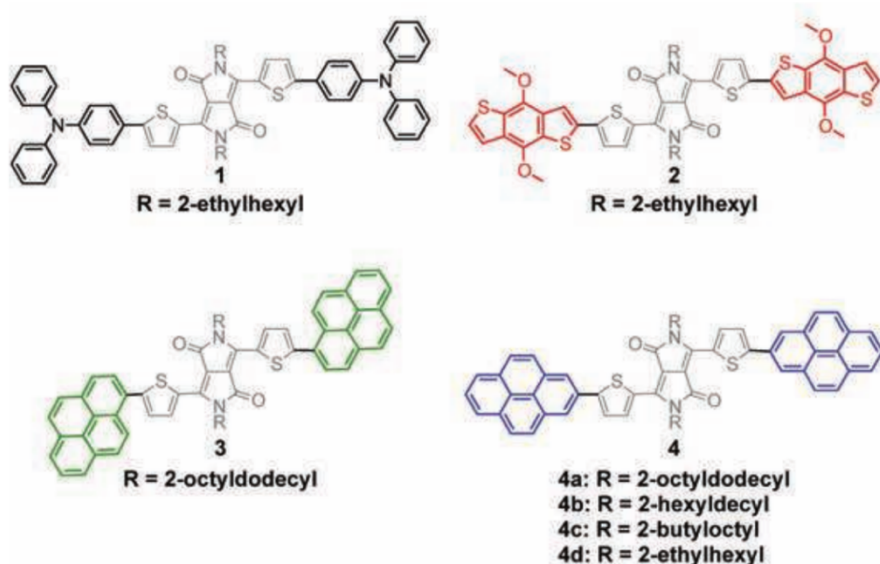
Figure 3-3: Chemical structures of molecules with DPP core moiety flanked by different electron-rich end-groups. Adapted from Reference [85].

The average OPV performances of BHJ devices are summarized in Table 3-2, and show that the molecule with highly planar end-groups (**molecule 4** in Figure 3-3) have higher PCEs than non-planar end-groups. Because planar end-groups facilitate favorable end-to-end π-π interactions (illustrated in Figure 3-4), hence, charge transport between adjacent molecules and photovoltaic efficiencies are enhanced[85].

The comparison of **molecule 3** and **4a** indicates that the end-group symmetry can also have significant influence on PCE. Further variation of alkyl side chains on the DPP core moiety showed that the side-chains can affect the intermolecular spacing and OPV performance (**molecule 4a, 4b** and **4c**).

= electron-deficient unit
= electron-rich unit   Molecular self-assembly via end groups
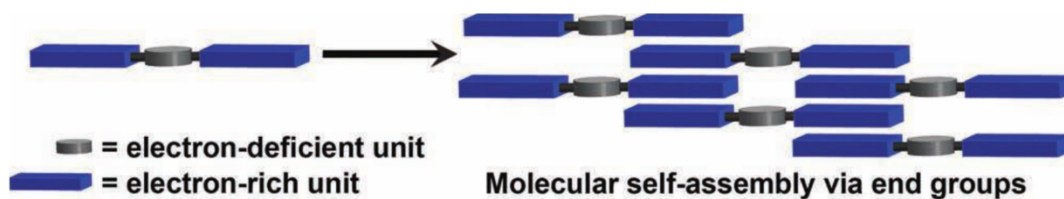
Figure 3-4: Illustration of molecular self-assembly through end-to-end π-π stacking. Adapted from Reference [85].

Table 3-2: Average OPV parameters for molecule 1-4. Adapted from Reference [85].

Molecule	Voc (V)	Jsc (mA cm-2)	FF	PCE (%)
1	0.73	-4.3	0.31	1.0
2	0.81	-6.2	0.30	1.3
3	0.73	-3.2	0.29	0.7
4a	0.77	-5.7	0.55	2.4
4b	0.76	-8.3	0.58	3.7
4c	0.78	-6.6	0.48	2.4

3.2 Triazatruxene units for molecule donors

The same design strategies are employed to molecule donors investigated in this thesis. In our ORION project, 10,15-dihydro-5*H*-diindolo-[3,2-*a:3',2'-c*]carbazole units, also called triazatruxene (TAT), are used as π-stacking platform (shown in Figure 3-5).
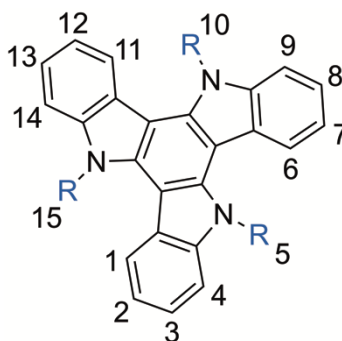
Figure 3-5: Chemical structure of the triazatruxene (TAT), showing its complete numbering.

Functionalized triazatruxene derivatives are interesting organic electronic materials because of their unique optoelectronic properties. The first TAT unit was synthesized by Sweden chemists Jan Bergman and Nils Eklund in 1980[86,87]. It is a C_3 symmetric planar π-extended conjugated structure, and can be considered as an overlapping framework of three carbazole units fused together, thus, resulting in an electron-donating unit. The planar character of TAT moieties promotes π-orbital overlapping, leading to a strengthened molecular

stacking behavior and charge transport. In addition to its planarity, the TAT units can also be made highly soluble because of three amine groups (position 5, 10 and 15) that are able to carry alkyl chains. For instance, **TAT$_{C8}$** shown in Figure 3-6 is an alkylated triazatruxene unit which has been investigated by Gallego-Gómez et al.[88]. It can be self-assembled into ordered nanostructures in solution-processed cast films. in addition, face-to-face molecular packing in a columnar crystalline phase provided a significant π-π stacking and therefore good charge transport[88].

TAT$_{C8}$

R=C$_8$H$_{17}$
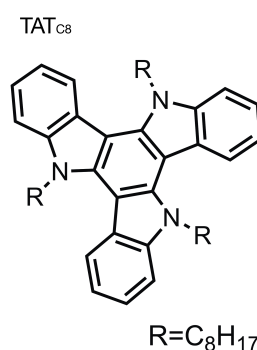
Figure 3-6: Chemical structure of **TAT$_{C8}$**.

TAT units can also be functionalized to build more complex molecular architectures (through position 2, 3, 7, 8, 12, or 13), such as star-shaped molecules[89–91], dumbbell-shaped molecules[11,12,92,93], D-π-A linear molecules[92], etc.

Bura *et al.* reported a series of TAT functionalized D-π-A linear molecules which show large absorption coefficients and fluorescence quantum yields as well as interesting electrochemical properties due to the introduction of TAT units[92]. Molecules TAT-Bodipy2 in this series reaches a V$_{oc}$ of 0.83 V, J$_{sc}$ of 3.6 mA/cm^2 and the a promising PCE of 0.9 %.

TAT-Bodipy1   TAT-Bodipy2   TAT-Bodipy3
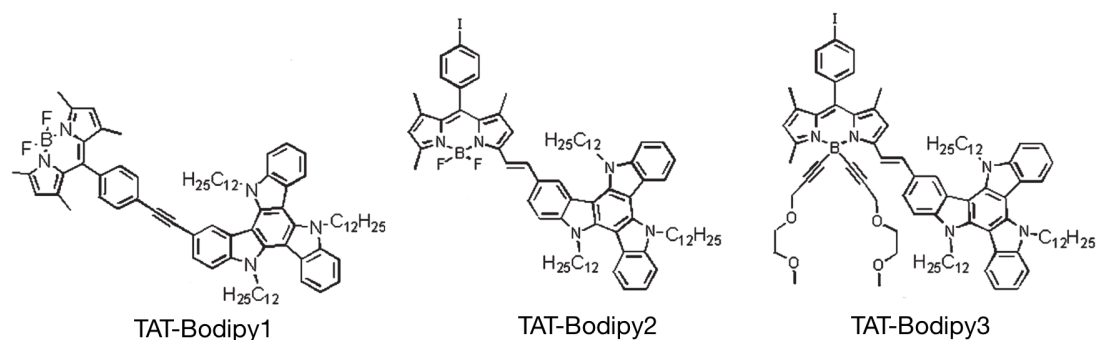
Figure 3-7: Chemical structures of TAT-linked Bodipy derivatives. Adapted from reference [92].

Huaulmé *et al.* further synthesized a family of star-shaped molecules with TAT as the core and DPP as the branches to broaden the photo-absorption region and reduce the band gap (Figure 3-7).[91] All the molecules exhibits strong and wide absorption in the near-UV and visible region of the solar spectra (400 -750 nm), with intramolecular cascade energy transfer enabling photo concentration and fluorescence at approximately 740 nm.

TAT(DPP)   **TAT(DPP)$_2$**   **TAT(DPP)$_3$**
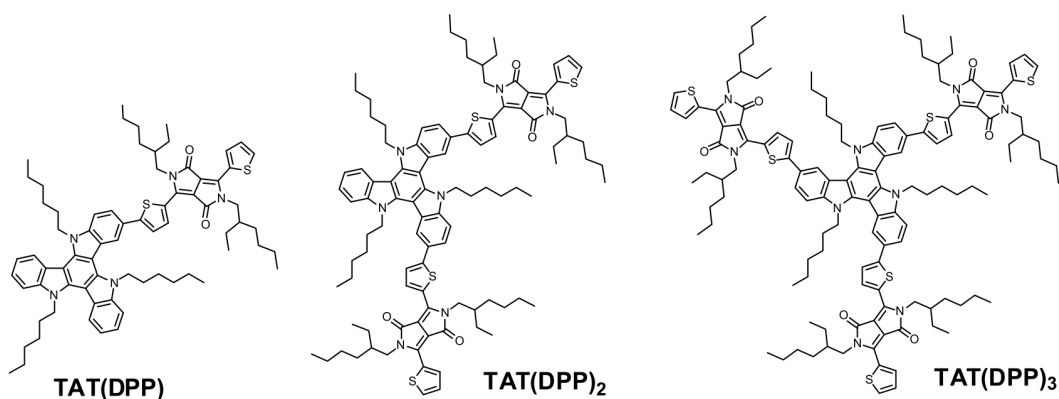
Figure 3-8: Chemical structures of the mono-, bis-, and tris- DPP substituted TAT based star-shaped panchromatic absorbing dyes. Adapted from reference [91].

Our group has previously used TAT units as end-groups attached onto electron acceptor units such as DPP to build dumbbell-shaped molecules[11]. Both, good planarity and solubility were achieved. The TAT units promoted end-to-end π-π stacking and lead to favorable transport properties. Promising V_{oc} above 0.6 V, J_{sc} around 14.6 mA cm^{-2} and a PCE of 5.3 % were obtained.
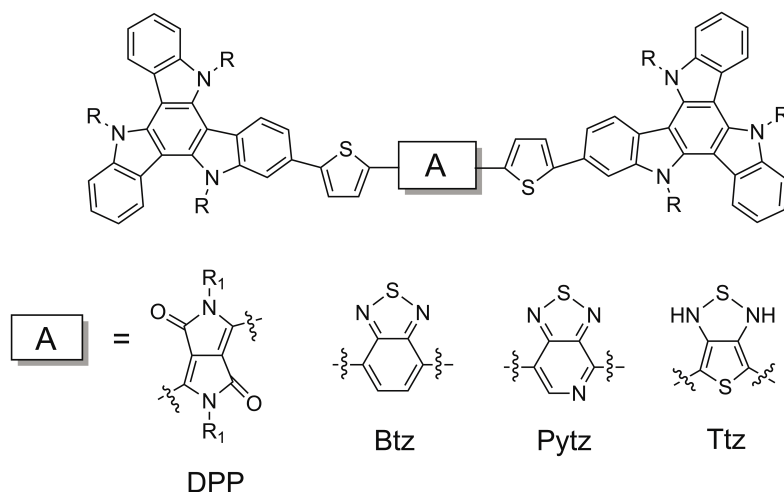
Figure 3-9: Chemical structures of TAT based dumbbell-shaped molecules with different central cores.

Moreover, by varying the electron-attracting central moiety, the electrochemical properties could be tuned without changing significantly the chemical

structure. Indeed, a series of dumbbell-shaped molecules, with benzo[2,1,3]-thiadiazole (Btz), pyridal[2,1,3]-thiadiazole (Pytz), or thieno[1,2,5]-thiadiazole (Ttz) as electron-withdrawing cores, respectively, and triazatruxene end-cappers were investigated.[11,12,92,93] The HOMO levels were similar for all the compounds, while the LUMO levels decreased from -3.6 eV (Btz) to -3.8 eV (Pytz), and to -3.9 eV (Ttz), respectively. The relationship between chemical structure and electronic properties remains hard to predict, because a slight change in the molecular assembly can have a strong influence on charge transport and morphology (in particular in a donor/acceptor blend). For instance, the position and nature of alkyl side chains are nowadays well known to strongly impact the structural properties of π-conjugated materials, whether polymers or small molecules[94,95], which possibly affects the material optoelectronic properties.

3.3 Thesis in context

To further understand how the presence of alkyl chains on the TAT unit may influence the optoelectronic properties, we have studied in depth a series of TAT-based dumbbell-shaped molecule donors and their behavior in BHJ solar cells. The molecules were based on an identical π-conjugated backbone, made up of a thieno[3,4-c]pyrrole-4,6-dione) (or TPD) central chromophore and two TAT units. A series of molecules with different combinations of side chains were investigated (molecules will be presented in detail in chapter 4). The TPD unit is an electron-withdrawing group that can decrease the FMO energy levels of molecule donors. In addition, the relatively compact and planar structure of TPD could facilitate the electron delocalization and enhance the intermolecular interactions.

In this thesis, the charge transport, microstructure and optoelectronic properties of these molecules have been studied in-depth and the effect of TAT units on molecular organization, charge transport and photovoltaic performances have been explored both, in pure materials and in blends with PCBM.

CHAPTER 4
Materials & Experimental Methods

A series of organic semiconducting molecular electron donors were investigated in this thesis. In order to understand the material properties as much as possible, different types of experimental techniques were employed. In this chapter, the experimental details of the procedures used throughout this thesis are summarized.

First, a brief description of the materials and substrates will be given. Then the experimental methods for investigating molecular and bulk material properties are presented, followed by the characterization of thin-film morphologies. The next section introduces the in-plane and out-of-plane charge carrier transport measurements. Elaboration procedures and analytical expressions used to extract the carrier mobilities are also detailed. The final section of this chapter presents the elaboration procedures of inverted organic solar cell devices and also the characterization methods.

4.1 Materials and substrates

In this thesis, the organic materials used as electron donor were designed and synthesized by Dr. I. Bulut from the ICPEES[a] under the supervision of Prof. Nicolas Leclerc. Their molecular structure is shown in Figure 4-1.

TPD_{C8}-TAT_{C8} : R = C_8 ; R_1 = C_8
TPD_{EH}-TAT_{C8} : R = EH ; R_1 = C_8
TPD_{C8}-TAT_{EH} : R = C_8 ; R_1 = EH
TPD_{EH}-TAT_{EH} : R = EH ; R_1 = EH

EH =

C_8 =
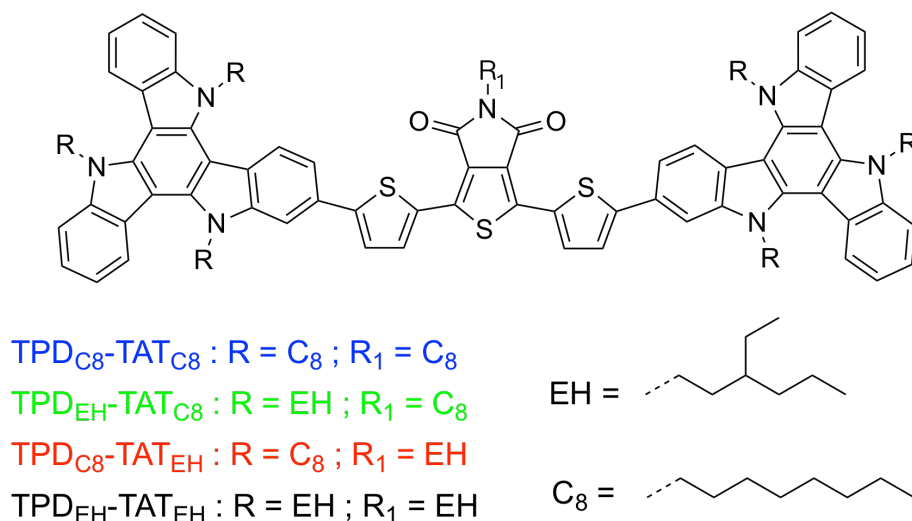
Figure 4-1: Chemical structure of dumbbell-shaped molecules TPD-TAT.

Those molecules use a thienopyrroledione (TPD) unit as central core, end-capped by two triazatruxene (TAT) units. The TAT unit has three amine group that are able to carry alkyl chains. Also, TPD can be alkylated independently from the TAT units. Thus, different side-chain combinations were explored, with either 2-ethylhexyl (EH) ramified side chains, n-octyl (C_8) linear side chains or a combination of both 2-ethylhexyl and n-octyl side chains.

The electron acceptor material [6,6]-phenyl-C71-butyric acid methyl ester (PC71BM) with a purity >99% was purchased from Solenne B.V. and used as received.

Poly(3,4-ethylenedioxythiophene)-poly(styrenesulfonate) (or PEDOT:PSS) was purchased from Heraeus Clevios™ and used as received. 80% ethoxylated polyethyleneimine solution (PEIE, 35-40 wt.% in H_2O, average M_W ~70,000

---

[a] Institut de Chimie et Procédés pour l'Energie, l'Environnement, Strasbourg, France

g/mol) and 2-Methoxyethanol (99.8%) were purchased from SIGMA-ALDRICH and utilized as received.

The solvent chloroform was purchased from SIGMA-ALDRICH and used as received. The purity of Chloroform is ≥99% and contains 0.5-1.0% ethanol as stabilizer. The processing additive 1,8-diiodooctane (DIO) was purchased from SIGMA-ALDRICH and used as received. DIO has a purity of 98% and contains copper as stabilizer.

Indium tin oxide (ITO) coated glass substrates used for solar cell devices and space-charge-limited-current (SCLC) diodes were purchased from Luminescence Technology Corp. The dimension of substrates is 20 × 20 × 1 mm (large × weight × height). The thickness of ITO layer is around 1200~ 1600 Å and the sheet resistance is between 9~ 15 Ω/sq.

4.2 Experimental methods

4.2.1 Molecular & bulk material properties

4.2.1.1 Ultraviolet-visible spectroscopy

A schematic of a UV-vis spectrophotometer is shown in Figure 4-2. Generally, a UV-vis spectrophotometer contains a radiation source, a monochromator for light dispersion, a sample compartment, and a photodetector. The radiation source emits light with a range of wavelengths. The light then passes through the monochromator that disperses the light by a diffraction grating. So light of a given wavelength can be extracted and crosses the sample. Afterwards, the detector records the degree of absorption (Absorbance) at each wavelength. The photomultiplier tube is a commonly used detector in UV-Vis spectroscopy. It contains a photoemissive cathode, anode and several dynodes. Photons entering the tube strike the cathode, causing the emission of electrons. The electrons are accelerated towards the first dynode. The electrons strike the first dynode, resulting in the emission of several electrons for each incident electron. Those electrons are then accelerated towards the second dynode, to produce more electrons which will accelerated toward the third dynode and so on. Eventually,

the electrons are collected at the anode and resulting current will be amplified and measured.
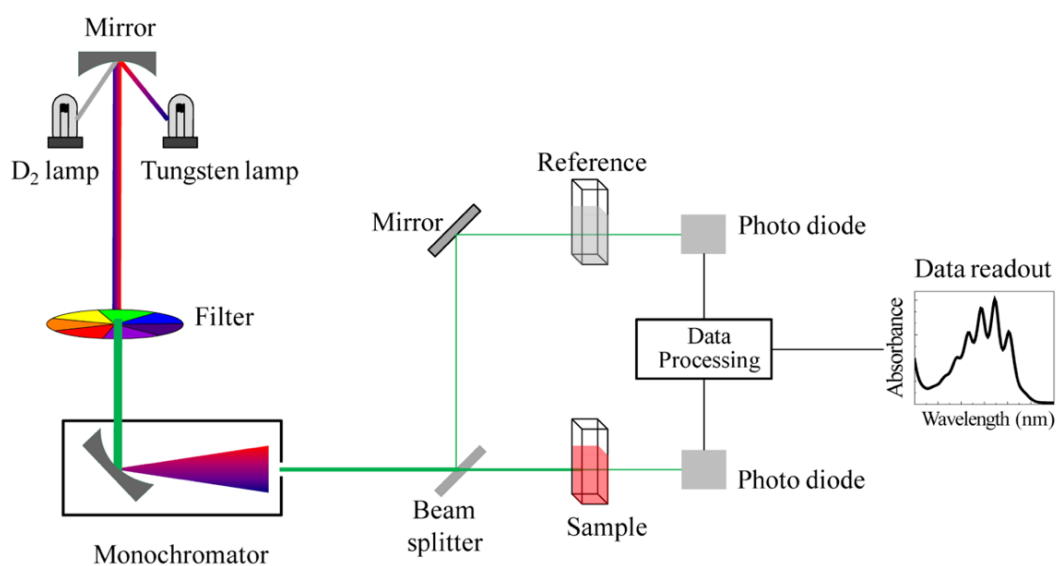
Figure 4-2: Schematic of a UV-vis spectrophotometer, image adapted from Wikipedia Commons.

For liquid samples, the absorbance (A) is defined as the $\log_{10}$ of the ratio between transmitted light intensity at a given wavelength (I), and the incident light intensity (I_o) at the same wavelength:

$$A = \log_{10} \frac{I_0}{I}$$ (4-1)

According to Lambert-Beer's law, the absorbance (A) is proportional to the concentration (C) of the solution and the path length (L):

$$A = \alpha \cdot C \cdot L$$ (4-2)

where α is the absorption coefficient, which depends on the solvent, temperature and pressure.

The wavelength at the absorption edge, λ_{onset} (shown in Fig 4-3) is used to calculate the optical gap energy $E_{g,opt}$, according to the equation:

$$E_{g,opt} = \frac{1242}{\lambda_{onset}} \text{ eV}$$ (4-3)

In this thesis, all the UV-visible absorption spectra were recorded at room temperature using a Shimadzu UV-3600 dual-beam grating spectrophotometer at ICPEES.
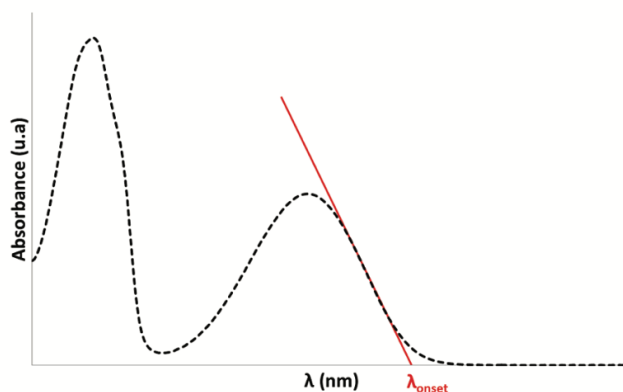
Figure 4-3: Experimental determination of optical band gap.

4.2.1.2 Cyclic voltammetry

The electrochemical properties were studied by cyclic voltammetry with a potentiostat (VPS type from BioLogic Science Instruments). All the measurements were conducted under argon (Ar), in a conventional three electrodes system consisting of a Pt micro disk (2 mm^2) working electrode with a scanning speed between 20 to 50 mV·s^{-1}, a Pt wire counter electrode, and a reference electrode (Ag/Ag+).

The semiconducting small molecules were studied both in solution (10^{-4} M in CH$_2$Cl$_2$) and thin films. Recrystallized tetrabutylammonium hexafluorophosphate (Bu4NPF6) or tetrabutylammonium perchlorate were used as a supporting electrolyte (0.1 M) in distilled and anhydrous CH2Cl2.

Potentials were calibrated versus the saturated calomel electrode (SCE), using the ferrocene/ferricinium couple as internal reference.

The voltage applied to the working electrode is scanned linearly. During the potential sweep, the potentiostat measures current as a function of the applied potential. The values of the oxidation and reduction potentials (E_{ox} and E_{red}) are measured at the threshold of the corresponding peaks. The corresponding HOMO and LUMO levels, or the ionization potential (*IP*) and the electron affinity (*EA*), are then determined according to the following equations:

$$IP = |E_{HOMO}| = E_{OX}^{onset} + 4.4\ eV \qquad (\,4\text{-}4\,)$$

$$EA = |E_{LUMO}| = E_{RED}^{onset} + 4.4\ eV \qquad (\,4\text{-}5\,)$$

The electrochemical band gap is given by *IP – EA*.

4.2.1.3 Differential scanning calorimetry

To study the thermal transitions of the organic semiconductors, a technique called differential scanning calorimetry (DSC) is employed. DSC measures the amount of energy absorbed or released by the organic material when it is heated or cooled. It provides quantitative and qualitative information on endothermic (heat absorption) and exothermic (heat evolution) processes, such as, melting temperature, glass transition temperature, crystalline phase transition temperature and energy, etc.

DSC measurements in this thesis were performed with a TA Instruments Q1000 instrument by Dr. Benoît Heinhrich, operated at a scanning rate of 5 °C min^{-1} on heating and on cooling.

4.2.1.4 Small-angle X-ray scattering

Small angle X-ray scattering (SAXS) analysis was used to determine the structural properties of macromolecular and nanostructured systems. It offers information about the shape and size of macromolecules, characteristic distance of partially ordered materials, pore size and other data[96]. The typical experimental setting is shown in Figure 4-4. A monochromatic beam of incident X-rays travels through the investigated bulk material, while the lattice structure causes the incident X-rays to diffract in different directions. The scattered X-ray intensities are collected at very low scattering angle (close to 0°). A spatial variation of electron density at a nanometer scales will scatter an X-ray beam to low angles, while that on the atomic scale will scatter to high angles[97]. Therefore, to study molecular structure at large distances, small-angle X-ray diffraction technique is used. On the other hand, to study the molecular structure at small distance, wide-angle X-ray diffraction will be used (presented in 4.2.2)

Powder XRD patterns in this thesis were obtained with a linear monochromatic Cu Kα1 beam (λ=1.5405 Å) using a sealed-tube generator equipped with a bent quartz monochromator and a curved Inel CPS 120 counter gas-filled detector; periodicities up to 70 Å can be measured, and the sample temperature controlled to within ±0.01 °C from 20 to 200 °C. The sample was filled in Lindemann capillaries and exposure times were of 6 h.
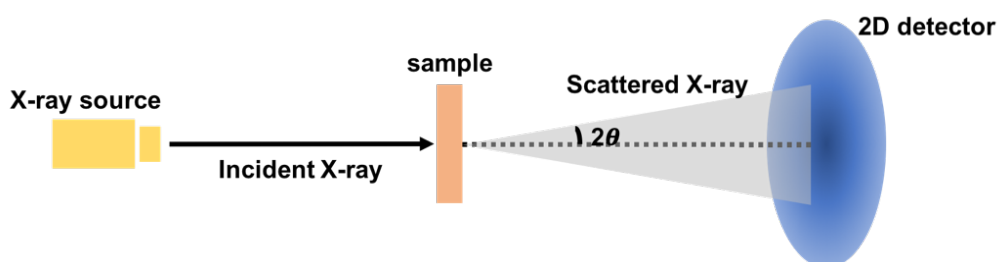
Figure 4-4: Schematic representation of 2-dimensional small-angle-x-ray-scattering.

4.2.2 Thin film morphology

4.2.2.1 Atomic force microscopy

Atomic force microscopy (AFM) technique is used to map the topography of the thin-film surface. Figure 4-5 represents the typical tip-surface interaction force as a function of tip-sample distance. The cantilever mainly senses interatomic forces: repulsive forces at very short distance and van der Waals forces at longer distances. The strong repulsive force at short distance is mostly probed when AFM is operated in the contact mode[98].
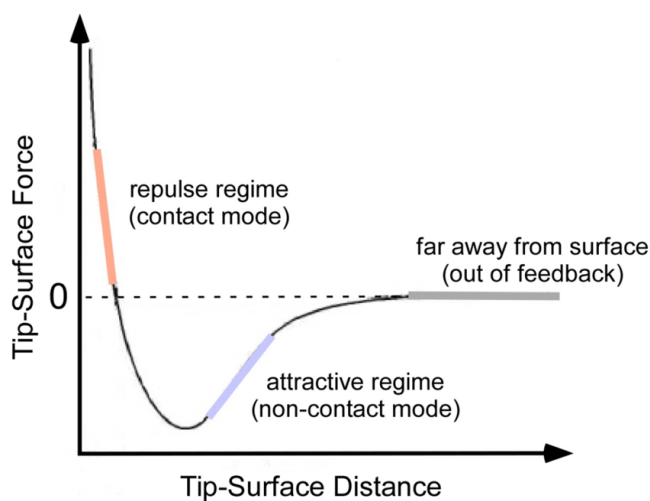
Figure 4-5: Tip-surface force-distance curve that reflects the the type of interaction between the tip and the sample surface for AFM measurements using specific operation mode. Adapted from Ref [98].

We used tapping-mode AFM for measuring the morphologies of thin-films. Figure 4-6 illustrates the working principle of this operational mode. A cantilever assembly is composed of a sharp tip placed on the edge of a cantilever. In the so-called tapping-mode AFM, the cantilever assembly is oscillated at or near the cantilever's resonant frequency using a piezoelectric actuator. The oscillating tip is then moved toward the analyzed surface, until it begins to interact with the surface. When the tip approaches the surface, the cantilever oscillation amplitude decreases. The oscillation amplitude of the tip is measured by a laser spot reflected on to a four-quadrant photodetector. During tapping mode operation, the cantilever oscillation amplitude is maintained constant by a feedback loop, while the vibrating tip is scanned over the sample surface. The voltage-controlled vertical position of the tip is adjusted to keep the oscillation amplitude constant. The voltage amplitude therefore follows the surface profile and is recorded as the surface topography by the AFM.

In tapping mode AFM, the phase shift between the cantilever's oscillation and the tip driving signal can be recorded as well. Surface areas that have different adhesion properties give rise to different phase lags and can be distinguished.

In this thesis, all the tapping-mode AFM measurements were performed on a Nanoscope IIIa system commercialized by Veeco®.
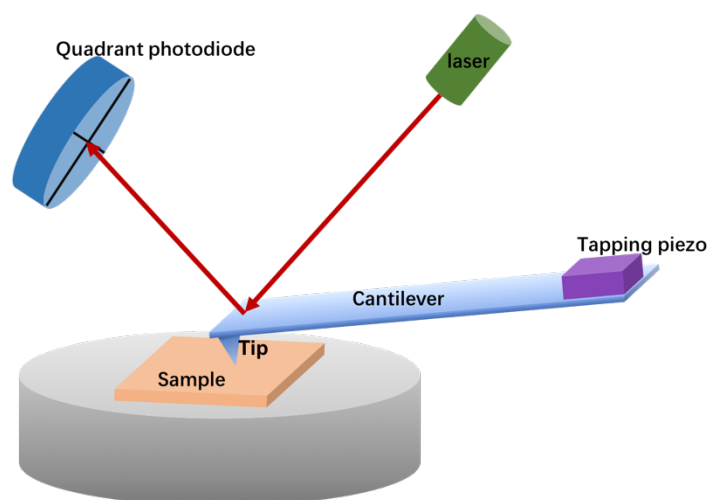
Figure 4-6: Schematic of the cantilever-tip assembly used in AFM.

4.2.2.2 Grazing-Incidence wide-angle X-ray scattering

Grazing-Incidence wide-angle X-ray scattering (GIWAXS) is also an X-ray diffraction technique used to analyze the molecular structure properties like SAXS, but the scattering angle of GIWAXS is larger, from 1° up to 45°, while the scattering angle of SAXS is close to 0°. The interest of GIWAXS is that the incident beam has a grazing incidence angle with respect to the film. This allows the beam to probe a large amount of material. It is thus particularly well suited for thin film structure analyses, while SAXS is done on powder. Doing GIWAXS at a synchrotron has the additional advantage of high intensity beam and therefore a high signal to noise ratio.

In this thesis, the GIWAXS measurements of organic molecular donors and blends of donors with fullerenes in thin-films were conducted by Dr. Benoît Heinrich, at synchrotron PLS-II 9A U-SAXS beamline of Pohang Accelerator Laboratory (PAL) in Korea, on films deposited by spin-coating on a silicon wafer. The X-ray beams coming from the vacuum undulator (IVU) were monochromated using Si(111) double crystals and focused on the detector using K-B type mirrors. Patterns were recorded with a 2D CCD detector (Rayonix SX165). The sample-to-detector distance was about 225 mm for an energy of 11.08 keV (wavelength = 1.119 Å).

4.2.3 Charge transport measurement

Since the charge carrier mobility is one of the key factors that limit the high-power conversion efficiency, charge transport measurements are necessary to understand the intrinsic material properties of designed molecule donors. Mobilities along different orientations have been measured. Transport along a vertical direction to the substrate is characterized by the out-of-plane mobility while the in-plane mobility describes transport parallel to the thin film. In-plane and out-of-plane hole mobilities were measured using organic field-effect transistors and space-charge-limited-current diodes, respectively. The combination of both methods gives us some insight into charge transport anisotropy.

4.2.3.1 Organic field-effect transistors

P-type organic field-effect transistors (OFETs) were fabricated to measure in-plane hole mobilities. For a p-type field-effect transistor, negative voltages are applied to the gate causing hole accumulation at the dielectric/semiconductor interface; in contrast, for n-type OFETs, positive gate voltages (V_{gs}) cause electron accumulation at the dielectric/semiconductor interface (with proper electrodes) (Figure 4-7). Upon the application of a voltage between source and drain (V_{ds}), the accumulated charge carriers drift along the channel and generate a source-drain current I_{ds}. Figure 4-8 shows a p-type OFET. When $|V_{gs}|$ < $|V_{th}|$ (V_{th} is the threshold voltage), the drain current is zero. As $|V_{gs}|$ becomes larger than $|V_{th}|$, the channel charge density increases, and so does the channel conductance. As a result, for a given V_{ds}, Ids increases as V_{gs} increases[99].

Figure 4-9a shows an I_{ds}-V_{ds} characteristics (also called output characteristics) of an OFET. In an OFET, the field induced by the gate voltage is generally much larger than the source-drain field. As a result, the gradual channel approximation can be used. If we assume that the charge carrier mobility in the channel μ is constant, the drain current can be described as[100]:

$$I_{ds} = \frac{W\mu C}{L}[(V_{gs} - V_{th})V_{ds} - \frac{V_{ds}^2}{2}] \qquad (\,4\text{-}6\,)$$

where C is the capacitance of the dielectric; W and L are channel width and length. Note that charge transport in OFETs is limited to the dielectric/organic semiconductor interface.

For small V_{ds} values ($V_{ds} \ll |V_{gs}\text{-}V_{th}|$), the channel region has the characteristics of a resistor, so the I_{ds}-V_{ds} characteristics is linear. In this linear regime, the equation 4-6 becomes:

$$I_{ds} = \frac{W\mu C}{L}(V_{gs} - V_{th})V_{ds} \qquad (\,4\text{-}7\,)$$

When V_{ds} values increases, the voltage drop across the dielectric near the drain terminal decreases, which means that the accumulated charge density near the drain also decreases. When V_{ds} increases to the limit that $V_{ds} \simeq |V_{gs}\text{-}V_{th}|$, the

accumulated charge density is zero at the drain terminal, the drain current becomes independent of the drain voltage. This regime is called saturation regime. Equation 4-6 becomes:

$$I_{ds} = \frac{W\mu C}{2L}\left(V_{gs} - V_{th}\right)^2 \qquad (\,4\text{-}8\,)$$

Exemplary transfer characteristics in both linear and saturation regimes are shown in Figure 4-9 (b) and (c), respectively. The mobilities at different regimes can be extracted directly from the transfer curve, in the linear regime:

$$\mu_{lin} = \frac{L}{WCV_{ds}}\left(\frac{\partial I_{ds}}{\partial V_{gs}}\right) \qquad (\,4\text{-}9\,)$$

In the saturation regime:

$$\mu_{sat} = \frac{2L}{WC}\left(\frac{\partial \sqrt{I_{ds}}}{\partial V_{gs}}\right)^2 \qquad (\,4\text{-}10\,)$$

Although those equations were originally developed for inorganic field-effect transistors originally, but they show a relatively good correspondence for organic semiconductors too. However, in organic semiconductors, the mobility usually increases with charge carrier density, i.e. with increasing gate voltage. As a consequence, mobilities extracted from the saturation regime are higher than in the linear regime[101].
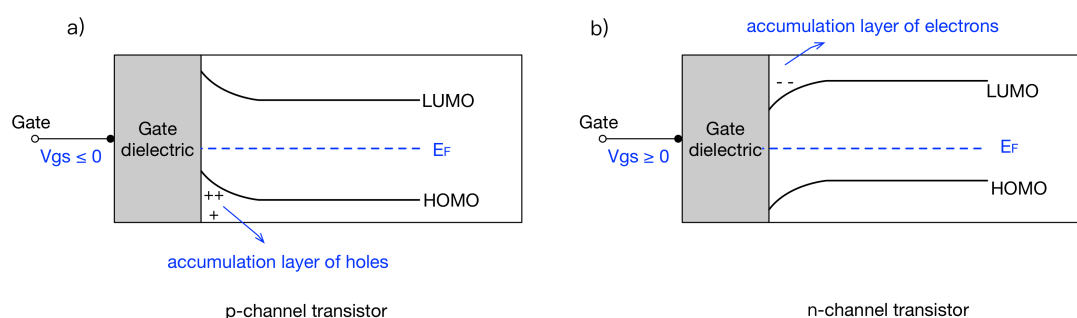
Figure 4-7: The energy-band diagram of an OFET with (a) a negative gate bias; (b) a positive gate bias.
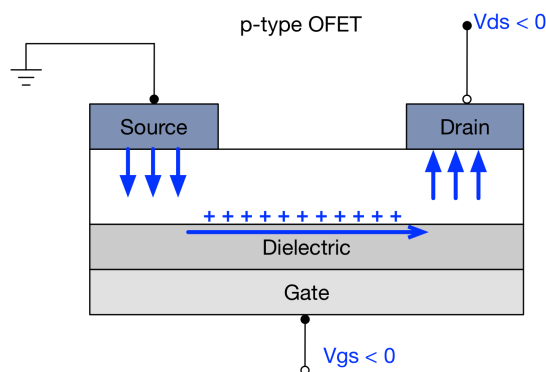
Figure 4-8: Schematic of a p-type OFET where holes are accumulated and transported.
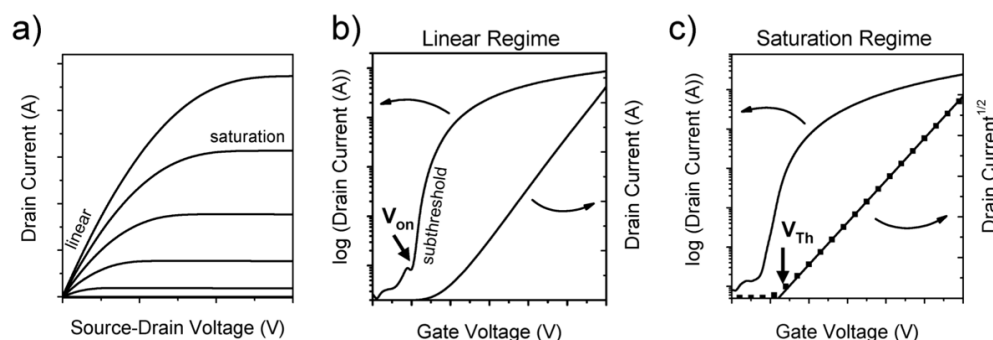
Figure 4-9 Ideal current-voltage characteristics of an OFET. (a) output characteristics indicating the linear and saturation regimes; (b) transfer curve in linear regime, indicating the onset coltage (V_{oc}) when the drain current increases abruptly. (c) transfer curve in saturation regime, indicating threshold voltage Vth, where the linear fit to the square root of the dran currrent intersects with the x-axis. Adapted from reference [100].

Elaboration procedures

The top-contact/bottom gate OFET structure is employed to measure the in-plane mobilities (shown in Figure 4-10).
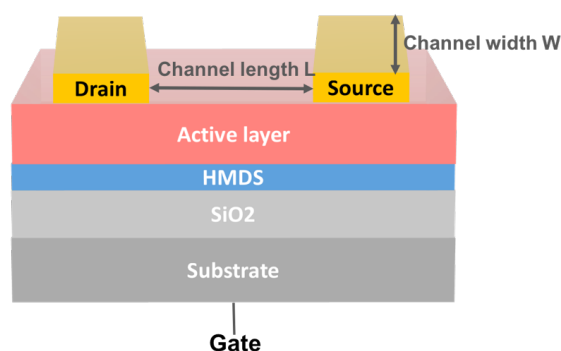
Figure 4-10: Configuration of a top-contact bottom-gate organic field-effect transistor.

OFETs were fabricated on silicon substrates with the 200 nm thermal silicon oxide (SiO_2) used as gate dielectric. The resistivity of the wafer is around 0.01 – 0.02 Ω.cm and the thickness is 675±25 m. The substrates were cut by YAG laser into the dimension of 15 × 20 mm.

Hexamethyldisilazane (HMDS) was used as a surface passivation layer. HMDS treatment leads to an improvement in hole mobility as well as to a decrease in current hysteresis[102]. 120 nm thick silver on top of a 7 nm thick Molybdenum trioxide (MoO$_3$) layer are used as source and drain contacts for p-type OFET to measuring the hole mobilities of our molecule donors.

The standard elaboration procedures for OFET are constituted of four steps:

1) Clean substrates: to remove the dusts and contaminants on the surface, the substrates were cleaned in ultrasonic bath at 45°C for 15 minutes each with deionized water with detergent, acetone and isopropyl alcohol, respectively.

2) UV-Ozone treatment: to eliminate the organic residues on the surface, the substrates were treated under an ultra-violet ozone system for 15 minutes.

After this step, the samples were transferred into the nitrogen-filled glove-box.

3) Deposit active layer: hexamethyldisilazane (HMDS) was spin-coated (500 rpm for 5 s and then 4000 rpm for 50 s) under nitrogen ambient and followed by an annealing step at 135°C for 10 minutes. Finally, 5 mg/ml concentrated anhydrous chloroform solutions of molecule donors or blends with PC$_{71}$BM were spin-coated (3000rpm for 60s).

4) Evaporate top electrodes: 7nm MoO3 and 120 nm Ag were thermal evaporated on the top of the active layer under vacuum ($< 10^{-6}$ mbar).

Our OFET layout is shown in Figure 4-11, it includes six transistors with different channel lengths L (60, 80 and 100 μm). The channel length and channel width are summarized in the Table 4-1. For all the transistors, the ratio W/L is constant.
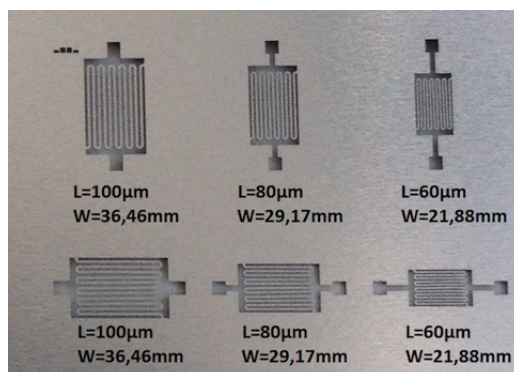
Figure 4-11: Scheme of a substrate including six OFETs of variable dimensions.

Table 4-1: Dimensions of top-contact/bottom gate OFETs.

Channel length L (μm)	Channel width W (mm)	W/L ratio
60	21.6	360
80	28.8	360
100	36	360

Electrical characterization

Device characterizations were performed in nitrogen ambient. The transistor output and transfer characteristics were measured with probe station, and recorded using a Keithley 4200 semiconductor characterization system. The charge carrier mobility was extracted in the saturation regime using the equation 4-10 described above on FET devices.

Temperature dependent electrical characterization

The OFETs were further measured at various temperatures. The temperatures were adjusted by a Peltier thermo-module. First, the OFET sample was fixed on a metal substrate with silver paste in order to polarize the gate electrode. Then the sample was placed on the Peltier module, measured by four-points station every 10°C, from -10°C to 50°C.

4.2.3.2 Space-charge-limited-current diodes

Space-charge-limited-current (SCLC) devices were elaborated to investigate the out-of-plane mobilities. For electrically conducting materials, the dielectric relaxation time (τ_{relax}) is defined as the time necessary for the charges to restore the local electric neutrality after charge injection. It is given by:

$$\tau_{relax} = \frac{\varepsilon_0 \cdot \varepsilon_r}{\sigma} \qquad (\text{4-11})$$

where ε_0 is the dielectric constant in vacuum, ε_r is the relative dielectric constant and σ is the electrical conductivity.

On the other hand, the time of flight τ_{flight} describes the time it takes for the injected charges to cross the semiconductor under an applied voltage (V). It is given by:

$$\tau_{flight} = \frac{L^2}{\mu \cdot V} \qquad (\ 4\text{-}12\ )$$

where L is the thickness of the active layer, μ is the out-of-plane mobility and V the applied voltage. If $\boldsymbol{\tau}_{\text{flight}}$ is far higher than $\boldsymbol{\tau}_{\text{relax}}$ ($\boldsymbol{\tau}_{\text{flight}} \gg \boldsymbol{\tau}_{\text{relax}}$), the current follows the Ohm's law:

$$J = \mu \cdot q \cdot p_0 \cdot \frac{V}{L} \qquad (\ 4\text{-}13\ )$$

where p_o is the background charge carrier density.

However, the conductivity of organic semiconductors is low, and $\boldsymbol{\tau}_{\text{relax}}$ is often much higher than $\boldsymbol{\tau}_{\text{flight}}$ ($\boldsymbol{\tau}_{\text{relax}} \gg \boldsymbol{\tau}_{\text{flight}}$). In this case, Ohm's law is no longer valid, while Mott-Gurney's law applies[103]:

$$J = \frac{9\varepsilon_0\varepsilon_r}{8} \cdot \mu \cdot \frac{V^2}{L^3} \qquad (\ 4\text{-}14\ )$$

This current is called space-charge-limited-current (SCLC). SCLC current depends on the charge carrier mobility. Therefore, the mobility can be estimated from a simple current-voltage measurement in this regime. One should note however that this equation is true only if the following assumptions are satisfied: 1) negligible injection barriers, diffusion currents and traps in semiconductors; 2) the mobility is constant throughout the sample;

3) SCLC mobility is independent of the electric field and charge carrier density.

Figure 4-12 presents an example of a J-V characteristic of a SCLC device plotted in log-log scale. Two regimes can be distinguished. At low voltage, the curve follows Ohm's law, whereas at high voltage, the current density J is proportional to V^2 according to Mott-Gurney's law with a constant charge carrier mobility. Devices with different active layer thicknesses are fabricated to make sure the SCLC regime obtained, and since the film thickness is a power of three in equation 4-14, it is importance to accurately measure the thickness values.
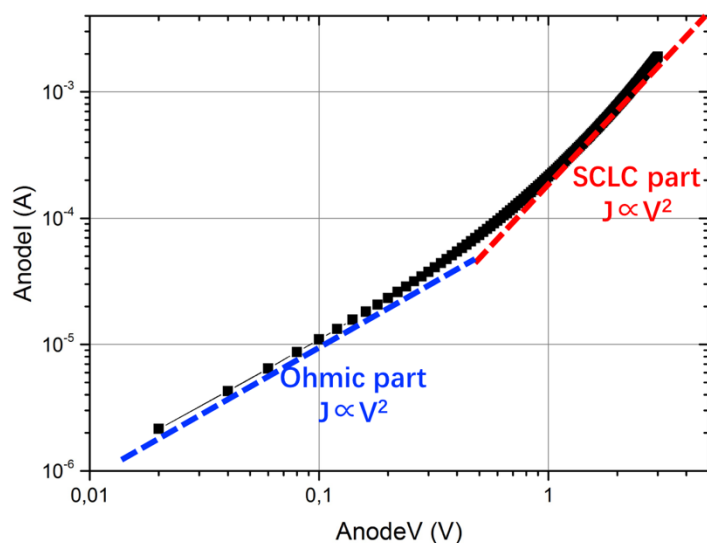
Figure 4-12: J-V characteristic of a SCLC device in log scale.

Elaboration procedures

The device structure used for hole mobility measurements is shown in Figure 4-13: Indium Tin Oxide (ITO) coated glass was used as substrate. PEDOT:PSS was used as the hole injection electrode. A 120 nm thick silver layer was deposited on top of a 7 nm thick MoO_3 layer as the top electrode. Each substrate can accommodate 21 diodes with three different surface areas.
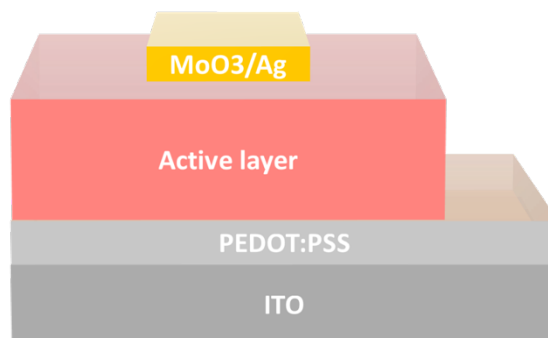
Figure 4-13: Schematic of a SCLC device.

The SCLC device elaboration procedures are as follows:

1) Clean substrates: to remove the dusts and contaminants on the surface, the glass-ITO substrates were cleaned in acetone, isopropyl alcohol and deionized water at 45°C for 15 minutes, respectively;

2) UV-Ozone treatment: the substrates were treated under an ultra-violet ozone system for 30 minutes to eliminate the organic residues on the surface;

3) Deposit PEDOT:PSS: PEDOT:PSS was spin-coated on the top of ITO layer (5000 rpm for 60 s) and then dried at 140°C for 30 minutes.

After this step, the samples were transferred into the nitrogen-filled glove-box.

4) Deposit active layer: 20 mg mL-1 chloroform solution of investigated molecule donors or blend with acceptors was spin-coated on top of PEDOT:PSS. Different thicknesses were achieved by different spin speeds.

5) Deposit top electrode: 7nm MoO_3 and 120 nm Ag were thermal evaporated on the top of the active layer under vacuum ($< 10^{-6}$ mbar). The top electrode has three sizes of surface: 2.25×10^{-2} mm², 6.25×10^{-2} mm² and 2.5×10^{1} mm².

Electrical characterization

Devices were then measured on a probe station equipped with an optical microscope in a glovebox. The current-voltage responses were recorded by the same Keithley 4200 semiconductor characterization system as OFET measurements.

Temperature dependence characterization

The SCLC devices were further measured at various temperatures. The temperatures were adjusted by a Peltier thermo-module. Unlike OFETs, SCLC device was placed directly on the Peltier module, measured by four-points station every 10°C, from -10°C to 50°C.

4.2.4 Photovoltaic properties: organic solar cells

4.2.4.1 Organic solar cell device elaboration

Bulk heterojunction devices were elaborated using the different synthesized molecules as electron donor and $PC_{71}BM$ as electron acceptor. Inverted solar cells using PEIE as an interfacial layer were elaborated. The device structure was the following: ITO/PEIE(5 nm)/ Donor:$PC_{71}BM/MoO_3$ (7 nm)/Ag (120 nm). ITO coated glass with a surface resistance lower than 20 Ω/sq was used as transparent substrate.

The solar cells elaboration procedures are as follow:

1) Clean substrates: glass-ITO substrates were cleaned sequentially by ultrasonic treatments in acetone, isopropyl alcohol, and deionized water at 45°C for 15 minutes.

2) UV-ozone treatment: An additional clean was conducted under ultra-violet generated ozone for 30 minutes.

3) Deposit PEIE: PEIE (M_W=70000 g/mol) was spin-coated (5000 rpm, 60s) to obtain a 5 nm thick layer and thermally annealed for 10 minutes at 100°C.

After this step, the samples were transferred into the nitrogen-filled glove-box.

4) Deposit active layer: the chloroform solutions of molecule donor:$PC_{71}BM$ were stirred for at least 24 hours at RT before spin-coating. The donor solution concentrations were of 5 mg.mL^{-1}. The relative donor:$PC_{71}BM$ weight ratio was varied from 1:1 to 1:5. The active layer spin coating conditions were the following: a first 120 seconds step (speed: 2000 rpm, acceleration: 600 rpm.s^{-1}) followed by a second 60 seconds step (speed: 2500 rpm, acceleration: 600 rpm.s^{-1}). A post-deposition thermal annealing process (for 10 minutes at 80°C) was added before the anode thermal evaporation.

5) Evaporate anode: A MoO_3 (7 nm)/Ag (120 nm) bi-layer was thermal evaporated under pressure (< 1×10^{-6} mbar). Each device contained four 12 mm^2 diodes, the surface of each diode being carefully defined by a shadow mask.

4.2.4.2 Solar cells characterization

The current supplied by a solar cell as a function of voltage is measured using a source measurement unit Keithley 2400 initially in the dark and then under AM1.5G[a] illumination.

These standard measurement conditions correspond to an incident light power of 1000 W.m^{-2} at 25 ° C. In the laboratory, illumination is usually provided by a solar simulator using a Xenon lamp equipped with a filter to create AM1.5G conditions. The standard illumination was provided by a Class A Lot Oriel solar simulator (550 W filtered Xe lamp) and the illumination power was calibrated using a reference silicon solar cell. Calibrated silicon reference cells were used to monitor the incident and the reflected light power for each wavelength. The photovoltaic cells characterizations were performed in nitrogen ambient.

All the main parameters of measured organic solar cells (including V_{oc}, J_{sc}, FF, PCE), along with shunt resistance (R_{SH}) and series resistance (R_S) were extracted by the LabView software. The main parameters were introduced in chapter 2, shunt resistance (R_{SH}) was given by the inverse slope of dark J-V curves at V = 0 V:

$$R_{SH} = \left. \frac{dV}{dI} \right|_{V=0} \qquad\qquad (4\text{-}16)$$

Series resistance R_S was extracted from the slope of dark J-V curves at $V=V_{oc}$, which is the same operating condition of solar cells:

$$R_S = \left. \frac{dV}{dI} \right|_{V=V_{OC}} \qquad\qquad (4\text{-}17)$$

---

[a] AM stands for air mass coefficient, it is used to characterize the solar spectrum after solar radiation has traveled through the atmosphere. AM1.5 corresponds to a solar zenith angle of 48.2°, and it is used for standardized testing terrestrial solar cells.

CHAPTER 5
Results: Molecular & bulk material properties

In this chapter, the characterization of molecular and bulk material properties of a series of dumbbell-shaped molecular donors are intensively investigated. Those molecules, noted as TPD-TAT, use a thienopyrroledione (TPD) unit as central core, and are end-capped by two triazatruxene (TAT) units.

First, cyclic voltammetry (CV) measurements of the electrochemical properties are presented. In the second part, Ultraviolet-visible (UV-vis) spectroscopy measurements are shown that provide information about electronic transitions. In the next section, differential scanning calorimetry (DSC) measurements that have been done to study the thermal property of the compounds are described. At last, small angle X-ray Scattering (SAXS) results are shown and used to determine the microstructure of the bulk materials.

5.1 Electrochemical property: Cyclic Voltammetry

The cyclic voltammetry (CV) technique was applied to analyze the electrochemical properties. In particular, the measurements allow us to estimate the frontier molecular orbital (FMO) energy levels of the investigated

molecules, which are of importance in order to evaluate their potential as electron donor material in BHJ photovoltaic devices. The CV measurements were performed in dichloromethane solutions (see Chapter 4 for experimental details) All four compounds have almost identical CV signatures (shown in Figure 5-1), indicating similar HOMO and LUMO levels, at - 5.3 and -3.3 eV, respectively. The corresponding electrochemical band-gap equals 2.0 eV (Table 5-1). This value suggests that those molecules can be applied efficiently as electron donor for BHJ solar cells with fullerene acceptors. Indeed, the energy band-gap is similar to that of the well-known P3HT (efficiency over 6 % have obtained for P3HT:fullerene BHJ devices[104,105]). For $PC_{71}BM$, the HOMO and LUMO values measured in similar conditions are -5.8 eV and -4.2 eV, respectively[18]. The LUMO offset for the electron-acceptor and the electron-donor therefore equals 0.9 eV, which is sufficiently high to promote the exciton dissociation. Moreover, as introduced in Chapter 2, the open-circuit voltage (V_{oc}) in BHJ solar-cells is expected to follow equation 5-1:

$$V_{oc} = \frac{1}{e}(HOMO_D - LUMO_A) - 0.3\,V \qquad\qquad (\;5\text{-}1\;)$$

Therefore, all compounds should give rise to higher Voc values than P3HT. (expected value ≈ 0.8 V, to be compared to the typical 0.6V observed with P3HT, whose HOMO is around -5 eV).
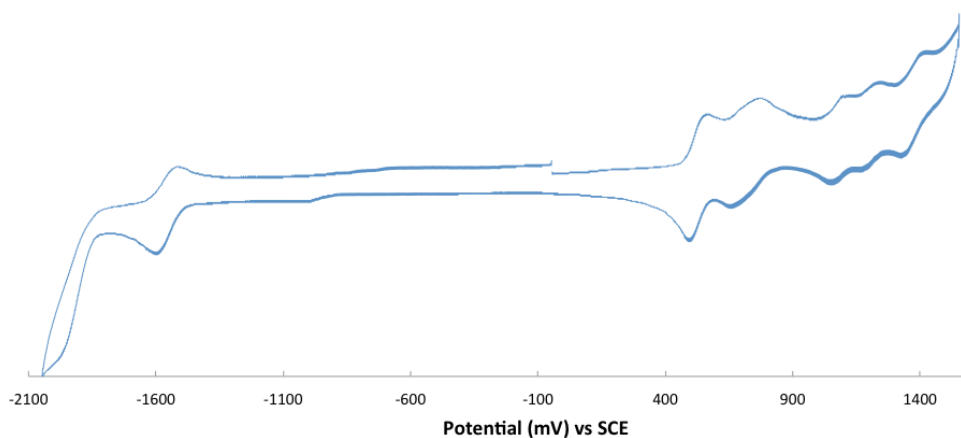

Figure 5-1: Cyclic voltamogram of TPD-TAT dyes in dichloromethane at rt. 1.5 mM substrate in 0.10 M Bu4NPF6.

Table 5-1: Opto-electronic properties of TPD-TAT dumbbell-shaped molecules.

Molecule	HOMO (eV)	LUMO (eV)	$E_{gap\ opt}$ (eV)
TPD_{C8}-TAT_{C8}	-5.3	-3.3	2.0
TPD_{EH}-TAT_{C8}	-5.3	-3.3	2.0
TPD_{C8}-TAT_{EH}	-5.3	-3.3	2.1
TPD_{EH}-TAT_{EH}	-5.3	-3.3	2.1

5.2 Optical property: UV-visible spectroscopy

The UV-visible absorption both in solution and in thin films of the TAT-based dumbbell-shaped molecules are shown in Fig. 5-2. The absorption spectra measured in chloroform solutions overlap almost perfectly (Fig. 5-2 top and Table 1), revealing that the charge delocalization is not affected by the side chains. We may therefore conclude that both, linear and branched chains do not affect the molecular conformation and the related conjugation length in solution. The strong absorption peak at about 320 nm (ε = 145,000 $M^{-1}cm^{-1}$) may be assigned to π-π^* transitions of the fused tris-carbazole (i.e. TAT) platform[92,106], while the broad absorption band around 500 nm (ε = 73,000 $M^{-1}cm^{-1}$) is likely due to an internal charge transfer between the electron-rich TAT unit and the electron-deficient TPD unit.

In the solid-state, all the spectra are red-shifted and broadened, with a clear impact of the side-chain nature on the optical properties (Fig. 5-2 bottom). Indeed, the absorption spectra of molecules with ramified side-chains on the TAT moieties (i.e. TPD_{C8}-TAT_{EH} and TPD_{EH}-TAT_{EH}) show a weak bathochromic shift (20 nm) with almost no vibronic structure, while the spectra of the molecules with linear chains on the TAT units (i.e. TPD_{C8}-TAT_{C8} and TPD_{EH}-TAT_{C8}) exhibit larger red-shifts (35 nm and 40 nm, respectively) and include marked vibronic peaks. The thin film optical band gaps are estimated to 2 eV and 2.1 eV for TAT_{C8} and TAT_{EH} based molecules respectively.

These results suggest that linear chains on the TAT units lead to a higher structural order (better defined vibronic features) and more pronounced intermolecular interactions (larger red-shift) in the solid state. On the other hand, the TPD substitutions do not change notably the optical properties. These

findings give therefore evidence that the intermolecular interactions of these dumbbell-shaped molecules are controlled mostly by the side chains on the TAT units, and, as a corollary, that the TAT packing are the major driving force for the molecular self-assembly.
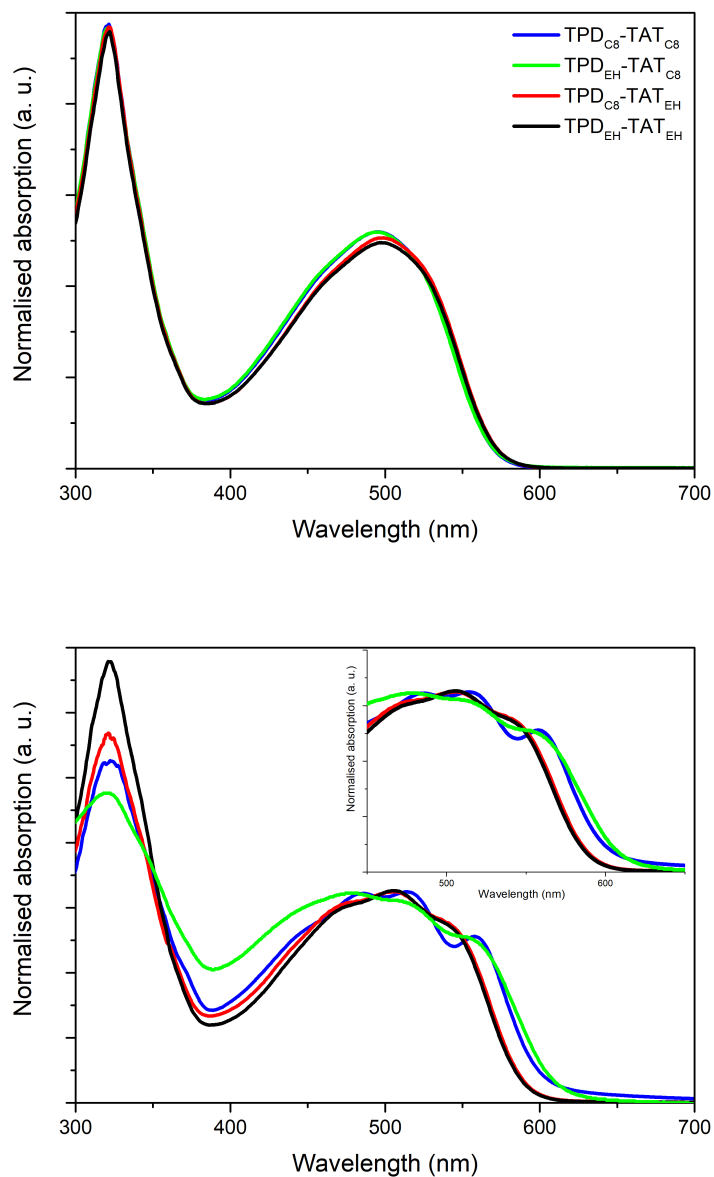

Figure 5-2: Normalized absorption in chloroform solution (top) and in thin-film (bottom) of TPD-TAT molecules (in onset, zoom in on the ICT bands). The normalization has been performed on the ~500 nm absorption peak.

5.3 Thermal properties: Differential Scanning Calorimetry

The different self-assembling behaviors of TAT_{EH} and TAT_{C8} platforms loom large in the polymorphism of the four samples, which was investigated by polarized optical microscopy (POM) and differential scanning calorimetry (DSC) (see Figure 5-3). The molecules bearing TAT_{EH} units only show the isotropic glass and liquid states with a glass transition at 75-80°C, while those bearing TAT_{C8} exhibit a rich polymorphism depending on thermal history (Table 5-2). Specifically, the initial frozen birefringent state flows to a fluid nematic phase on crossing the glass transition, which is located at the same temperature as for TAT_{EH} analogues. The transition to the isotropic liquid state is then reached at 156-158°C, and the fluid and glassy states of the nematic phase are successively re-obtained on cooling. The liquid-crystalline phase is however metastable and a slow crystallization process occurs on second heating above the glass transition. This crystalline phase melts at 165-170°C, thus above the clearing temperature in the nematic state, which is therefore a monotropic phase in the sense that it can only be obtained on cooling from the isotropic liquid, but not on heating from the crystal. In any case, phase sequences are the same with nearly identical transition temperatures for TPD_{C8}-TAT_{C8} and TPD_{EH}-TAT_{C8}, confirming that the molecular organization is driven by the peripheral chains on TAT units, whatever the nature of the chain on TPD.
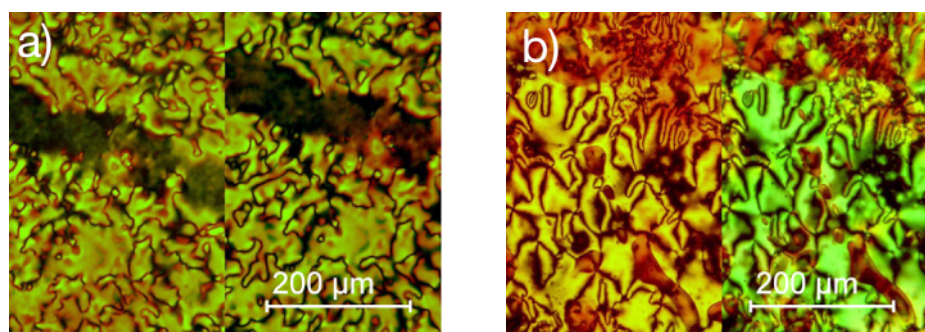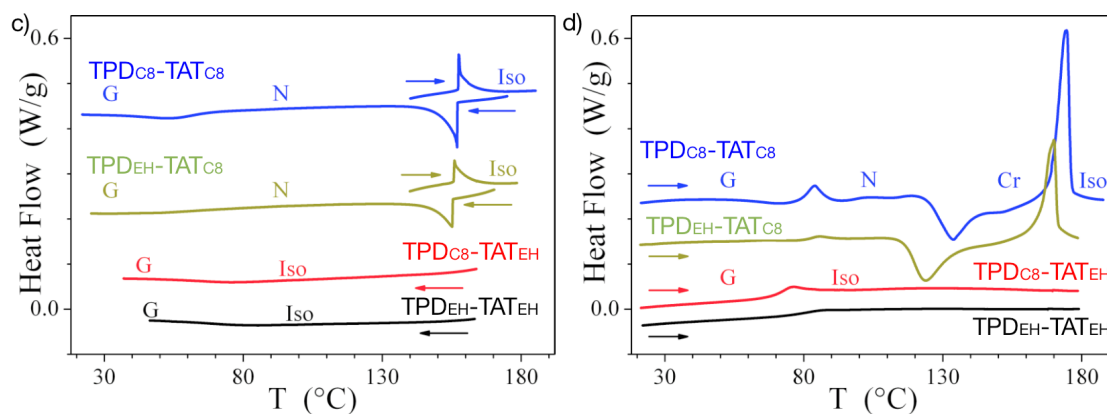
Figure 5-3: POM: typical nematic schlieren textures observed for the liquid-crystalline phase of TPD$_{C8}$-TAT$_{C8}$ (a) and TPD$_{EH}$-TAT$_{C8}$ (b), at 150°C in the fluid state, and at 20°C in the glassy state (half-images left and right, respectively); bottom, DSC: (c) cooling runs from the fluid isotropic liquid state (Iso) and 3rd heating runs from the fluid nematic phase (N) at 125°C; (d) 2nd heating runs from glassy nematic or isotropic room temperature states (G); Cr: crystalline phase; ramp conditions: 5°C/min, endotherm up.

Table 5-2: Phase transition temperatures and associated enthalpy changes from DSC second and third heating runs of TPD-TAT dumbbell-shaped molecules. G: glassy state or glassy nematic state; N: fluid nematic state; Cr: crystalline phase; Iso: isotropic liquid phase.

Molecule	Transition	Temperature (°C)	ΔH (kJ/mol)
TPD$_{C8}$-TAT$_{C8}$	G→N	80	--
	N→Cr	158	4.0
	Cr→Iso	170	45.0
TPD$_{EH}$-TAT$_{C8}$	G→N	80	--
	N→Cr	156	3.9
	Cr→Iso	165	19.0
TPD$_{C8}$-TAT$_{EH}$	G→Iso	75	--
TPD$_{EH}$-TAT$_{EH}$	G→Iso	80	--

5.4 Structural properties: Small Angle X-ray Scattering

Small Angle X-Ray Scattering experiments (SAXS) in the glassy room-temperature and the cold crystalline states reveal differences in molecular self-organization, depending on the alkyl side-chains grafted on the TAT moieties (Figure 5-4 a, b).

When TAT units are bearing linear chains (i.e. TPD$_{C8}$-TAT$_{C8}$ and TPD$_{EH}$-TAT$_{C8}$), the SAXS patterns in the frozen mesophase (shown in Figure 5-4a are typical of a nematic columnar organization, with two characteristic broad wide-angle scattering maxima from lateral distances between molten chains (h_{ch}~4.5 Å) and between face-to-face piled conjugated segments (h_{π}~3.8 Å), besides a strong

peak at small-angles (D_{col}~18 Å) due to average distances between TAT columns spaced by aliphatic and TPD moieties. An illustration of the nematic column structure is shown in Figure 5-5, where the blue triangles represent the TAT units, which pile up into in-plane columns. Note that each molecule contributes to two columns. All the columns are thus interconnected by conjugated bridges, which should translate into a 3D charge transport network. Indeed, transport perpendicular to the columns should be supported by the "intra-molecular" transport along the bridging molecules, whereas efficient inter-molecular π-π stacking interactions among TAT units should favor transport along the columns. After cold crystalline (Figure 5-4b) of the molecules with linear side chains on TAT, additional peaks appear while the dominant Bragg peak D_{col} is slightly shifted to lower angles, the corresponding crystalline structure is still under investigation.

On the other hand, when TAT units are bearing ramified side chains (i.e. TPD$_{C8}$-TAT$_{EH}$ and TPD$_{EH}$-TAT$_{EH}$), the patterns are characteristic of amorphous compounds in both glassy state and cold crystalline state, with in particular disappearance of the π-stacking maximum and persistence of a unique broad signal for lateral distances between conjugated and aliphatic segments h_c+h_{ch}. The alternation of zones containing each type of antagonistic segments persist at the local range, as proven by the presence of a diffuse small-angle scattering (D~10 to 20 Å).

In conclusion, the differences of polymorphism and molecular packing in the series comes down essentially to a supramolecular organization of TAT columns induced by C_8 chains, versus the absence of supramolecular association with EH chains. This fact is likely to originate from the different cross-sections of both chain types, which is the double for EH (42-43 Å² at 20°C), so that the overall cross-section of three ramified chains would exceed the envelope area of the TAT columns, preventing de facto the formation of the columns. With C_8 chains, the piling up is on the contrary authorized and thus the arrangement of the so-formed columns into nematic phase. Moreover, the close-packing along columns presumably initiates the crystallization process on second heating,

explaining that this happens only with TAT_{C8}. Regarding the chain borne by TPD, its insertion in the periphery of columns does not impact the piling of TAT units, but could just influence the arrangement of the columns through its contribution to the overall volume. However, the partial volume of EH and C_8 chains differ by less than 1%, and the nature of the chain of TPD has hence no importance, in accordance with experimental findings.

In short, the design of the alkyl chains grafted on the TAT units is crucial for the molecular organization while the chain on TPD has only a minor role.
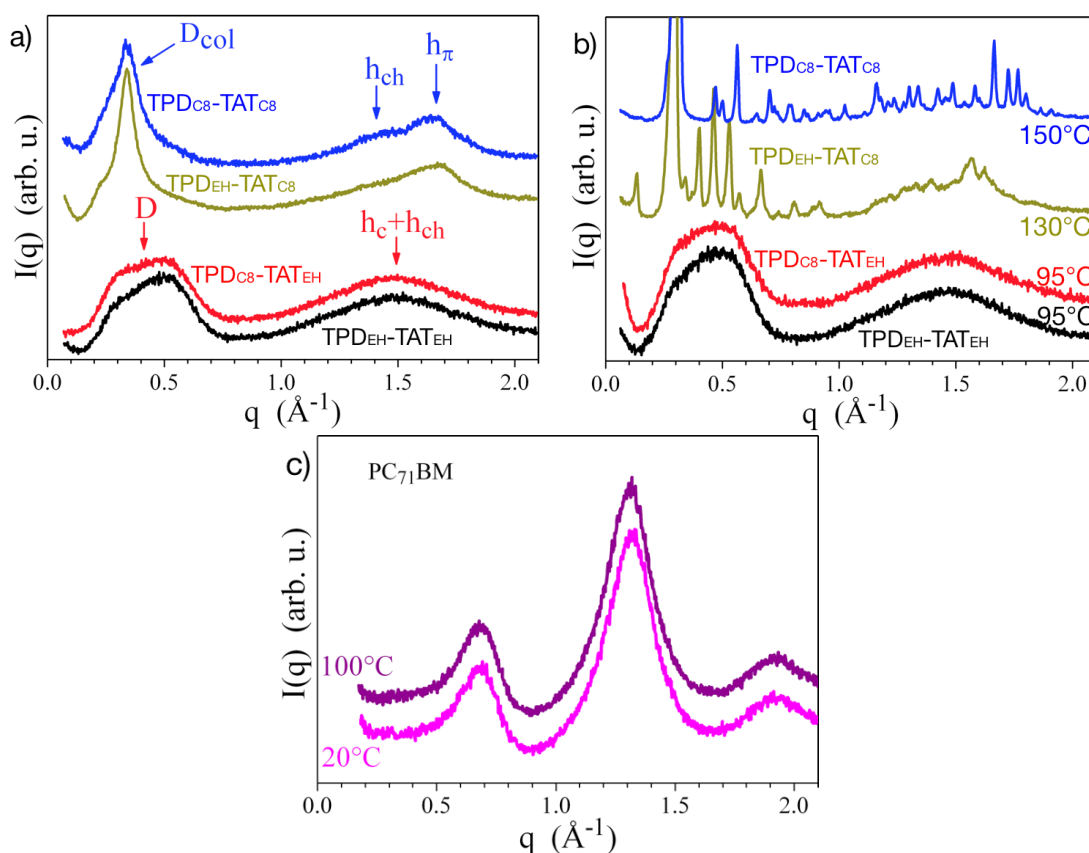
Figure 5-4: SAXS patterns measured a) on pure TPD-TAT materials at room-temperature; b) on TPD_{C8}-TAT_{C8} at 150°C and TPD_{EH}-TAT_{C8} at 130°C, after their cold crystallization; TPD_{C8}-TAT_{EH} and TPD_{EH}-TAT_{EH} in the isotropic liquid at 95°C; C) on PC71BM at 20°C and 100°C.
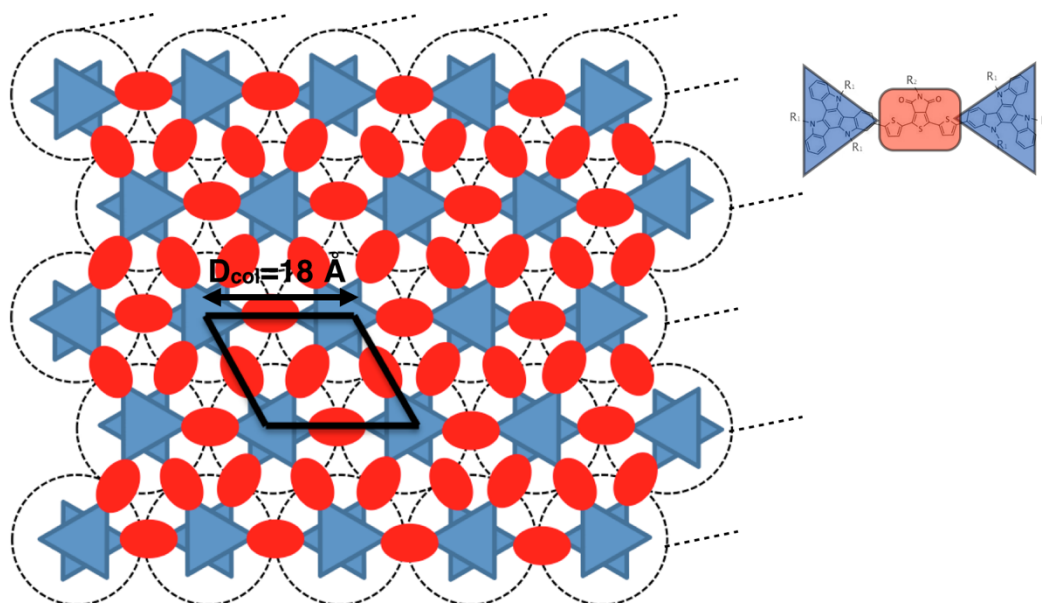
Figure 5-5: Illustration of nematic column structure for TPD_{C8}-TAT_{C8} and TPD_{EH}-TAT_{C8}, where the red parts represent TPD core and the blue tringles represent TAT units.

5.5 Conclusion

In summary, through the investigation of molecular and bulk material properties, we demonstrated that all the molecules have the same HOMO and LUMO levels. And their absorption properties in solutions do not affected by the side-chains. However, the absorption in thin-films suggests that linear chains on the TAT units lead to a higher structural order and more pronounced intermolecular interactions in the solid state. On the other hand, the TPD substitutions do not change notably the optical properties. As a matter of fact, the molecular self-assembling appeared to be driven by the stacking of TAT units and consequently, the bulkiness of the chains connected to them: the linear chains led to nematic and crystal phases, while the bulkier branched ones led to amorphous states. The nature of the chain on TPD has on the contrary no significant influence. In the step, charge mobilities will be measured to understand the influence of structure ordering on the charge carrier transport.

CHAPTER 6
Results: Charge transport measurements

Based on our previous work on the molecular properties, we found that TPD-TAT molecules are promising donor materials for BHJ solar cells. Apart from molecular properties, charge carrier transport is another important key parameter for solar cell applications. Therefore, in the first part of this chapter, charge transport measurements of pure TPD-TAT molecules at different states will be presented. In the second part, the temperature dependent mobilities of the most interesting molecule, TPD_{C8}-TAT_{C8}, will be investigated.

6.1 Mobilities of TPD-TAT molecules

6.1.1 In-plane mobility measured by OFETs

6.1.1.1 As-deposited mobilities

In-plane charge-carrier mobility measurements have been performed on both as-deposited and crystalline TPD-TAT thin films using top-contact/bottom-gate organic field-effect transistor (OFET) structures. Please refer to Chapter 4 for detailed elaboration procedures. The transistor transfer characteristics in the

linear regime are shown in Figure 6-1, while the output and transfer characteristics (in the saturation regime) are shown in Figure 6-2 and 6-3a respectively.

The in-plane mobilities were extracted from the OFET transfer characteristics in the saturation regime. Mobilities in the linear regime could not be extracted because of a large contact resistance (R_c) and hysteresis (Figure 6-1). Note in particular that at high gate voltages ($|V_{gs}| > 40$ V), the drain current I_{ds} decreases significantly due to the contact resistance R_c. The high R_c value is at least partly due to the energy offset between contact metal work function (close to 5 eV) and the deep HOMO level of the TPD-TAT molecules and/or to a "poor" metal/organic interface. Note that the effect is most pronounced in the crystalline phase. This will be further discussed in Chapter 8.

Figure 6-3 shows the $I^{1/2}$ as a function of V_{gs} in saturation regime. We observe that the curves are no longer linear when $|V_{gs}| > 40$ V. At high Vgs, channel resistance R_{ch} is lower and therefore the contact resistance R_c affects most the drain current. As a result, the saturation mobility is extracted from the linear part of the curve. By comparing the transfer curves in saturation regime and linear regime, we note that the hysteresis is much lower and that R_c has minor impact in the saturation regime (high V_{ds}). A possible reason for lower R_c is the barrier narrowing under high V_{ds}. The impact of R_c on the mobility values will be further addressed in detail in section 6.1.1.3.
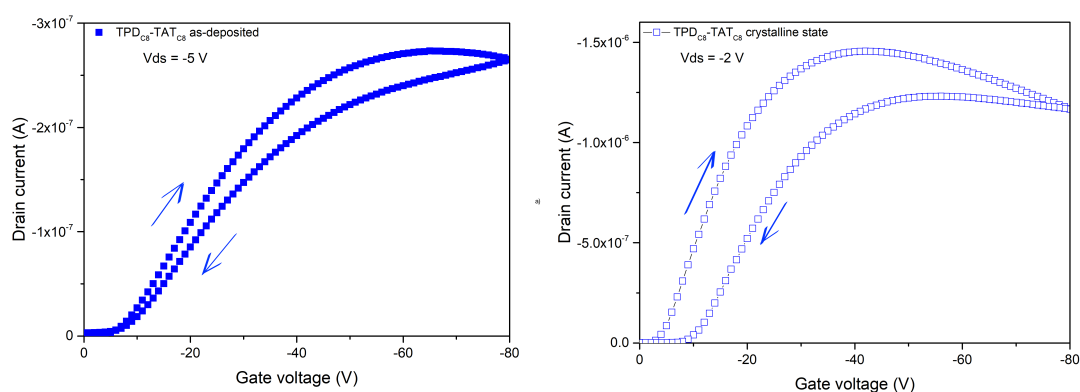

Figure 6-1: Transfer curve in linear regime of as-deposited TPD$_{C8}$-TAT$_{C8}$ thin films (left) and in crystalline state (right).

The extracted field-effect mobilities of all TPD-TAT molecules in the as-deposited state are summarized in Table 6-1. Among the four molecules, TPD_{C8}-TAT_{C8} has the highest hole mobility of $(2.8\pm1) \times 10^{-4}$ $cm^2 V^{-1} s^{-1}$, almost one order of magnitude higher than the other three molecules (around $3\text{-}4 \times 10^{-5}$ $cm^2 V^{-1} s^{-1}$). These results are not fully in line with UV-visible absorption and SAXS patterns in the previous chapter, which suggested that both molecules with linear C_8 chains on TAT exhibit similar molecular properties. A possible reason is that OFET charge transport measurements are more sensitive to minor differences in the molecular assembly, in particular near the interface with the dielectric.

Table 6-1: OFET hole mobility values for TPD-TAT thin films at as-deposited and crystalline state.

Molecules	μ_{hole} ($cm^2 V^{-1} s^{-1}$) OFET	
	as-deposited	crystalline state
TPD_{C8}-TAT_{C8}	$(2.8 \pm 1) \times 10^{-4}$	$(6.2 \pm 2) \times 10^{-3}$
TPD_{EH}-TAT_{C8}	$(4.9 \pm 2) \times 10^{-5}$	$(7.9 \pm 1) \times 10^{-6}$
TPD_{C8}-TAT_{EH}	$(2.6 \pm 0.1) \times 10^{-5}$	--
TPD_{EH}-TAT_{EH}	$(4.5 \pm 0.4) \times 10^{-5}$	--

6.1.1.2 Crystalline state mobilities

The crystalline state of TPD-TAT_{C8} molecules was achieved by thermal annealing at 100°C for 5 minutes, 120°C for 5 minutes and 130°C for 5 minutes (cold-crystallization shown in the DSC curve Figure 5-3). In this state, the hole mobility of TPD_{C8}-TAT_{C8} increases to $(6.2\pm2) \times 10^{-3}$ $cm^2 V^{-1} s^{-1}$, which is over 20 times higher than before annealing, indicating a more ordered molecular organization (comparison of transfer curve shown in Figure 6-3 b). However, for TPD_{EH}-TAT_{C8} the mobility in the crystalline stat is lower than in the as-deposited mobility. This unusual trend might be caused by the poor morphology after crystallization (see Chapter 8).

We would like to emphasize that the rather moderate in-plane hole mobility values do not predestine the BHJ solar cell efficiencies, since the photovoltaic energy conversion is dependent mostly on charge transport across the film (i.e.

the bulk mobility). It is therefore essential to study the out-of-plane hole mobility as well.
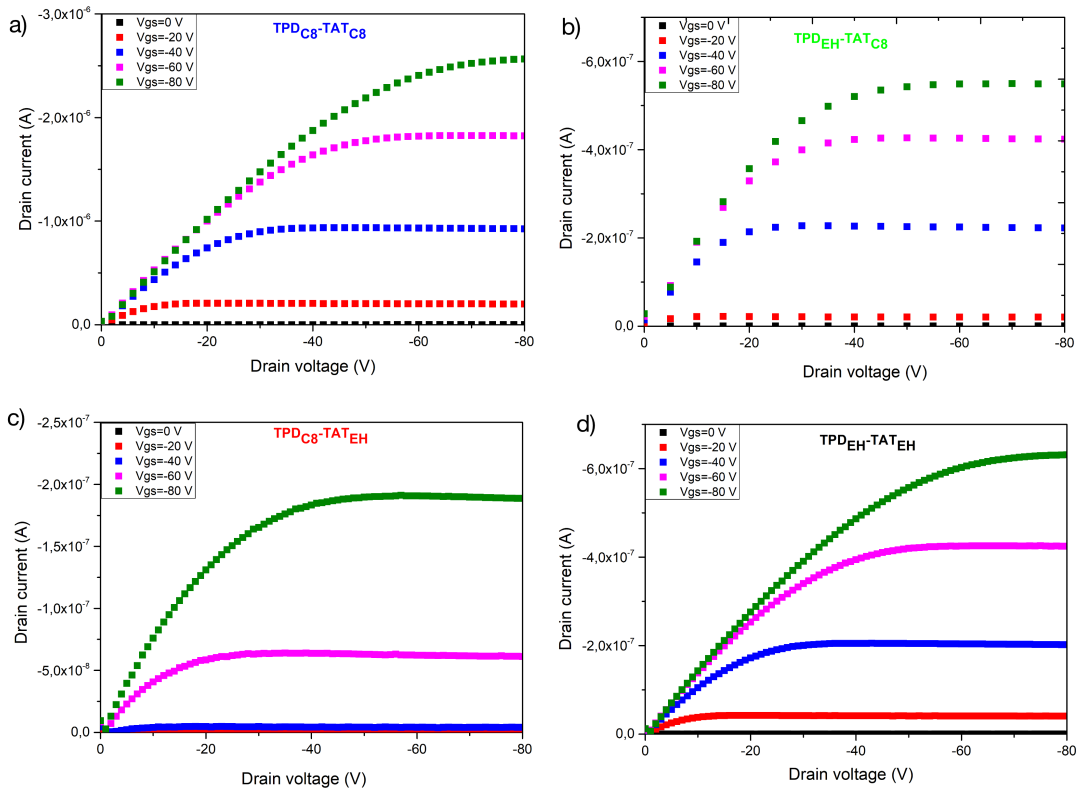
Figure 6-2: Output characteristics of TC-BG OFETs based on pure as-deposited (a) TPD_{C8}-TAT_{C8}, (b) TPD_{EH}-TAT_{C8}, (c) TPD_{C8}-TAT_{EH} and (d) TPD_{EH}-TAT_{EH} thin films.
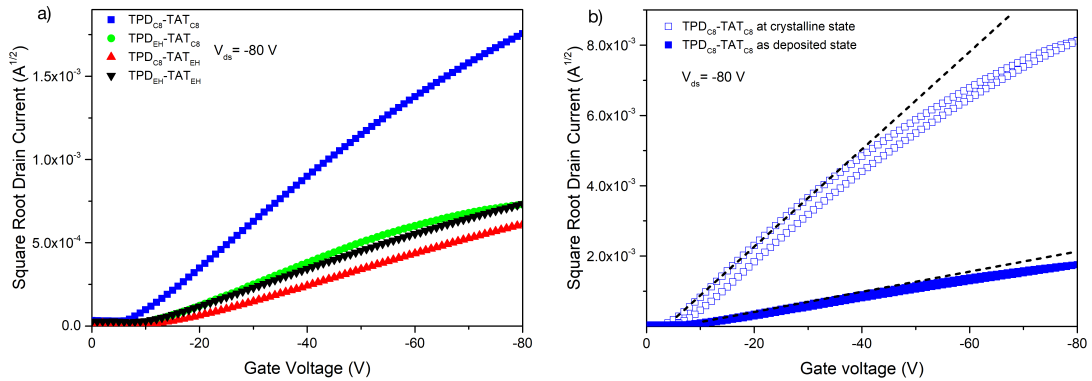
Figure 6-3: Transfer curve in saturation regime at V_{ds} = -80 V of (a) as deposited TPD-TAT thin films; (b) TPD_{C8}-TAT_{C8} in as-deposited and crystalline states.

6.1.1.3 Contact resistance

Contact resistance effects can be seen in both output and transfer characteristics of OFET at high gate voltages. In a P-type OFET, holes are injected into the HOMO level. As already mentioned above, the injection barrier depends on the difference between the work function of the metal contact and the HOMO level

of the semiconductor. If this energy barrier is negligible, an ohmic contact is obtained. On the opposite, a large energy barrier leads to a significant voltage drop at the metal/semiconductor interface. Therefore, the voltage drop and, as a consequence, the in-plane electric field along the channel are reduced, leading to a lower drain current. The hole mobilities extracted with the standard transistor model are thus under-estimated if R_c gets close to the channel resistance (i.e. at high gate voltages).

If R_c is not too high, it is possible to get a better estimate of the mobility by taking the voltage drop at the Metal/Semiconductor interface into account.

To measure the contact resistance, we used the Transfer Line Method (TLM) by studying the device resistance as a function of channel length. The total resistance (R_{total}) can be approximated by the sum of the contact resistance (R_c) and the channel resistance (R_{ch}):

$$R_{total} = R_c + R_{c\square} = \frac{V_{ds}}{I_{ds}} \qquad (6\text{-}1)$$

In linear regime, the OFET channel resistance R_{ch} is given by:

$$R_{c\square} = \frac{L}{W \cdot \mu \cdot C_i \cdot (V_{gs} - V_T)} \qquad (6\text{-}2)$$

On the other hand, the total resistance can be estimated from the out-put characteristics at low V_{ds} by the following: $R_{total} = \left.\frac{dV_{ds}}{dI_{ds}}\right|_{V_{ds}\to 0}$.

Therefore, by measuring several OFETs with different channel lengths on the same semiconductor film, we can use the linear extrapolation of the resistance versus channel length plot to L=0 to estimate the contact resistance[107].

For TPD$_{C8}$-TAT$_{C8}$ based OFETs, R_{total} was calculated for V_{gs} = -80 V with three different channel length (L= 60, 80 and 100 μm). Then R_{total} versus L is plotted in Figure 6-4, and lead to contact resistance of roughly 1.1 MΩ.

Based on equation 6-1 and 6-2, the corrected mobility calculated for TPD$_{C8}$-TAT$_{C8}$ at crystalline state can be expressed as:

$$\mu_{corrected} = \frac{L}{W \cdot C_i \cdot (R_{total} - R_c) \cdot (V_{gs} - V_T)} \qquad (6\text{-}3)$$

where V_T is around -20 V according to the transfer curve in the saturation regime (Figure 6-3). Finally, an average $\mu_{corrected}$ of 6.1×10^{-3} cm^2 V^{-1} s^{-1} is obtained, which is close to the mobility estimated from the transfer curve in the saturation regime (in the linear part of Fig 6-3b) without taking into account R_c (6×10^{-3} cm^2 V^{-1} s^{-1}).
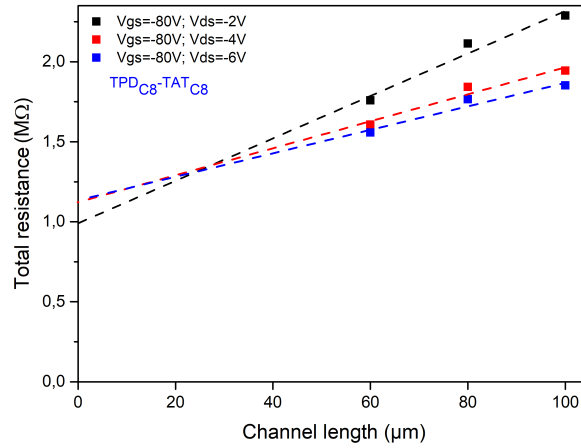
Figure 6-4: Total resistance versus channel length plot for the top-contact/bottom-gate OFETs based on TPD$_{C8}$-TAT$_{C8}$ thin film.

6.1.2 Out-of-plane mobility measured by SCLC devices

6.1.2.1 As-deposited mobilities

Out-of-plane hole mobilities for all TPD-TAT molecules were measured by space-charge-limited-current (SCLC) diodes. Standard device structure ITO/PEDOT:PSS/Active layer/MoO$_3$/Ag was employed. The working principle and elaboration processes have been introduced in Chapter 4.

In order to correctly evaluate the SCLC hole mobilities, devices with two different active layer thicknesses have been fabricated and measured. Figure 6-5 shows the J-V characteristics of SCLC devices based on as-deposited TPD-TAT films with two different thicknesses. According to Mott-Gurney's law, J is proportional to $\mu \cdot \frac{V^2}{L^3}$ in the SCLC regime. Moreover, the mobility may be electric field dependent, i.e. $\mu = \mu(V/L)$. Thus, to test the validity of Mott-Gurney's law,

J×L was plotted against V/L. As shown below, the curves almost collapse, indicating that the current is space-charge-limited rather than injection-limited.
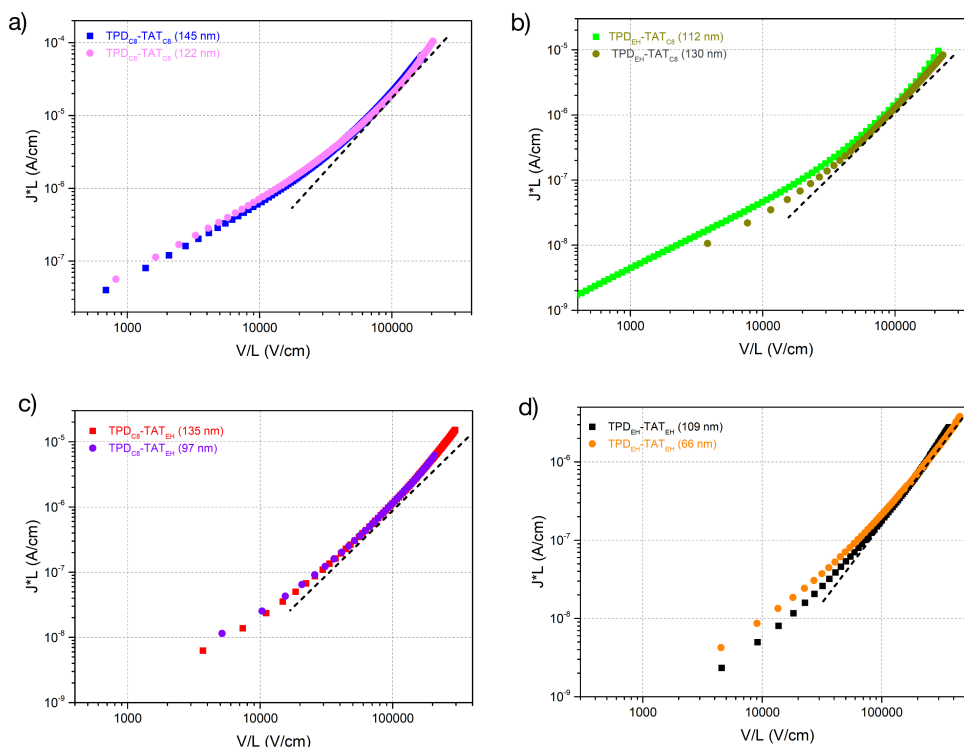
Figure 6-5: J-V characteristics of hole-only SCL diodes based on (a) TPD$_{C8}$-TAT$_{C8}$; (b) TPD$_{EH}$-TAT$_{C8}$; (c) TPD$_{C8}$-TAT$_{EH}$ and (d) TPD$_{EH}$-TAT$_{EH}$ for two different active layer thicknesses.

The J-V characteristics of the SCLC devices for all as-deposited TPD-TAT thin-films are summarized in Figure 6-6. The corresponding hole mobilities are given in Table 6-2 and are compared to the OFET mobilities. The results show a clear dependence on the TAT substituents: the SCLC hole mobility increases by a factor of 50 (from 4×10^{-5} cm^2 V^{-1} s^{-1} to 2×10^{-3} cm^2 V^{-1} s^{-1}) range, when using C$_8$ linear chain instead of EH ramified chain. On the other hand, the side-chain on the central TPD unit have a much weaker influence on the bulk mobility (30 % difference in mobility for TPD-TAT$_{C8}$ and 75 % for TPD-TAT$_{EH}$).

Table 6-2: OFET and SCLC hole mobility values for as-deposited TPD-TAT thin films.

Molecules	μ_{hole}^{SCLC} (cm^2 V^{-1} s^{-1})	μ_{hole}^{OFET} (cm^2 V^{-1} s^{-1})
TPD$_{C8}$-TAT$_{C8}$	$(2.3\pm0.8) \times 10^{-3}$	$(2.8\pm0.8) \times 10^{-4}$
TPD$_{EH}$-TAT$_{C8}$	$(1.8\pm0.7) \times 10^{-3}$	$(4.9\pm1.8) \times 10^{-5}$
TPD$_{C8}$-TAT$_{EH}$	$(4.7\pm2.9) \times 10^{-5}$	$(2.6\pm0.1) \times 10^{-5}$
TPD$_{EH}$-TAT$_{EH}$	$(3.8\pm0.9) \times 10^{-5}$	$(4.5\pm0.4) \times 10^{-5}$
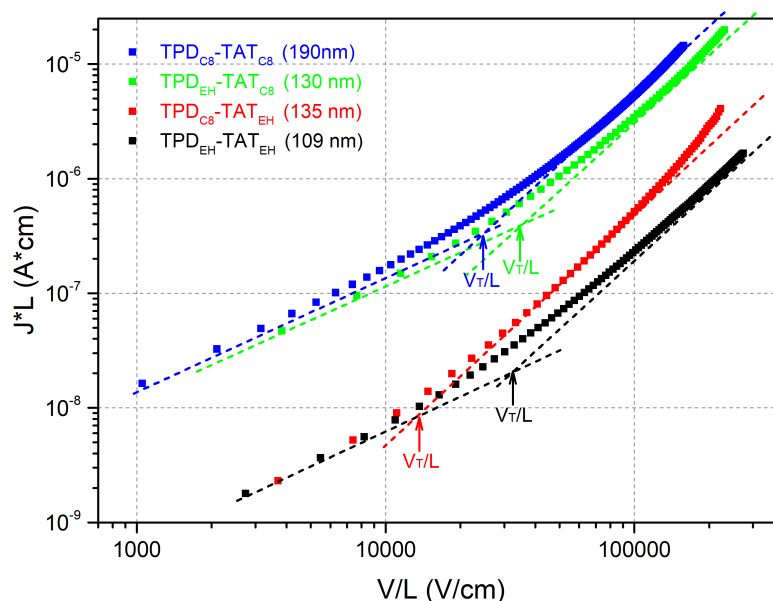
Figure 6-6: J-V measurements on SCLC devices for as-cast TPD-TAT molecule thin-films. The dashed lines at high electrical field correspond to the expected variation of J as a function of V^2. The current density and applied voltage has been scaled by the device thickness in order to highlight the difference in charge carrier mobility. V_T/L represents the crossover voltage of ohmic and SCLC part.

Those results are in line with the SAXS and spectroscopy data and conform that the stacking of TAT moieties drives the intermolecular interactions. Also, the minor influence of the TPD core on the mobility corroborates the idea that charge transport in such dumbbell-shaped molecules can be controlled at least to some extent by the planar end-groups, independently on the central dye unit.

By comparing the SCLC mobilities with the OFET mobilities (Table 6-2 a and b), we note that for TPD_{C8}-TAT_{C8} and TPD_{EH}-TAT_{C8}, the out-of-plane mobility is significantly higher than the in-plane mobility, which is uncommon (OFET mobilities in disordered organic semiconductors are generally larger than SCLC mobilities), suggesting an anisotropic charge transport. The nematic columnar structure observed by SAXS measurements (see Chapter 5) indicates that the TAT columns are oriented in-plane, while the columns are connected out-of-the-plane by TPD_{C8}-TAT_{C8} molecules, i.e. by conjugated bridges. It is likely that intra-molecular charge transport (through the conjugated bridges) is more efficient than inter-molecular transport (via hopping between neighboring TAT

units along the columns), and therefore leads to the observed charge transport anisotropy characterized by efficient out-of-plane transport.

On the other hand, for TPD_{C8}-TAT_{EH} and TPD_{EH}-TAT_{EH} molecules, both in-plane and out-of-plane mobilities are low and close to each other. This result correlates well with their amorphous structures.

Based on the above mobility values, the background charge carrier density p_o and conductivity σ can also be estimated. Indeed, in the Ohmic regime, the J-V characteristic can be expressed as:

$$J_{o\square mic} = p_0 \cdot q \cdot \mu \cdot \frac{V}{L} \qquad (6\text{-}4)$$

At V_T, defined as the crossover voltage from the Ohmic to the SCLC regime (see Fig 6-6), $J_{Ohmic} \approx J_{SCLC}$, which is:

$$p_0 \cdot q \cdot \mu \cdot \frac{V_T}{L} = \frac{9}{8} \cdot \varepsilon_0 \varepsilon_r \cdot \mu \cdot \frac{V_T^2}{L^3} \qquad (6\text{-}5)$$

This equation can be resolved for charge density by:

$$p_0 \approx \frac{8 \cdot \varepsilon_0 \varepsilon_r \cdot V_T}{9 \cdot q \cdot L^2} \qquad (6\text{-}6)$$

The values found for p_o (see table 6-3) are of the same order of magnitude for all derivatives and are similar to those reported in the literature[45,108]. The origin of the background charge carriers may be due either to carrier diffusion from the ohmic contacts[109] or to doping by residual impurities.

The p_o and mobility values can be used to calculate the film conductivity:

$$\sigma = p_0 \cdot \mu \cdot q \qquad (6\text{-}7)$$

The calculated parameters for four materials are summarized in Table 6-3:

Table 6-3: Summary of charge density and conductivity values of TPD-TAT as-deposited films in SCLC devices.

Molecules	$p_o(cm^{-1})$	σ $(S \cdot cm^{-1})$
TPD_{C8}-TAT_{C8}	$(6\pm1) \times 10^{15}$	$(2.2\pm0.4) \times 10^{-6}$
TPD_{EH}-TAT_{C8}	$(3\pm1) \times 10^{15}$	$(8.6\pm3) \times 10^{-7}$
TPD_{C8}-TAT_{EH}	$(3\pm0.4) \times 10^{15}$	$(2.2\pm0.3) \times 10^{-8}$
TPD_{EH}-TAT_{EH}	$(4\pm0.6) \times 10^{15}$	$(2.4\pm0.3) \times 10^{-8}$

The conductivity can also be calculated from the linear part of the experimental curve J-V:

$$\sigma_{measued} = \frac{J}{E} = \frac{J \cdot L}{V} \qquad\qquad (\,6\text{-}8\,)$$

Correspondingly, the mobility can be estimated also from the linear part of the J-V characteristics. The estimated mobility values are summarized in Table 6-4 below:

Table 6-4: Summary of average conductivity and mobility calculated from J-V curves of TPD-TAT as-deposited films in SCLC devices.

Molecules	σ_{calcul} $(S \cdot cm^{-1})$	μ_{calcul} $(cm^2\,V^{-1}\,s^{-1})$
$TPD_{C8}\text{-}TAT_{C8}$	4×10^{-6}	4.2×10^{-3}
$TPD_{EH}\text{-}TAT_{C8}$	4.2×10^{-7}	9×10^{-4}
$TPD_{C8}\text{-}TAT_{EH}$	3×10^{-8}	6.3×10^{-5}
$TPD_{EH}\text{-}TAT_{EH}$	1.4×10^{-8}	2.2×10^{-5}

As we can see, the calculated mobilities are in the same order than the mobilities extracted from the SCLC part, corroborating our interpretation of I-V curves.

6.1.2.2 Crystalline & nematic state mobilities

To further understand the charge carrier transport in different solid states, the SCLC mobility was measured in $TPD_{C8}\text{-}TAT_{C8}$ and $TPD_{EH}\text{-}TAT_{C8}$ thin films for both, the crystalline and the nematic phases. Both states were reached by thermal annealing: 100°C for 5 minutes - 120°C for 5 minutes - 130°C for 5 minutes to obtain the crystalline state, and 180°C for 5 seconds to reach the nematic state (this last step is believed to erase the processing history). The measured mobilities are summarized in Table 6-5.

Table 6-5 SCLC mobilities for as-deposited, crystalline and nematic state for TPD-TAT molecules.

Molecules	μ_{hole} $(cm^2\,V^{-1}\,s^{-1})$ SCLC		
	as-deposited	crystalline state	nematic state
$TPD_{C8}\text{-}TAT_{C8}$	$(2.3\pm0.8) \times 10^{-3}$	0.6 ± 0.2	$(2.9\pm0.7) \times 10^{-3}$
$TPD_{EH}\text{-}TAT_{C8}$	$(1.8\pm0.7) \times 10^{-3}$	$(1.4\pm0.4) \times 10^{-3}$	--
$TPD_{C8}\text{-}TAT_{EH}$	$(4.7\pm2.9) \times 10^{-5}$	--	--
$TPD_{EH}\text{-}TAT_{EH}$	$(3.8\pm0.9) \times 10^{-5}$	--	--

For TPD_{EH}-TAT_{C8}, the mobilities in the crystalline state remains close to the as-deposited value. This result is rather surprising, since crystallization is expected to enhance the structural order, and thus the charge transport (see also below). Unfortunately, the mobility in the nematic state could not be measured due to film dewetting at 180°C.

For TPD_{C8}-TAT_{C8} the SCLC mobility in the nematic state is around $(3\pm0.7) \times 10^{-3}$ $cm^2\,V^{-1}\,s^{-1}$, which is close to the mobility measured in the as-deposited film (see Figure 6-9). Interestingly, in the crystalline state, the measured mobility appears to be 0.6 ± 0.2 $cm^2\,V^{-1}\,s^{-1}$, which is significantly higher than what in the as-deposited and nematic states. This value is among the highest SCLC hole mobility reported so far for solution-processed small molecules (a record value of 1.4 $cm^2\,V^{-1}\,s^{-1}$ was measured in discotic liquid crystalline conjugated molecules by Gõmez-Lor *et al.*[110]).

However, a careful analysis of the data led us to the conclusion that the mobility values measured in the crystalline films are over-estimated! The reason is due to the very pronounced roughness of the crystalline films (AFM topography will be presented in Chapter 8). Indeed, while the spin-coated molecular films are smooth and have a well-defined thickness, in the range of 150 ± 50 nm, the film roughness increased considerably upon cold-crystallization. Initial thickness measurements using the profilometer (Bruker's Dektak®) led to an average thickness of 315 nm with a 60 nm roughness. These values were used to estimate the mobility given above. Yet, by investigating the film surface by AFM (see Chapter 8), we noticed that the profilometer underestimated the film roughness considerably. As a result, the film thickness and the mobility are overestimated. Since the active layer thickness appears at a power of three in Mott-Gurney's equation (equation 4-14), the accuracy of the thickness values is indeed very important. To get a better estimate of the carrier mobility in these particularly rough films, we developed a new approach based on topography data obtained by AFM.

6.1.2.3 Corrective factor on thin films with high roughness

Figure 6-7 shows an AFM image of the crystallized TPD$_{C8}$-TAT$_{C8}$ film, where some part of the film has been removed in order to obtain the planar reference level.
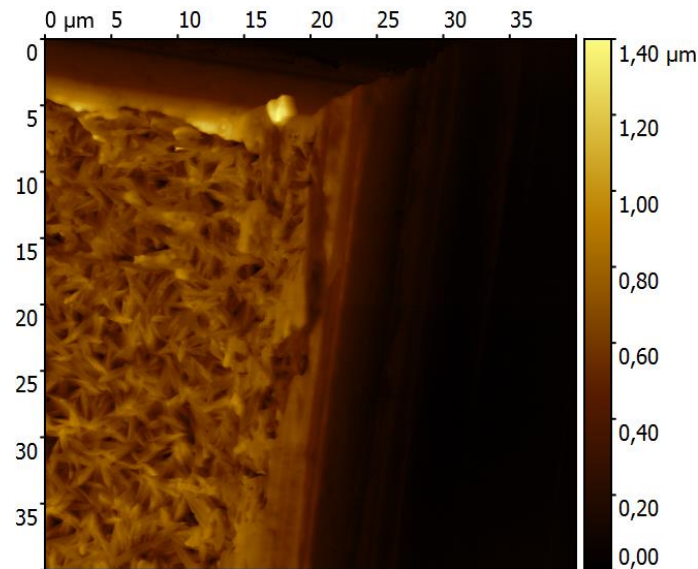
Figure 6-7: AFM image of TPD$_{C8}$-TAT$_{C8}$ film at crystalline state on a SCLC device, the right part is removed in order to get plane level.

We can observe that the TPD$_{C8}$-TAT$_{C8}$ film is indeed particularly rough. The average film thickness can be estimated from the height histogram plotted in Fig 6-8. The roughness is seen to be close to 100 nm, which is significantly larger than the value measured by the profilometer. The reason for this discrepancy may be due to the shape of the profilometer probe, which hinders the probe to follow the film topography if the high roughness occurs at a length scale of 100 nm.

In order to take into account the large roughness in the estimation of the SCLC mobility, we consider that the TPD$_{C8}$-TAT$_{C8}$ film can be divided into N segments, with each segment *i* having a constant thickness L_i and area Δs_i, (*i=1 … N),* and assume that Mott-Gurney's law can be applied to each individual segment. We also assume that the material is characterized by a constant mobility μ independent of the film thickness (i.e. spatial location) and that the transport is purely one dimensional.

The I-V characteristic can then be expressed as follows:

$$I = \sum_i J_i \cdot \ s_i = \sum_{i=1}^{N} \frac{9}{8} \varepsilon_0 \varepsilon_r \mu \frac{V^2}{L_i^3} \cdot \ s_i \qquad (6\text{-}9)$$

where J_i represents the current flowing across segment i.

If we call μ_m the mobility estimated using the standard equation (6-9) with the average film thickness L_m, i.e.:

$$I = \frac{9}{8} \varepsilon_o \varepsilon_r \cdot \mu_m \cdot \frac{V^2}{L_m^3} \cdot S \qquad (6\text{-}10)$$

and compare equation 6-9 with 6-10, we obtain:

$$\mu_m = \mu \cdot \frac{\sum_i \frac{s_i}{L_i^3}}{\frac{S}{L_m^3}} = \mu \cdot \gamma \qquad (6\text{-}11)$$

γ can be considered as a "correction" factor that takes into account the film roughness.

We further note that the average thickness is given by,

$$L_m = \sum_i f_i \cdot L_i \qquad (6\text{-}12)$$

where f_i is the probability that a segment has thickness L_i.

f_i can be estimated by measuring the film thickness distribution or histogram, for instance by AFM (see below). If the n_i represents the histogram amplitude corresponding to thickness L_i, we can write:

$$f_i = \frac{n_i}{\sum_i n_i} = \frac{n_i}{n_{total}} \qquad (6\text{-}13)$$

Also, the area Δs_i of the segment with thickness L_i is related to the total device area S by:

$$\Delta s_i = f_i \cdot S \qquad (6\text{-}14)$$

From equation 6-12, 6-13 and 6-14, we can write the corrective factor γ as:

$$\gamma = \left(\sum_i f_i \cdot L_i \right)^3 \cdot \sum_i \frac{f_i}{L_i^3} \qquad\qquad (\,6\text{-}15\,)$$

Over five different films have been measured. For each film, 3 to 4 different areas similar to those in Fig. 6-7 have been scanned. Figure 6-8 shows the height histogram of one TPD_{C8}-TAT_{C8} film at 3 different areas, calculated by using the Gwyddion software. The corresponding γ value are estimated to 0.3 ± 0.1. As a consequence, the SCLC mobility of the crystalline TPD_{C8}-TAT_{C8} film can be corrected according to $\mu_{corrected} = \mu_{measured} \cdot \gamma = 0.18 \pm 0.06 \text{ cm}^2 \text{V}^{-1} \text{s}^{-1}$.
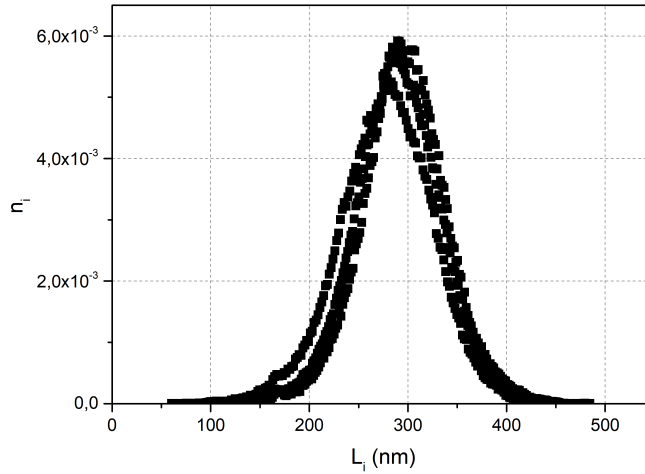
Figure 6-8: Height distributions of a crystallized TPD_{C8}-TAT_{C8} film measured by AFM, three curves correspond to three different areas on the same film.

The J-V characteristics in the crystalline state is shown in Figure 6-9, along with the characteristics at as-deposited and nematic state. We can see that the curves at as-deposited and nematic states almost collapse, which indicating similar mobilities. As expected, the amplitude of the curve in the crystalline state is significantly higher than the other curves. The black curve (characteristic at crystalline state) follows well the Mott-Gurney's law (black dashed line). However, the red and blue curves show a slight deviation from Mott-Gurney's law at higher applied voltages. This may by a signature of an electric field or charge carrier density dependent mobility, which is detailed in reference [45].
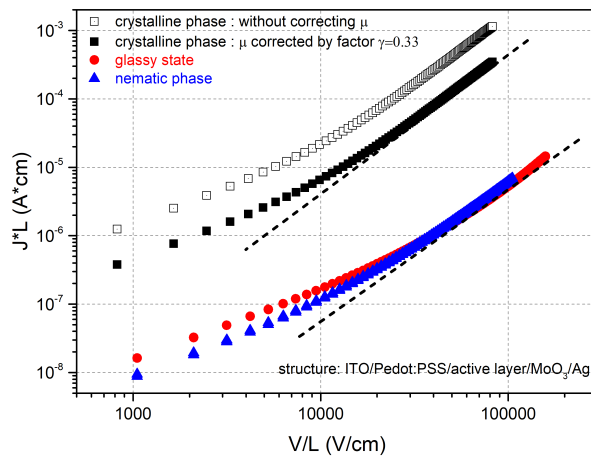
Figure 6-9: J-V characteristics of TPD_{C8}-TAT_{C8} films at crystalline state without correcting the thickness roughness (open black curve) and after correcting the thickness roughness (solid black curve); at as-deposited state (red curve) and nematic state (blue curve) on standard SCLC structure.

The same correction method has been applied to crystallized TPD_{EH}-TAT_{C8} films. The corrective factor obtained is 0.9±0.06, indicating that the TPD_{EH}-TAT_{C8} film is less rough than TPD_{C8}-TAT_{C8} film. The AFM image of etched TPD_{EH}-TAT_{C8} film is shown in Figure 6-10, if we compare it with Figure 6-7, we can conclude that the size of TPD_{EH}-TAT_{C8} crystals are much smaller than for TPD_{C8}-TAT_{C8}. As a result, the roughness is reduced, and the mobility does not change much after the correction. Importantly, the small size of the crystallites may be at the origin of the much lower SCLC mobility measured in these films, in comparison to the TPD_{C8}-TAT_{C8}.
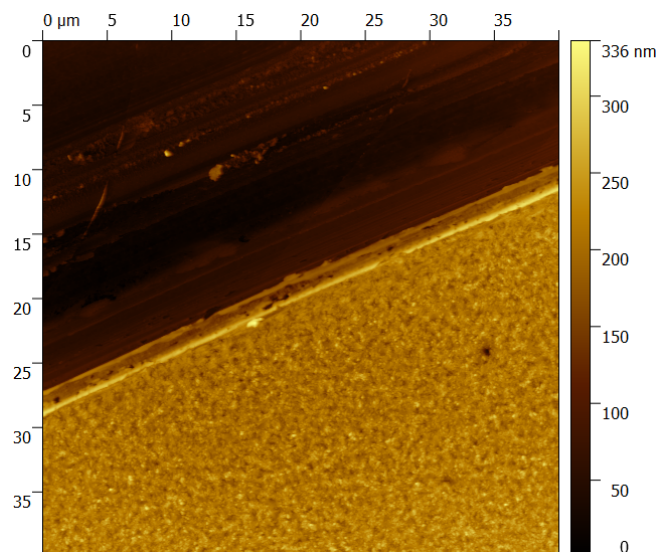
Figure 6-10: AFM image of TPD_{EH}-TAT_{C8} film at crystalline state on a SCLC device, some part of the film is removed in order to get plane level.

6.1.2.4 Sandwich structural devices with an encapsulated active layer

To cross-check the validity of the model used above to calculate the mobility on the rough film, a different device architecture composed of a thick active layer sandwiched between two Glass/ITO substrates has been developed. This device structure should allow us to avoid the issue of film roughness.

Elaboration procedures

The ITO layer of two ITO-glass substrates was structured by photo-lithography into an array of parallel, 1mm large, electrodes and used as building block of the device. The device fabrication procedure was as follow:

1) A suitable amount of molecular powder (~ 1-2 mg) was deposited on the center of an etched ITO-glass substrate. Several 20 µm thick spacers (Mica) were added on the four corners in order to define the active layer thickness (Figure 6-11, step 1);

2) The second ITO-glass substrate was put on top of the molecular powder with the electrodes being perpendicularly oriented with respect to the ITO strips of the bottom substrate (Figure 6-11 step 2).
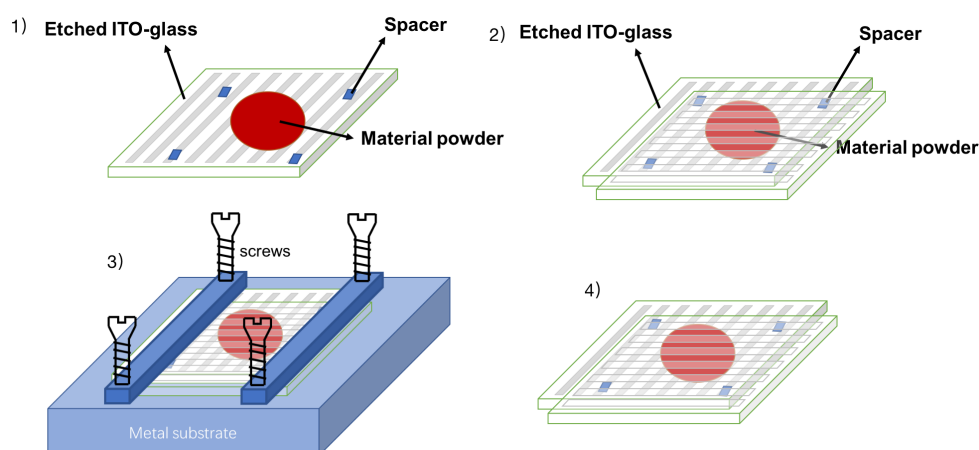
Figure 6-11: Fabrication procedures of sandwich structural SCLC devices.

3) Next, the sample was put on a metal assembly with four screws, in order to compress both substrates while heating the sample (Figure 6-11 step 3);

4) The sample was then heated above the isotropic temperature (T_{iso} ~180°C) for several minutes. While the molecules were in the liquid state and were able to spread over the device area, the screws were tightened continuously;

5) The samples were cool down to room temperature by removing the samples from the heating stage, this cooling process takes about 1 hour;

6) The sample was eventually annealed again to achieve cold-crystallization;

7) After the annealing steps, the devices were glued at the edges. The metal assembly was removed once the glue was dry (Figure 6-11 step 4).

One example is shown in Figure 6-12. A 20 μm spacer was used for this sample. The precise thickness of the active layer is 22 μm, which is calculated by the quantity of the molecule m and the active layer surface S ($L = \frac{m}{\rho \cdot S}$), assuming a volume density ρ of 0.1 mg/cm^3.
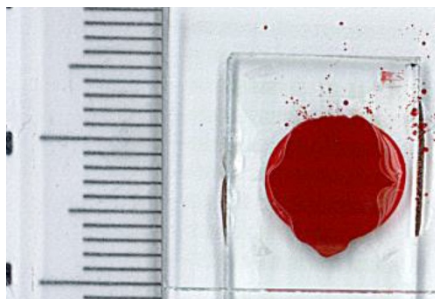
Figure 6-12: Image of a sandwiched structural SCLC device with encapsulated active layer, the substrates are glass with etched ITO (1 mm width stripes), and the red part is the deposited TPD$_{C8}$-TAT$_{C8}$ film. The active layer thickness of this sample is 22 μm and it contains 15 usable diodes.

J-V Characterization

The J-V characteristic of sandwich SCLC diodes with a TPD$_{C8}$-TAT$_{C8}$ film in both, the as-fabricated and the crystalline states (i.e. annealed at 100°C for 5 minutes - 120°C for 5 minutes - 130°C for 5 minutes), are shown in Figure 6-13.

As expected, a significant difference in the current amplitude is observed between both states. The characteristic in crystalline state is in line with the one in the same phase in standard structure device. The curves follow more or less well the Mott-Gurney's law (dashed line). For the crystalline phase, a deviation from Mott-Gurney's law is seen at higher applied voltages. This may point out that the mobility is dependent on the electric field or on the charge carrier density, although no such dependence was observed in the standard SCLC devices (Fig. 6-9). Another possibility might be injection-limited current. Indeed, the lower work-function of ITO (in comparison to PEDOT:PSS), may

lead to a charge injection barrier. Additional devices with different spacers are needed to cross-check the SCLC nature of the current. Unfortunately, these measurements have not been done yet due to limited time.

Nevertheless, the hole mobility that could be extracted from the devices with TPD_{C8}-TAT_{C8} in either as-deposited or the crystalline states are given in Table 6-6 and compared to the values measured on spin-coated TPD_{C8}-TAT_{C8} films.

In both cases, the mobilities match nicely, suggesting in particular that the model used to take into account the film roughness is appropriate. (assuming that the SCLC nature of the current in the sandwich device will be confirmed with up-coming experiments).

Importantly, the results further confirm the exceptionally high hole mobility of TPD_{C8}-TAT_{C8} in the crystalline state, highlighting the potential interest of this compound for organic electronics applications.

Table 6-6: Out-of-plane hole mobilities for crystalline, pristine and nematic TPD_{C8}-TAT_{C8} films by different device structures.

device type	$\mu_{hole}^{\text{crystalline state}}$	$\mu_{hole}^{\text{as-deposited}}$	$\mu_{hole}^{\text{nematic state}}$
spin-coating active layer	$(1.8\pm0.6) \times 10^{-1}$	$(2.3\pm0.8) \times 10^{-3}$	$(2.9\pm0.7) \times 10^{-3}$
encapsulated active layer	$(1.3\pm0.4) \times 10^{-1}$	$(3.2\pm0.5) \times 10^{-3}$	--
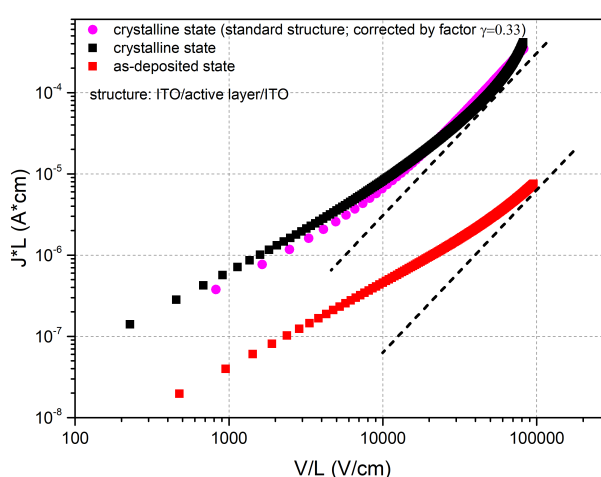
Figure 6-13: J-V characteristics of TPD_{C8}-TAT_{C8} films at crystalline state (black curve) and as-deposited state (red curve) on sandwiched structural SCLC devices, and the characteristic at crystalline state on standard structural device (magenta curve).

6.1.3 Conclusion: charge transport for TPD-TAT molecules

In summary, the charge transport measurements on TPD-TAT molecules confirm that the stacking of TAT moieties drives the intermolecular interactions: linear side-chains on TAT lead to two orders of magnitude higher out-of-plane mobilities and a one order higher in in-plane mobility compared to ramified side-chains. Also, the TPD substituent has minor influence on the mobility. Those results corroborate the idea that charge transport in such dumbbell-shaped molecules can be controlled at least to some extent by the planar end-groups, independently on the central dye unit.

In addition, the results demonstrate that the lateral π-stacking platforms (in-plane columns) of dumbbell-shaped molecules provide high stacking abilities, resulting in relatively good charge transport properties in the direction parallel to the substrate-plane (OFET mobility). Particularly, the conjugated bridges that connecting the columns provides efficient out-of-plane charge transport. Especially the most structural molecule, TPD_{C8}-TAT_{C8}, who has an extraordinary high out-of-plane mobility in the crystalline state in the order of 10^{-1} $cm^2\,V^{-1}s^{-1}$, which is among the highest SCLC mobility values reported so far for small molecular donors.

To better understand the energetics of charge transport in these molecules, temperature dependent measurements have been performed on both OFET and SCLC devices at different states.

6.2 Temperature dependent charge transport of TPD_{C8}-TAT_{C8}

6.2.1 OFET mobilities

The OFET characterization at various temperatures were conducted for both as-deposited and crystalized TPD_{C8}-TAT_{C8} films. As described in Chapter 4, the temperature was adjusted by a Peltier module and was therefore could only be varied between -10°C and 50°C. The mobility dependence on temperature are shown in Figure 6-14 for both solid states.
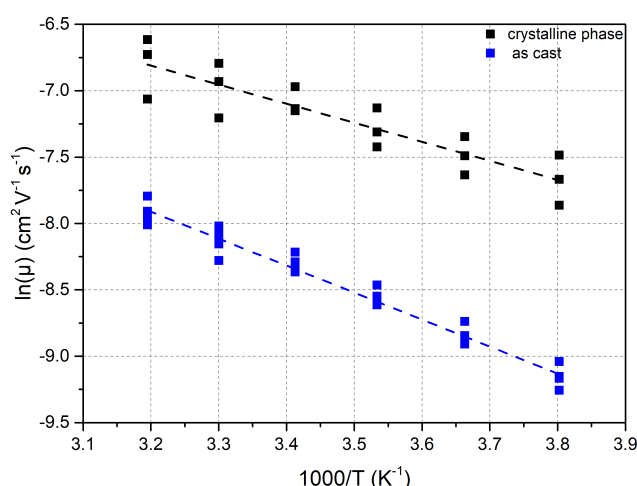
Figure 6-14: Variation of mobilities as a function of temperature, dash lines are the linear fitting curves.

The temperature dependence of the mobility is a key parameter to understand the energetics of charge carrier transport in organic semiconductors. As shown in Figure 6-14, the mobility follows an Arrhenius law (at least in the limited temperature range) with an activation energy E_a:

$$\mu = \mu_0 \cdot exp(-\frac{E_a}{kT}) \qquad (6\text{-}16)$$

where k is the Boltzmann constant, T is the temperature and μ_0 is a constant which represents the mobility at infinite temperature[111]. The exponential temperature dependence reveals that the charge transport is thermally activated.

The activation energy can be understood as the average energy needed for charge carrier hopping from one molecular site to a neighboring site[112,113]. The values of E_a in both states are shown in Table 6-7. For hopping-transport in organic semiconductors, the typical values of activation energies reported in literature vary between 0.1 eV and 1.1 eV[114–116]. The measured activation energy of as-deposited TPD_{C8}-TAT_{C8} film is about 180 meV which is comparable to literature data. A slightly lower activation energy is observed in the crystalline state, suggesting that the distribution of electronic states is reduced upon crystallization (see also Chapter 8 when discussing the thin-film morphology).

Table 6-7: Activation energy values and mobilities of TPD$_{C8}$-TAT$_{C8}$ films at as-deposited and crystalline states. Those values are based on 12 different transistors.

	as-deposited	crystalline state
μ_{hole}^{OFET} ($cm^2\,V^{-1}\,s^{-1}$)	$(2.8\pm1) \times 10^{-4}$	$(6.2\pm2) \times 10^{-3}$
E_a^{OFET} (meV)	176±10	116±10

6.2.2 SCLC mobilities

6.2.2.1 Standard structural devices

The same temperature dependent measurements have been conducted on SCLC devices using both, standard and sandwiched-type structures. The J-V characteristics of standard devices are shown in Figure 6-15. We note that the current increases with temperature at all applied voltages for both pristine and crystalized films, suggesting that the mobility increases with temperature. Interestingly, the effect is less pronounced in the crystalline state.

Figure 6-16 represents the mobility data in an Arrhenius plot. The mobility in as-deposited state increases by a factor of 2.8 when the temperature varies from -10°C to 40°C, while it only increases by 1.3 in the crystalline state. Correspondingly, the activation energies are significantly lower in the crystalline state.
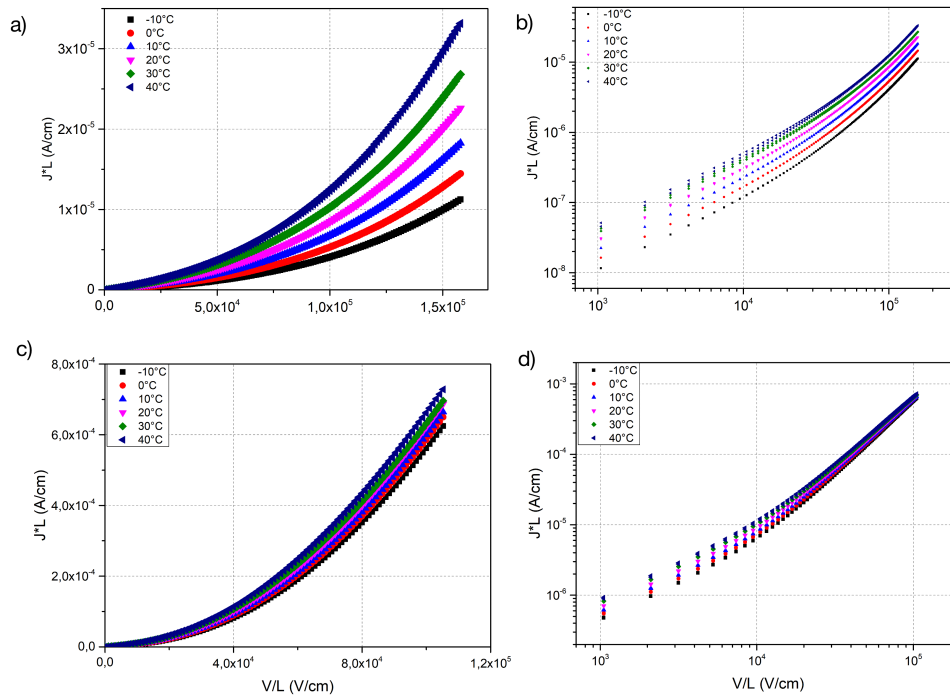
Figure 6-15: J-V characteristics as a function of temperature on standard SCLC devices of TPD$_{C8}$-TAT$_{C8}$ films at as-deposited state in (a) linear regime and (b) logarithm regime; and

at crystallization regime in (c) linear regime and (d) logarithm regime. The range of the varied temperature is from -10°C to 40°C.
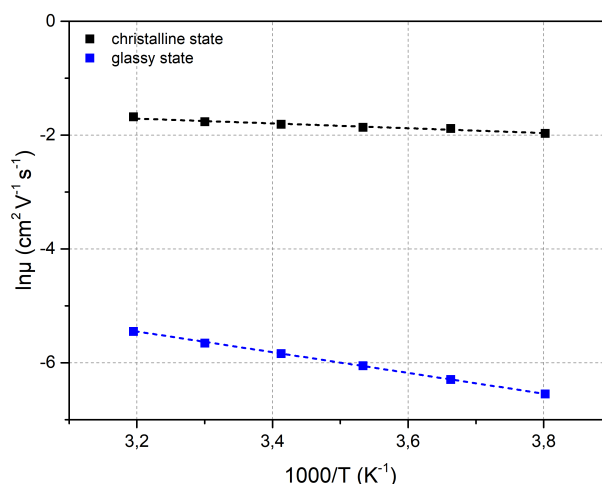
Figure 6-16: lnμ as a function of temperature for TPD$_{C8}$-TAT$_{C8}$ films at as-deposited state (blue dots) and crystalline state (black dots). Dash lines are the linear fit of each series of dots.

The activation energies are summarized in Table 6-8. The activation energy in the crystalline state (26 meV) is 7 times lower than in the as-deposited state. Such a substantial drop in E_a points out a high structural order. To fully understand the differences in the activation energy, further investigations of the film morphology are needed (see chapter 8).

Table 6-8: Activation energy of TPD$_{C8}$-TAT$_{C8}$ films at as-deposited state and crystalline state.

	as-deposited	**crystalline state**
E_a^{SCLC} (meV)	185±5	26±8
E_a^{OFET} (meV)	176±10	116±10

6.2.2.2 Sandwiched structural devices

Complementary temperature dependent SCLC measurements were done on the sandwiched device in the crystalline state. It should be mentioned that these measurements were performed 2 weeks after the device fabrication of the samples, possibly leading to device degradation. The room temperature mobility dropped indeed from 0.14 cm^2 V^{-1} s^{-1} down to 0.08 cm^2 V^{-1} s^{-1} during this period.

The J-V characteristics in linear and logarithm scales are shown in Figure 6-17. The increase of the current with temperature is significantly more pronounced

than for the standard SCLC device (Compare Figure 6-15c and d). The calculated mobilities at each temperature are shown in Figure 6-18 (black dots).
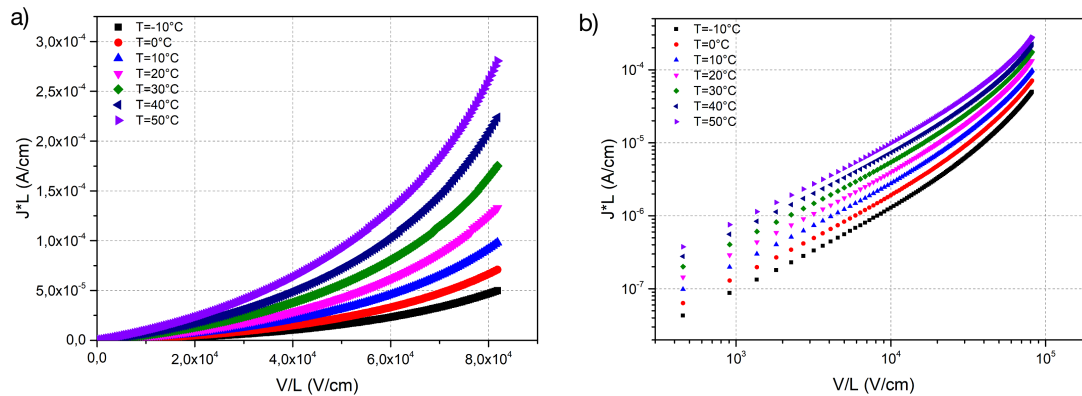
Figure 6-17: J-V characteristics as a function of temperature on sandwiched structural SCLC devices of TPD$_{C8}$-TAT$_{C8}$ films at crystalline state in (a) linear regime and (b) logarithm regime. The range of the varied temperature is from -10°C to 50°C.
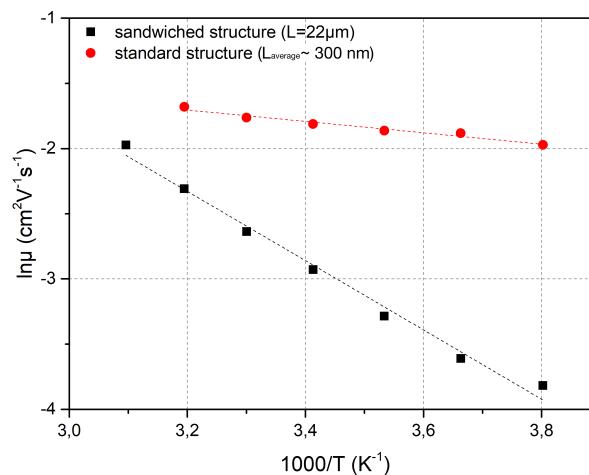
Figure 6-18: lnμ as a function of temperature for TPD$_{C8}$-TAT$_{C8}$ films at crystalline state for both spin-coated (red dots) and sandwiched structural devices (black dots). Dash lines are the linear fit of each series of dots.

The activation energy in the crystalline state are shown in Table 6-9. Surprisingly, for sandwiched structural SCLC diodes, E_a is around 220 meV, which is slightly higher than E_a at as-deposited state for standard SCLC diodes and OFETs (~ 180 meV). This value is also four times higher than E_a obtained on thin film devices (26 meV). The possible reason for this discrepancy may be due to the substantially larger thickness of the active layer in the sandwich device (~ 20 μm instead of~ 300 nm) and to the larger hopping barrier at the interface between molecular crystals (or "crystalline grain boundary"). In the thin film device, the film thickness is of the same order of magnitude than the height of

the molecular crystals. Therefore, the charges may flow from one electrode to the other by crossing only a small number of crystals (or eventually only a single crystal). On the other hand, the thickness of the sandwich device is orders of magnitude larger. Inter-grain charge carrier hopping may therefor become a current limiting factor and be responsible for the larger the activation energy.

Table 6-9: Activation energy for SCLC devices and OFETs at as-deposited and crystalline states.

	Activation energy E_a (meV)	
	as-deposited	crystalline state
sandwiched SCLC devices	--	220±8
standard SCLC devices	185±5	26±8
OFETs	176±10	116±10

6.2.3 Conclusion: temperature dependent charge transport

In conclusion, the temperature dependence of the J-V characteristics of TPD$_{C8}$-TAT$_{C8}$ organic semiconductor with different devices have been systematically investigated. We found that in both OFETs and SCLC diodes, the hole mobility follows an Arrhenius temperature dependence $\mu_h(T)=\mu_o exp(-E_a/kT)$ for all TPD-TAT derivatives.

Activation energies from OFET and SCLC measurements in the glassy state are close to 0.18 eV, which is comparable to a large variety of disordered organic semiconductors (for instance, E_a is around 0.3 eV for P$_3$HT and 0.45 eV for MEH-PPV[117,118]). Importantly, the activation energy is much reduced in the crystalline state for thin film devices and can be considered as representative of intra-grain charge transport. Similar results were also found by Christopher Proctor *et al.* who investigated the temperature dependence of the charge transport in three different molecular donors:PC$_{71}$BM blend systems[118]. These molecular donors have different structural ordering and they showed that long range order along the π-stacking direction leads to lower activation energy, and correspondingly, higher charge carrier mobilities.

The impact of the charge transport properties on the photovoltaic performances will be described in the next chapter.

CHAPTER 7
Results: Photovoltaic properties

In this chapter, photovoltaic properties of investigated TAT-based molecular donors will be tested in bulk heterojunction solar cells.

The fullerene derivative PC71BM is used as electron-acceptor for all TPD-TAT molecular donors because of its attractive properties including high electron affinity, high electron mobility in 3D, enhanced optical absorption (in comparison to $PC_{61}BM$), as well as the ability to form nanoscale morphologies in BHJ active layers that favor charge separation[15]. Throughout this thesis, 1,8-diiodooctane (DIO) is used as a processing additive to enhance the performance of the BHJ devices. DIO is expected to optimize the active layer morphology, forming a better bi-continuous interpenetrating network for exciton dissociation and charge carrier transport, and hence, increase the PCE of BHJ devices[119–121]. Device elaboration procedures and methods for electrical characterization have been presented in Chapter 4.

The first section of this chapter introduces procedure followed to reach the optimum conditions. The next part presents the photovoltaic properties of all TPD-TAT based BHJ devices. And at last, a conclusion will be given.

7.1 Optimum conditions

In order to achieve the optimum conditions for BHJ devices, device structure, D:A weight ratio, concentration of the solutions and quantity of the processing additive have been varied, along with different annealing conditions.

First series of measurements were conducted on TPD_{EH}-TAT_{C8} molecule by applying the standard device structure (ITO/PEDOT:PSS/active layer/Al). The weight ratio was varied while the concentration of the solution was kept constant. The OPV parameters corresponding to each condition are summarized in Table 7-1. For each condition 8 cells (2 samples) have been tested.

Table 7-1: Conditions for TPD_{EH}-TAT_{C8}:$PC_{71}BM$ blend, standard structure is employed for all the conditions and correspondent average OPV parameters.

Conditions	D:A[a]	Conc.[b] (mg/ml)	DIO[c] (%)	annealing[d]	device performances[e]			
					Voc (V)	Jsc (mA cm⁻²)	FF (%)	PCE (%)
1	1:1	5	0	no	0.76	4.7	39	1.2
2	1:1	5	0	80°C/10 min	074	4.9	42	1.7
3	1:1	5	0	100°C/10 min	0.51	4.0	34	0.7
4	1:2	5	0	no	0.73	5.5	37	1.5
5	1:2	5	0	80°C/10 min	0.73	5.8	39	1.6
6	1:2	5	0	100°C/10 min	0.49	4.8	34	0.8
7	1:3	5	0	no	0.72	3.6	29	0.8
8	1:3	5	0	80°C/10 min	0.74	3.4	32	1.0
9	1:3	5	0	100°C/10 min	0.45	3.5	32	0.5
10	1:4	5	0	no	0.67	2.6	33	0.5
11	1:4	5	0	80°C/10 min	0.70	2.7	33	0.6
12	1:4	5	0	100°C/10 min	0.66	2.5	32	0.4

[a]Donor:Acceptor weight ratio

[b]concentration of donor in final chloroform solution

[c]concentration of DIO additive

[d]annealing condition

[e]average device performances on 8 devices

From Table 7-1, we can observe that the photovoltaic performances at D:A weight ratio 1:1 and 1:2 are higher than the concentration 1:3 and 1:4 (compare conditions 1, 4, 7, 10). For the same weight ratio, the annealing at 80°C for 10 minutes enhances the photovoltaic performances while the annealing at 100°C decreases the efficiencies. The annealing process is conducted before the evaporation of top electrode.

BHJ devices with an inverted structure (ITO/PEIE/active layer/MoO_3/Ag) have also been elaborated with similar conditions for the active layer deposition. In this series of measurements, only the D:A weight ratio has been varied. And all samples have been annealed at 80°C for 10 mins before the deposition of top electrode.

Table 7-2: Conditions with varied D:A weight ratios for TPD_{EH}-TAT_{C8}:$PC_{71}BM$ blend with inverted structure and their correspondent OPV parameters.

Conditions	D:A	Conc. (mg/ml)	DIO (%)	annealing	device performances			
					Voc (V)	Jsc (mA cm^{-2})	FF (%)	PCE (%)
13	1:0.5	5	0	80°C 10 min	0.81	3.2	56.3	1.5
14	1:1	5	0	80°C 10 min	074	6.1	43	1.8
15	1:1.5	5	0	80°C 10 min	0.77	6.2	44	2.1
16	1:2	5	0	80°C 10 min	0.72	6.0	41	1.7

If we compare the standard and inverted structures in the same conditions (**condition 2** and **14** or **condition 5** and **16**), the V_{oc} are close but J_{sc} and FF are higher in the inverted device (J_{sc} is 25 % higher in **condition 14** than **condition 2**). The enhanced J_{sc} might originate from increased optical absorption, or reduced bimolecular recombination[122,123]. Consequence, PCE values are slightly higher with inverted structures.

By comparing the conditions in Table 7-2, we find out, that the optimum weight ratio corresponds to 1:1.5. Therefore, for further optimization, inverted structure with D:A weight ratio of 1:1.5 will be kept constant. However, the solution concentration will be altered, as well as the concertation of the processing additive. (see Table 7-3).

Table 7-3: Conditions with alternative concentrations of the solution for TPD$_{EH}$-TAT$_{C8}$:PC$_{71}$BM blend with inverted structure and their correspondent OPV parameters.

Conditions	D:A	Conc. (mg/ml)	DIO (%)	annealing	device performances			
					Voc (V)	Jsc (mA cm^{-2})	FF (%)	PCE (%)
17	1:1.5	5	0	80°C 10 min	0.77	6.2	44	2.1
18	1:1.5	5	0.3	80°C 10 min	077	6.7	48	2.6
19	1:1.5	6.5	0.3	80°C 10 min	0.73	5.4	48	2.1
20	1:1.5	7.5	0	80°C 10 min	0.75	4.3	42	2.0
21	1:1.5	7.5	0.3	80°C 10 min	0.77	5.3	47	2.2
22	1:1.5	7.5	0.4	80°C 10 min	0.75	5.5	48	2.5
23	1:1.5	7.5	0.5	80°C 10 min	0.77	4.6	56	2.5

Comparing the **condition 17** and **18,** or the **condition 20, 21, 22** and **23**, we find out that the presence of DIO increases the J$_{sc}$ and FF, and PCE accordingly. This might be due to optimized active layer morphology, which favors the exciton dissociation and charge carrier transport.

Condition 17, 19 and **21** are identical except for the solution concentration. The corresponding OPV performances suggest that at 5 mg/ml, V$_{oc}$ and Jsc are highest. When the concentration of the blend is varied, the active layer thickness changes. Although a thicker film could absorb more incident light, the device performance can be less efficient because of inadequate mobility for charges to be collected at electrodes.

In conclusion, for TPD$_{EH}$-TAT$_{C8}$:PC$_{71}$BM blend BHJ devices, the optimum condition to obtain the best OPV performances are: 1:1.5 weight ratio, 5 mg/ml on donor, 0.3 % DIO and annealing at 80°C for 10 minutes before electrode deposition (Table 7-3, marked in red).

A similar optimization process has been applied to TPD$_{C8}$-TAT$_{C8}$. An inverted structure was utilized and the corresponding conditions are summarized in Table 7-4.

Table 7-4: Conditions for TPD$_{C8}$-TAT$_{C8}$:PC$_{71}$BM blend with inverted structure and their correspondent OPV parameters.

Conditions	D:A	Conc. (mg/ml)	DIO (%)	annealing	device performances			
					Voc (V)	Jsc (mA cm^{-2})	FF (%)	PCE (%)
24	1:1	5	0.3	80°C 10 min	0.77	6.3	52	2.6
25	1:1	7.5	0.3	80°C 10 min	0.81	6.0	54	2.6
26	1:1.5	5	0.2	80°C 10 min	0.73	8.3	45	2.8
27	1:1.5	5	0.3	80°C 10 min	0.80	8.0	58	3.7
28	1:1.5	7.5	0.3	80°C 10 min	0.78	7.9	46	2.8
29	1:1.5	7.5	0.4	80°C 10 min	0.78	8.2	55	3.5
30	1:1.5	7.5	0.5	80°C 10 min	0.78	7.1	44	2.5

By comparing the **conditions 24** and **27** (or **condition 25** and **28**), it is clear that when BHJ active layer has the D:A weight ratio of 1:1.5, J$_{sc}$ is 25 % higher than the one with 1:1. The same tendency then for TPD$_{EH}$-TAT$_{C8}$:PC$_{71}$BM was found when varying the solution concentration. On the other hand, while adding DIO leads to a higher J$_{sc}$ and FF, high DIO concentrations (0.5 %) cause the opposite evolution. At last, active layer with 1:1.5 D:A weight ratio, 5 mg/ml solution concentration with 0.3 % DIO shows the best OPV performances (Table 7-4, marked in red).

A similar optimization process has been performed on the other two molecular donors with branched side-chains on TAT, and the respective optimum conditions for each molecule are as follow:

Table 7-5: Optimum conditions for each molecule and corresponding average photovoltaic parameters.

Molecule	D:A	Conc. (mg/ml)	DIO (%)	annealing	device performances			
					Voc (V)	Jsc (mA cm^{-2})	FF (%)	PCE (%)
TPD$_{C8}$-TAT$_{C8}$	1:1.5	5	0.3	80°C 10 min	0.78	8.2	57	3.7
TPD$_{EH}$-TAT$_{C8}$	1:1.5	5	0.3	80°C 10 min	0.78	6.5	48	2.4
TPD$_{C8}$-TAT$_{EH}$	1:1.5	7.5	0.4	80°C 10 min	0.83	4.3	40	1.4
TPD$_{EH}$-TAT$_{EH}$	1:1.5	7.5	0.4	80°C 10 min	0.81	2.0	36	0.6

7.2 Photovoltaic performances

J-V characteristics of TPD-TAT based BHJ devices under optimum conditions are shown in Figure 7-1, and average photovoltaic results along with the maximum PCE values are summarized in Table 7-6.

Table 7-6: Average OPV parameters and maximum PCE values of TPD-TAT:PC$_{71}$BM based BHJ devices under optimized conditions.

Molecule	Voc (V)	Jsc (mA cm-2)	FF (%)	PCE (%)	PCE$_{max}$ (%)
TPD$_{C8}$-TAT$_{C8}$	0.78±0.01	8.2±0.4	57±4	3.7±0.5	4.1
TPD$_{EH}$-TAT$_{C8}$	0.78±0.01	6.5±0.2	48±3	2.4±0.2	2.6
TPD$_{C8}$-TAT$_{EH}$	0.83±0.01	4.3±0.1	40±1	1.4±0.1	1.5
TPD$_{EH}$-TAT$_{EH}$	0.81±0.01	2.0±0.01	36±1	0.60±0.05	0.6
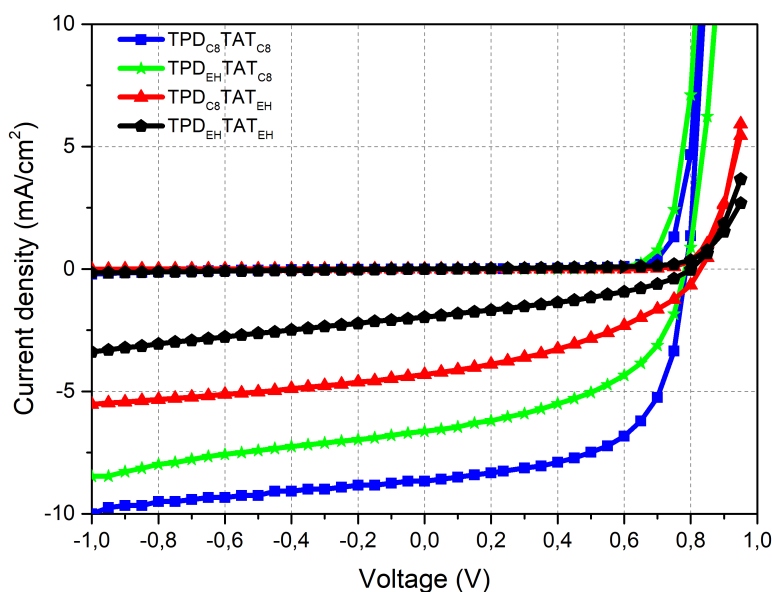
Figure 7-1: J-V characteristics of BHJ solar cells based on TPD-TAT:PC$_{71}$BM in the dark and under standard AM1.5G (100 mW/cm²) illumination conditions.

The photovoltaic results are in-line with the molecular properties and charge carrier transport measurements. It appears that the nature of the peripheral chains does not impact significantly the PC71BM load for which the exciton dissociation efficiency and charge collection are optimized. The V$_{oc}$ values are close to those expected from the HOMO and LUMO levels, which is around 0.8 V (e·Voc = |HOMO$_D$-LUMO$_A$|-0,3)[72].

The other photovoltaic parameters are all found to vary substantially from one molecule to the other. The J$_{sc}$ increases continuously from the less-ordered

TPD$_{EH}$-TAT$_{EH}$ molecule (2.0 mA cm^{-2}) to the most ordered TPD$_{C8}$-TAT$_{C8}$ (8.6 mA cm^{-2}).

Importantly, the FF increases from 36 % for TPD$_{EH}$-TAT$_{EH}$ to near 60% from TPD$_{C8}$-TAT$_{C8}$ to TPD$_{C8}$-TAT$_{C8}$. The FF can be affected by the series and parallel resistance (R$_s$ and R$_{sh}$) of the solar cells, as well as the recombination in the cells. In other words, charge carrier transport is crucial for the FF since efficient transport leads to efficient charge extraction and less recombination. According to the charge transport measurements presented in Chapter 6, the molecules bearing linear side chains on the TAT units (i.e. TPD$_{EH}$-TAT$_{C8}$ and TPD$_{C8}$-TAT$_{C8}$), the in-plane and out-of-plane hole mobilities are significantly higher than for the TPD$_{C8}$-TAT$_{EH}$ and TPD$_{EH}$-TAT$_{EH}$ in as-deposited glassy state (10^{-3} *versus* 10^{-5} cm^2 V^{-1} s^{-1}). The photovoltaic performances are therefore in good agreement with our transport measurements.

Consequently, the maximum PCE value of around 4% has been obtained for the most structurally organized molecule TPD$_{C8}$-TAT$_{C8}$. Considering the high optical band gap of the molecules (~ 2.0 eV), the PCE values of 4.1 % of TPD$_{C8}$-TAT$_{C8}$ appears as a quite fair performance when compared to the benchmark P$_3$HT of similar band gap, whose PCE is typically around 3 – 4 %[124].

One should note that there are still possibilities to improve the photovoltaic performance. As presented in Chapter 2, the efficiency is defined as $PCE = \frac{V_{oc} \cdot I_{sc} \cdot FF}{P_{in}}$, therefore, PCE can be improved by increasing the V$_{oc}$, I$_{sc}$ and FF.

Even though the upper limit of V$_{oc}$ is determined by the HOMO/LOMO energy levels, charge carrier recombination in the bulk and at the interfaces can lead to voltage losses in V$_{oc}$. Therefore, further engineering of the interfacial layers may lead to larger V$_{oc}$ values.

Alternative methods to improve the film morphology may also be considered. For instance, for other small donor:PCBM systems, solvent vapor annealing (SVA) has been found to improve the device performances. Jones *et al.* demonstrated that by exposing the DPP(TBFu)$_2$:PC$_{71}$BM to different solvent vapors, including THF, CS$_2$, chlorobenzene (CB), 1,2-dichlorobenzene (oDCB),

chloroform, acetone and 1,2-dichloroethane (DCE), the efficiencies were found out enhanced for all solvents, and best photovoltaic performance was achieved by using THF and CS_2, with a ten-fold increase in the PCE (up to 5.2 %)[76]. They conclude that solvents with high vapor pressure and medium donor solubility were found to enhance the solar cell efficiency, while acceptor solubility in these solvents played an insignificant role in determining the photovoltaic performance. The SVA was shown to induce a desirable phase separation in both lateral and vertical directions. The SVA also lead to organized fiber-like structure which enhances the hole mobility.

Another study reported by Pavan Kumar *et al.* combined the thermal annealing with the solvent vapor annealing[78,125]. The as-deposited blended film was heated on the hot plate first, increasing the PCE from 3.5 % to 4.6 %. After cooling to room temperature, the film was placed in a Petri dish containing THF vapor for 2 minutes, and the PCE further increases to 5.5 %.

Using additive is another commonly use method to improve the morphology. In the previous study, the introducing of DIO in solutions results in an improved OPV performance.

7.3 Conclusion

To conclude, the fine molecular design of dumbbell-shaped molecules constitutes a promising route towards efficient solution-processable donor molecules for high performance BHJ photovoltaic devices. In particular, since TPD-TAT molecules have a large bandgap (~ 2 eV), they are promising materials for tandem solar cells[126]. In a tandem solar cell, donors with differentiated energy bandgaps should be applied in order to absorb in different solar spectrum range. For TPD-TAT molecules, the absorption ranges from 300 nm to 550 nm (presented in Chapter 5), so materials with absorption over 550 nm can be used as second electron donor (detailed design rules can be seen in reference[127]). For example, thienyl-Bodipy dye TB2 whose chemical structure is shown in Figure 7-2[128] could be an interesting candidate. This molecule has a

bandgap of 1.45 eV with broad absorption range from 350 to 920 nm. PCE of 4.7 % in BHJ solar cells has been obtained in blend with PC71BM.
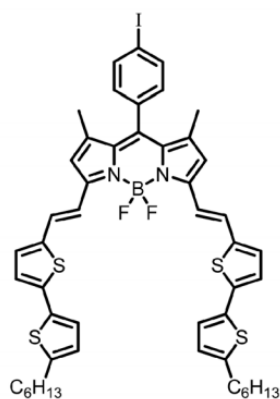
TB2

Figure 7-2: Chemical structure of TB2.

CHAPTER 8
Results: Thin-film morphology

Morphology and microstructure of thin films is a critical and unpredictable parameter, and directly controls their optoelectronic properties, which are often different from bulk material properties. In the previous chapters, SAXS measurements on bulk materials revealed that the stacking of TAT units drives the molecular self-assembling: linear side-chains on them lead to nematic columnar organizations while the branched ones lead to amorphous states. This observation is further confirmed by photovoltaic devices, since the most structurally ordered molecule obtains highest PCE. In addition, good charge transport properties have been provided by the lateral π-stacking platforms of TAT units. On the other hand, charge carrier transport measurements of TPD-TAT$_{C8}$ thin films show anisotropic mobilities in the directions perpendicular and parallel to the substrate-plane. In the crystalline state, a high out-of-plane mobility of 10^{-1} cm^2 V^{-1} s^{-1} has been obtained for TPD$_{C8}$-TAT$_{C8}$ molecule, while the in-plane mobility is two orders of magnitude lower. This large difference can be related to the thin film morphologies of different devices.

In order to understand the influence of the side-chains on the self-organization of thin films, as well as the impact of the morphologies on optoelectronic properties, grazing incidence wide angle X-ray scattering (GIWAXS) was used to characterize crystalline lattice spacing and correlation length, as well as the molecular orientation. Atomic force microscopy (AFM) measurements were moreover performed to characterize the film surface topography.

The first section introduces the GIWAXS measurements of TPD-TAT:fullerene blend films, similar to the OPV active layers. The pure TPD_{C8}-TAT_{C8} films at different states are also characterized. The films deposition conditions and measurement procedures were presented in Chapter 4. The last section shows the AFM surface topographies of the active layers of measured BHJ devices, OFETs and SCLC diodes in Chapter 6 and 7.

8.1 GIWAXS measurements

First, thin films elaborated with the same conditions as the active layers of photovoltaic devices have been characterized. Then, detailed investigations of TPD_{C8}-TAT_{C8}:$PC_{71}BM$ blend films with various weight ratios have been conducted in order to figure out the influence of $PC_{71}BM$ on the TPD_{C8}-TAT_{C8} microstructure. In the third and last section, TPD_{C8}-TAT_{C8} thin films on top of either PEDOT:PSS/Si and HMDS/SiO2/Si have been tested, which are comparable to the structure used for SCLC and OFET devices presented in Chapter 6.

8.1.1 TPD-TAT:PC_{71}BM blend films

For the GIWAXS measurements, TPD-TAT:PC_{71}BM films have been spin-coated on top of PEIE with Silicon wafer as substrates, with a weight ratio of 1:1.5. In addition, 0.3 % DIO was used as processing addictive. The samples were annealed at 80°C for 10 minutes after the deposition. The GIWAXS patterns of blend films are shown in Figure 8-1.
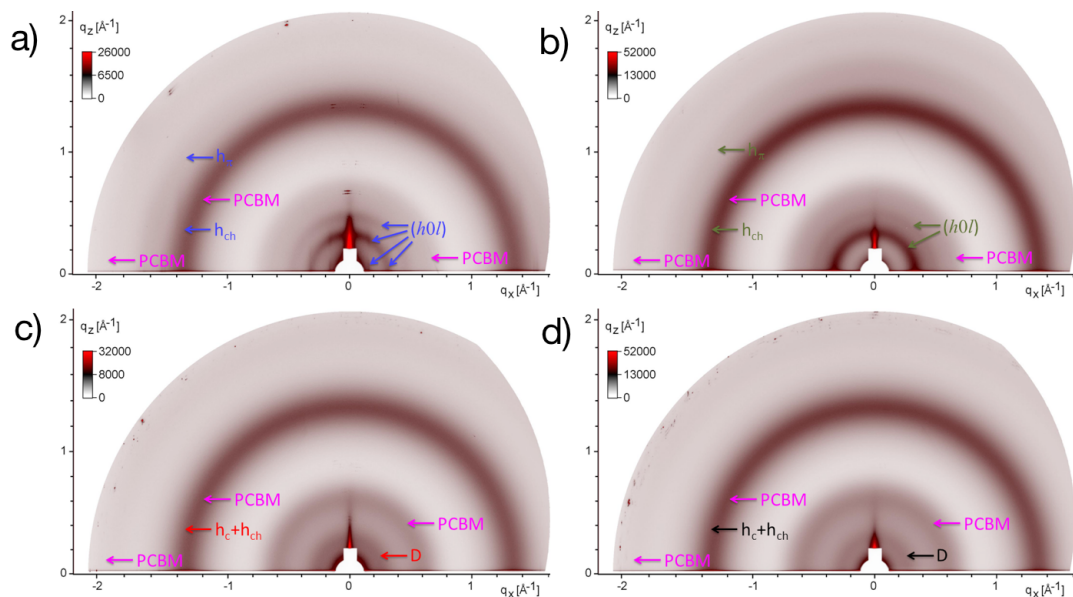
Figure 8-1: GIWAXS patterns of blended and annealed films of (a) TPD_{C8}-TAT_{C8}, (b) TPD_{EH}-TAT_{C8}, (c) TPD_{C8}-TAT_{EH} and (d) TPD_{EH}-TAT_{EH}, in 1:1.5 mixture with $PC_{71}BM$.

All patterns contain signals from at least two coexisting PCBM-rich and donor molecule-rich phases. For the TPD_{C8}-TAT_{C8} and TPD_{EH}-TAT_{C8} films, the small-angle reflections (*hol*) indicate a two-dimensional lattice formed by the arrangement of column-like objects, while the wide-angle scattering peak (h_π) is the signature of the π- stacking of flat conjugated cycles into columns. On the other hand, the amorphous molecules, TPD_{C8}-TAT_{EH} and TPD_{EH}-$TAT_{EH,}$ give rise, as expected, to only a weak and diffuse small-angle ring, revealing a local-range nano-segregation.

If we compare the SAXS patterns obtained for pure materials at room temperature in the glassy state (Figure 8-2a) and $PC_{71}BM$ (Figure 8-2b), with the radial profiles of GIWAXS patterns (Figure 8-2c), we can observe that the contribution of the PCBM-rich phase dominates the profiles and that the scattering maxima are not significantly shifted. The main peak around 0.3 $Å^{-1}$ observed on TPD_{C8}-TAT_{C8} and TPD_{EH}-TAT_{C8} thin films is close to D_{col}, while the h_π scattering signals coincide as well. Interestingly, the high order reflections visible in the profiles (~0,4 and ~0,7 $Å^{-1}$) are most pronounced for TPD_{C8}-TAT_{C8}, indicating the development of a more regular columnar structure.

In conclusion, for BHJ solar cells, the presence of $PC_{71}BM$ does not change significantly the molecular packing of the donor molecules. For TPD-

TAT_{C8}:$PC_{71}BM$ active layer, the columnar structures subsist, explaining that the charge carrier transport remains efficient, leading to high FF and J_{sc} values. On the other hand, TPD-TAT_{EH} molecules are amorphous, thus the charge transport is less efficient and so are the photovoltaic performances.
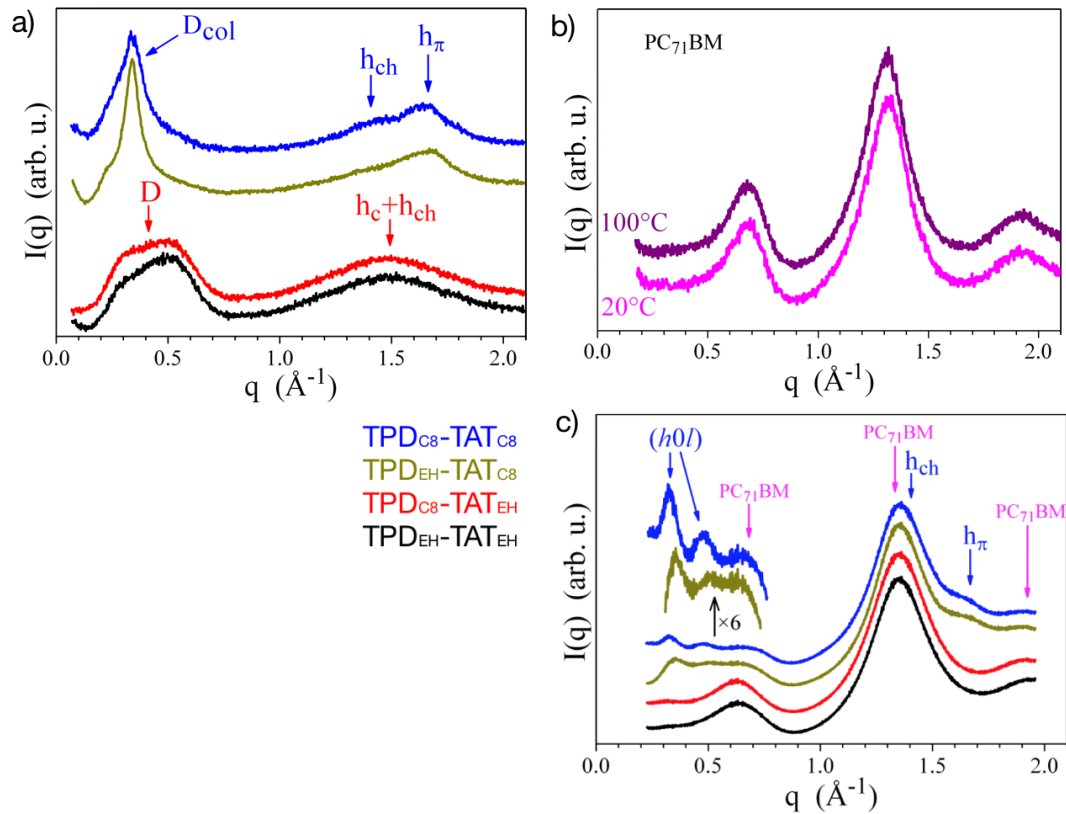
Figure 8-2: SAXS patterns of (a) pure TPD-TAT molecules at glassy state and (b) $PC_{71}BM$ at 20°C and 100°C; (c) radial profiles of GIWAXS patterns of TPD-TAT:$PC_{71}BM$ blend films.

8.1.2 TPD$_{C8}$-TAT$_{C8}$:PC$_{71}$BM blend films with various weight ratios

To further explore the influence of $PC_{71}BM$ quantity on the TPD_{C8}-TAT_{C8} microstructure, blend films with various weight ratios (1:0.1, 1:0.5, 1:1 and 1:1.5) have been characterized. The blend films were deposited on top of PEDOT:PSS/Si substrates. Both pristine and annealed (80°C for 10 minutes) films have been prepared for each weight ratio.

First of all, GIWAXS patterns of a PEDOT:PSS film and its radial profile are shown in Figure 8-3 as a reference. Figure 8-4 presents the GIWAXS patterns of TPD_{C8}-TAT_{C8}:$PC_{71}BM$ thin films with different weight ratios (indicated on the

Figure). Figure 8-5 shows the radial profiles of TPD_{C8}-TAT_{C8}:$PC_{71}BM$ thin films with different weight ratios (curves presented with different colors), either before (Figure 8-5a) or after the annealing (Figure 8-5b). The SAXS patterns of bulk TPD_{C8}-TAT_{C8} pure materials are also included for comparison (Figure 8-5c).

As we can see, the contribution of the bottom PEDOT-PSS layer is undetectable, due to its comparatively low thickness. Comparing the three as cast films with 1:0.1, 1:0.5 and 1:1 weight ratios, the GIWAXS patterns show roughly the same distribution of domain orientations, whatever the PCBM content.

In consistency with previous results, the morphology of TPD_{C8}-TAT_{C8}:$PC_{71}BM$ thin films comply with the columnar-type self-organization of TPD_{C8}-TAT_{C8} pure material, as revealed by the presence of the scattering maximums h_{ch} and h_{π} and of the periodicity D_{col}, where h_{ch} represents the lateral distances between molten chains, h_{π}, the face-to-face distances between π-stacked segments, and D_{col}, the lateral spacing of TAT columns in the mixed periphery of alkyl chains and bridges. The D_{col} peak has a broad shape and is not associated to higher-order periodicities, as typical for nematic mesophases. Eventually, the peak position and width (D_{col} = 17-18 Å; correlation length from Scherrer formula: ξ ~ 4-8 nm) is roughly the same as in the bulk (D_{col} = 18-18.5 Å; ξ ~ 5-10 nm).

TPD_{C8}-TAT_{C8} in the pristine bulk state and in two thin films shows a further small-angle peak corresponding to two-columns periodicity (33-34 Å). This peak evidences the formation of a multiple-columns lattice, presumably through a self-aggregation process between conjugated bridges in the periphery of columns. On the contrary, only the broad D_{col} peak persists in the nematic phase and in most thin film profiles, for which the molecular organization therefore comes down to an arrangement of individual TAT columns. In any case, bridges introduce constraints hindering the regular spacing of columns and the development of a long-range columnar lattice, which conversely explains the freezing of the nematic bulk state and the finding that correlation lengths are not improved in the annealed thin films.
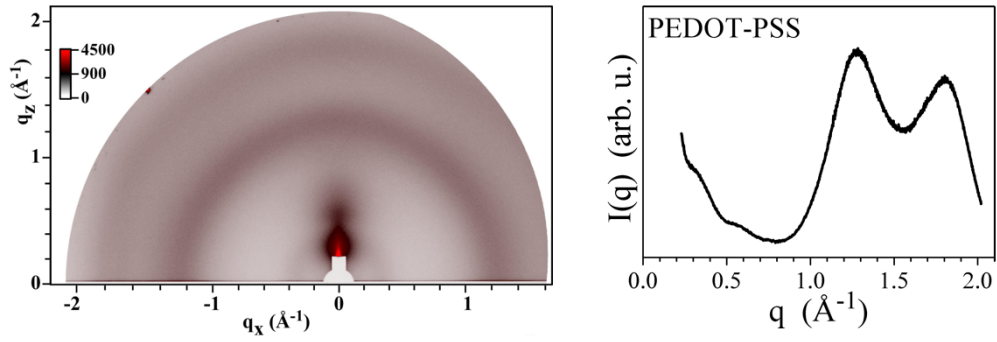
Figure 8-3: GIWAXS pattern of PEDOT:PSS film (left) and its radial profile (right).

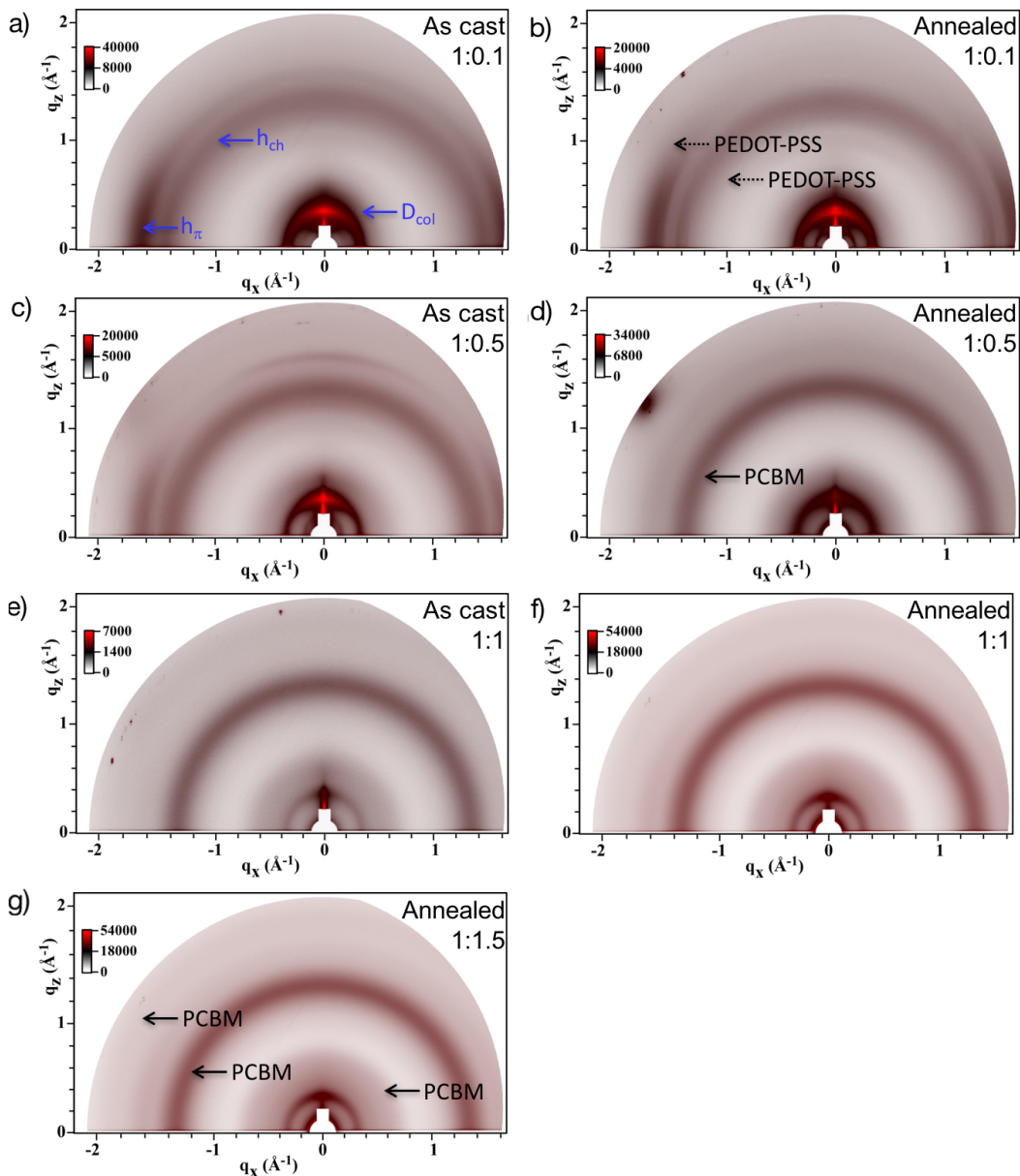

Figure 8-4: GIWAXS patterns of TPD_{C8}-TAT_{C8}: $PC_{71}BM$ blend films with weight ratio (a) 1:0.1 (as cast), (b) 1:0.1 (annealed), (c) 1:0.5 (as cast), (d) 1:0,5 (annealed), (e) 1:1 (as cast), (f) 1:1 (annealed) and (g) 1:1.5 (annealed).
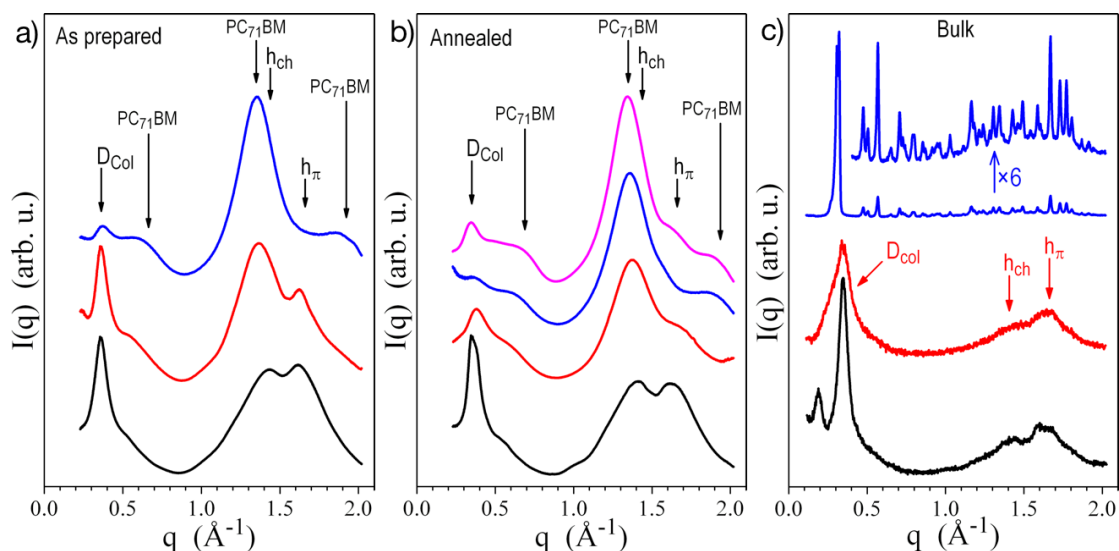
Figure 8-5: Radial profiles of precedent GIXS patterns of as prepared (left) and annealed (at 80°C, middle) films of TPD_{C8}-TAT_{C8}:$PC_{71}BM$ blends in following proportions, from bottom to top: 1:01 (black), 1:0.5 (red), 1:1 (blue), 1:1.5 (magenta). Profiles are compared with SAXS patterns of bulk TPD_{C8}-TAT_{C8} (right), in the pristine state (bottom, black), in the frozen room-temperature nematic phase (middle, red) and in the crystalline phase (top, blue).

8.1.3 PEDOT:PSS/TPD_{C8}-TAT_{C8} films

As shown in Chapter 6, a particularly high out-of-plane hole mobility has been measured in TPD_{C8}-TAT_{C8} thin films in the crystalline phase ($\sim$0.13 cm^2 V^{-1} s^{-1}). To better understand the origin of this efficient charge carrier transport, GIWAXS measurements have been performed on TPD_{C8}-TAT_{C8} films, both in the glassy and crystalline states. The films were deposited on the same substrate as for SCLC devices (PEDOT:PSS/ TPD_{C8}-TAT_{C8} film).

Figure 8-6 presents the GIWAXS patterns of PEDOT:PSS/TPD_{C8}-TAT_{C8} films in the glassy state (a) and in the crystalline state (b), as well as the corresponding radial profiles. SAXS patterns of bulk TPD_{C8}-TAT_{C8} in the crystalline phase is also presented for comparison

For TPD_{C8}-TAT_{C8} films in the glassy state (as cast film), a series of (00l) spots extending to l=5 emerged along the meridian (marked with blue arrow in Figure 8-6a, revealing the formation of ordered lamellae lying flat on the surface. The lamellar thickness (d = 35 Å) accords with two rows of flat-lying TAT columns, i.e. with the entire molecules periodicity. Apart from the lamellar peaks and from the broad scattering ring h_{ch} around 4.5 Å due to lateral distances between

molten chains, the pattern further contains two nearly sharp equatorial ($hk0$) bows (at 4.92 and 4.12 Å), originating from the in-plane arrangement of conjugated moieties. Crossed reflections (hkl) are totally absent, so that the morphology comes down to a superposition of molecular layers without positional correlations between molecules from successive layers. This "as cast" structure has no counterpart in the bulk TPD_{C8}-TAT_{C8} material, as it is induced by the specific flat thin film geometry during deposition step and finally erased by the subsequent annealing steps. It is worth mentioning that this morphology with lamellae parallel to substrate is not favorable for charge transport, which is different from results of edge-on lamellae.

On the other hand, for TPD_{C8}-TAT_{C8} films in the crystalline state (Figure 8-6b), the radial profile obtained from the narrow diffraction peaks is in agreement with the SAXS pattern in the crystalline phase of bulk TPD_{C8}-TAT_{C8}, notwithstanding the lower resolution of the former technique and the absence of 2D information for the latter. The crystal structure is thus the same or very close to the bulk. The diffraction peaks elongated into bows moreover show that crystals grew with preferential orientation with respect to substrate.

The molecular organization in the crystalline phase was found to contribute to the efficient charge carrier transport. Specifically, the SCLC hole mobility in crystalline phase is over 50 times higher than the mobility in as-cast glassy state (from 2.3×10^{-3} to $0.13 \ cm^2 \, V^{-1} \, s^{-1}$).
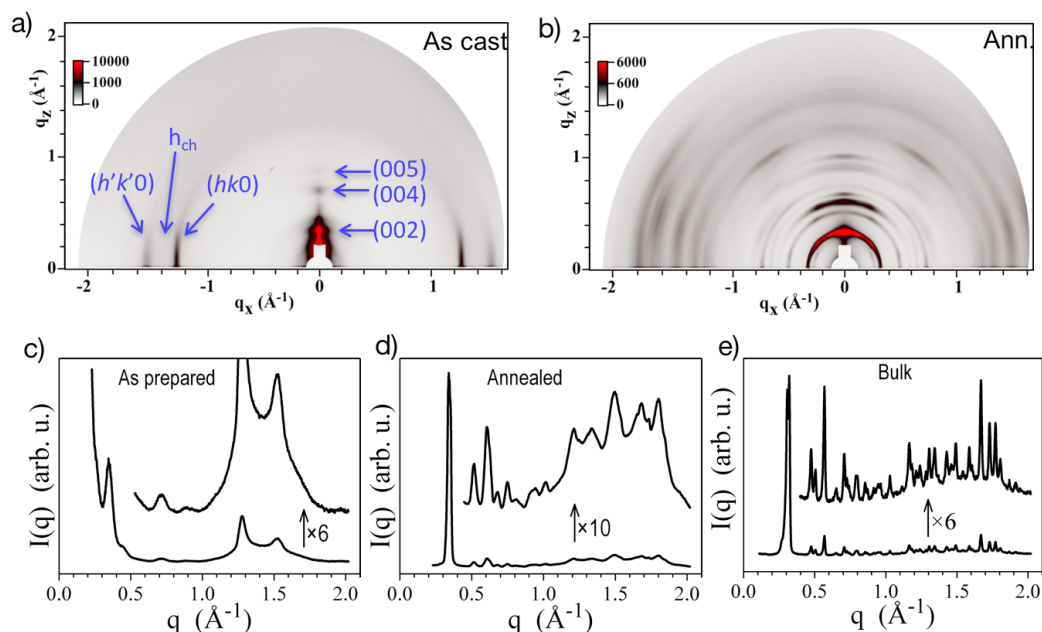
Figure 8-6: GIWAXS pattern of PEDOT:PSS/TPD$_{C8}$-TAT$_{C8}$ films: (a) as prepared and (b) annealed at 140°C in crystalline state; radial profiles correspond to pattern (a) and (b), and (e) SAXS pattern of bulk TPD$_{C8}$-TAT$_{C8}$ material in the crystalline phase.

8.1.4 HMDS/TPD$_{C8}$-TAT$_{C8}$ films

The same measurements have been performed for TPD$_{C8}$-TAT$_{C8}$ films in OFETs. Unlike in SCLC devices, the TPD$_{C8}$-TAT$_{C8}$ films in OFETs are deposited on top of HMDS, and the thickness is much lower (~30 nm for OFETs and ~120 nm for SCLC devices). The GIWAXS patterns in glassy and crystalline state are shown in Figure 8-7 (a) and (b) and the corresponding radial profiles are shown in (c) and (d). SAXS pattern of bulk TPD$_{C8}$-TAT$_{C8}$ in crystalline phase is also presented in (e).

The morphology of the as-prepared TPD$_{C8}$-TAT$_{C8}$ films agrees with the domain structure described above for the blends and for the frozen mesomorphous room-temperature bulk states. Patterns are composed of the scattering maximums h_{ch} and h_π. h_{ch} represents lateral distances between molten chains and h_π stands for face-to-face stacking into columns. In addition, D_{col} is the short range periodicity from the spacing of TAT columns (D_{col} = 17.5 Å; ξ ~ 7 nm). The preferential alignment is also still the same as before: TAT columns are lying flat on the surface (in-plane columns).

The X-ray structure obtained after crystallization at 135°C is identical to the one of the films directly deposited on PEDOT:PSS and thus the same as for bulk TPD_{C8}-TAT_{C8}. The crystalline orientation with respect to substrate is also the same as in the absence of HMDS, with however considerably improved alignment resulting in spot-like diffraction peaks.

The GIWAXS measurements are in line with the charge carrier transport measurements represented in Chapter 6, that TPD-TAT_{C8} materials exhibit columnar and crystalline organizations, which facilitate the intermolecular interactions. On the other hand, TPD-TAT_{EH} are amorphous materials, lead to less efficient charge transport and bad OPV performance.
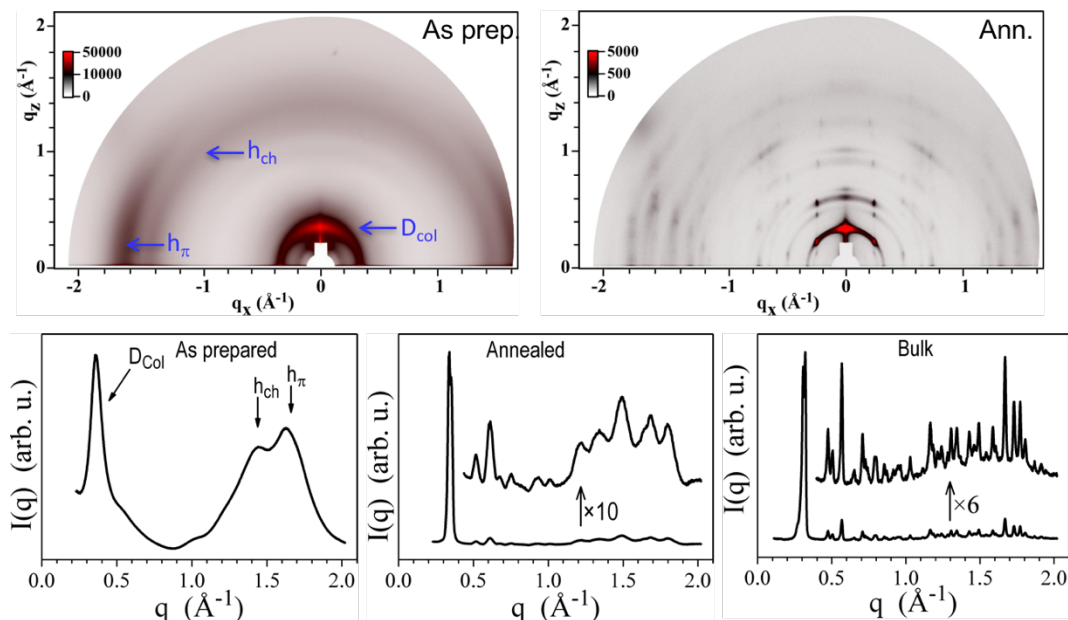

Figure 8-7: GIWAXS patterns of TPD_{C8}-TAT_{C8} films in (a) glassy and (b) crystalline state. Correspondent radial profiles are shown in (c) glassy and (d) crystalline state. (e) SAXS pattern of bulk TPD_{C8}-TAT_{C8} in the crystalline phase.

8.2 AFM measurements

Thin film topographies have been further analyzed by atomic force microscopy (AFM) technique to characterize the film quality, phase separation and crystallinity. TPD-TAT:PC$_{71}$BM blend films were deposited following the same procedure than for BHJ devices. TPD$_{C8}$-TAT$_{C8}$ thin films in crystalline state were also characterized, with two different substrates: PEDOT:PSS or HMDS/SiO2. These structures correspond to SCLC diodes and OFETs, respectively.

8.2.1 TPD-TAT:PC$_{71}$BM blend films

The AFM images of TPD-TAT:PC$_{71}$BM blend films are shown in Figure 8-8. The TPD$_{C8}$-TAT$_{C8}$:PC71BM film topography (image a) reveals the presence of homogenously distributed nanometer-sized "domains" that may correspond to TPD$_{C8}$-TAT$_{C8}$ rich and PC$_{71}$BM rich domains respectively. TPD$_{EH}$-TAT$_{C8}$:PC$_{71}$BM is somewhat less homogenous than TPD$_{C8}$-TAT$_{C8}$:PC$_{71}$BM and reveals the presence of spherical features that may correspond to larger PCBM aggregates. Similar, but more pronounced features can be seen in the TPD$_{EH}$-TAT$_{EH}$:PC$_{71}$BM, while the TPD$_{C8}$-TAT$_{EH}$:PC$_{71}$BM film appears featureless.

Although these results do not allow any conclusion about the composition of the different domains, they at least allow us to conclude that there is no macroscopic phase separation between the fullerene and the TPD-TAT molecules. Such a morphology is a prerequisite to achieve efficient charge generation.
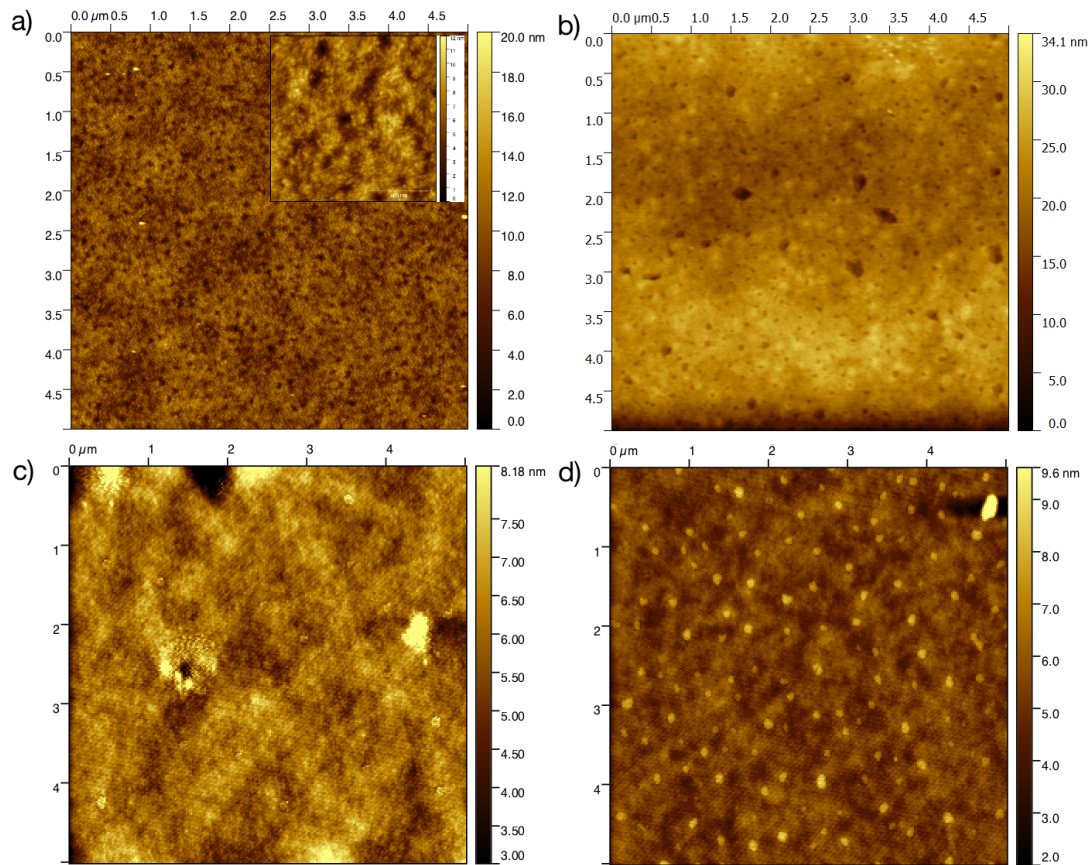
Figure 8-8: AFM topography images of (a) TPD_{C8}-TAT_{C8}:$PC_{71}BM$ (inset is the zoomed image), b) TPD_{EH}-TAT_{C8}:$PC_{71}BM$, c) TPD_{C8}-TAT_{EH}:$PC_{71}BM$ and d) TPD_{EH}-TAT_{EH}:$PC_{71}BM$ films. D:A ratio is 1:1.5 for all the films.

8.2.2 Pedot:PSS/TPD-TAT_{C8} films

In Chapter 6, charge carrier transport properties of TPD_{C8}-TAT_{C8} and TPD_{EH}-TAT_{C8} films have been measured by OFETs and SCLC devices. The SCLC mobility of crystalline TPD_{C8}-TAT_{C8} films is about 0.13 $cm^2\,V^{-1}\,s^{-1}$, which is two orders of magnitude higher than as-deposited ones. One the other hand, the mobility in the nematic phase is close to the as-deposited mobility ($\sim 10^{-3}\ cm^2\,V^{-1}\,s^{-1}$). However, unlike the evolution tendency of TPD_{C8}-TAT_{C8} mobilities, the SCLC mobility of crystalline TPD_{EH}-TAT_{C8} films is close to as deposited ones ($1.8\times 10^{-3}\ cm^2\,V^{-1}\,s^{-1}$), and the mobility in the nematic phase cannot be measured due to dewetted films. These carrier mobilities might be influenced by the film morphologies, therefore, AFM measurements have been conducted.

The AFM images for PEDOT:PSS/TPD_{C8}-TAT_{C8} films in different phases are shown in Figure 8-9. Image (a) and (b) shows the AFM images of TPD_{C8}-TAT_{C8}

films in crystalline state with different scanning scale (a: 10 μm and b: 20 μm). In figure a) and b), randomly distributed needle-like crystals can be observed, with length in the order of micrometers.

The crystals are gathered together leading to a very rough surface (roughness in the order of hundreds of nm). As shown in Chapter 6, this roughness is substantially higher than the value measured by the profilometer. This is probably due to the fact that the size of probing needle is larger than the average distance between the crystalline needles. As a consequence, the film average thickness estimated by the profilometer was wrong. This brought us to introduce the "statistical" model, described in chapter 6, to get an estimate of the mobility by taking into account the film roughness.

The presence of these crystals favors the out-of-plane charge transport, leading to a very high SCLC mobility in crystalline state. However, when we further annealed the same TPD$_{C8}$-TAT$_{C8}$ film above the isotropic phase transition temperature (180°C for 5 seconds), the mobility decreases. The AFM topography shows that, after this annealing step, the needle-like crystals disappeared, leading to a rather homogeneous film, as expected (Figure 8-9c). The "holes" that can be observed in Figure 8-9c are likely to be due to partial dewetting of the film. Indeed, the processing window that is required to avoid dewetting on a macroscopic range (i.e. visible by eye), turned out to be very narrow. The feature-less morphology is in-line with the low hole mobility (2×10^{-3} cm^{-2}V^{-1}s^{-1}) that was observed on similarly treated thin films.

To find out if the crystallization can be repeated after having reached the nematic state, the annealing process for cold crystallization has been applied to the same TPD$_{C8}$-TAT$_{C8}$ film. It turns out that the crystalline phase could be obtained again by annealing again the same sample. AFM image is shown in Figure 8-9d. The overall morphology, i.e. random assembly of needle-like crystals, was similar to those observed in the films after the first cold-crystallization step, but finer and more flexible (compare Figure 8-9 a and d). Also, the hole mobility measured on this film ($\sim 9 \times 10^{-2}$ cm^{2}V^{-1}s^{-1}) was similar to the previous results.
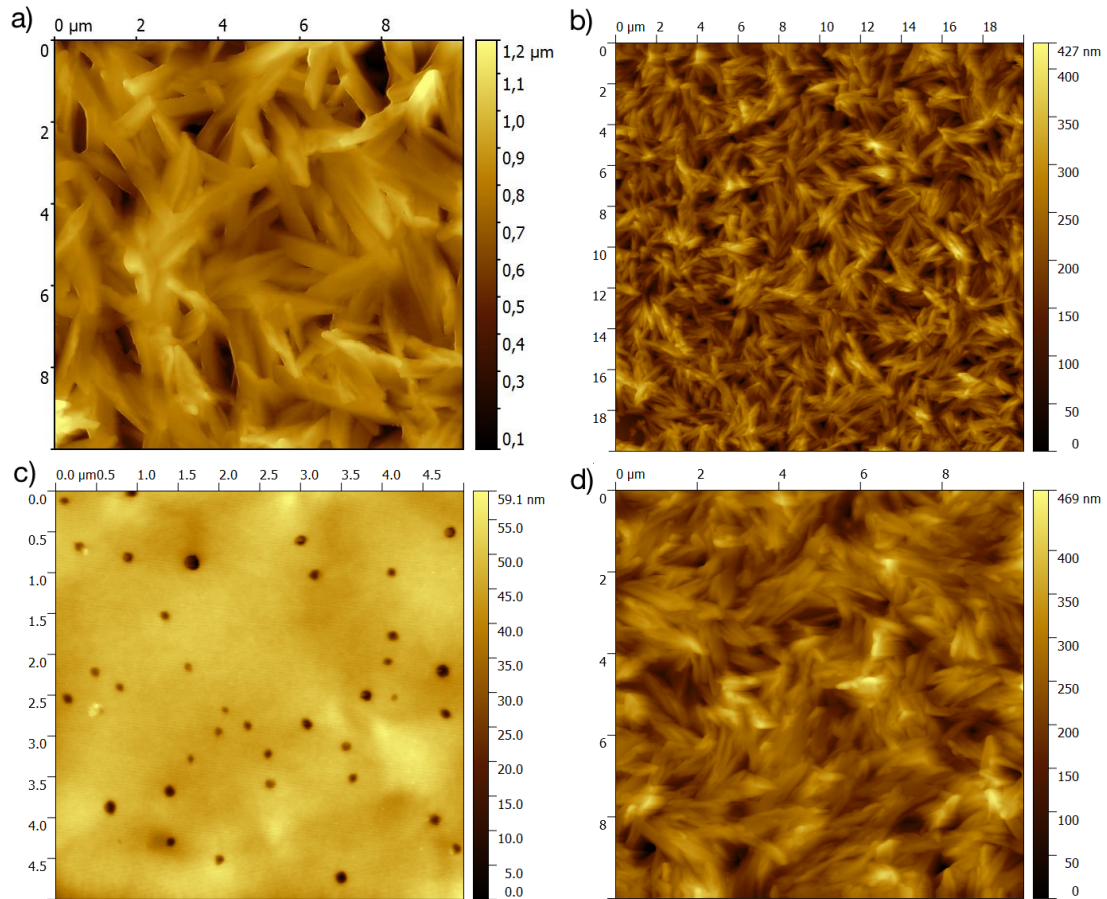
Figure 8-9: Image (a) and (b) are the AFM images of TPD_{C8}-TAT_{C8} films in cold crystalline state with different scanning scale (a: 10 μm and b: 20 μm). Image (c) is the AFM image TPD_{C8}-TAT_{C8} films after passing the isotropic phase (180°C). Image (d) is the AFM image TPD_{C8}-TAT_{C8} films in crystalline phase after passing the isotropic phase.

The AFM images for PEDOT:PSS/TPD_{EH}-TAT_{C8} films at different phases are shown in Figure 8-10. Image (a) shows the AFM images of TPD_{EH}-TAT_{C8} films in crystalline state. We observe that the crystal grains are distributed in the film, with smaller sizes than the TPD_{C8}-TAT_{C8} crystal needles. As a result, the TPD_{EH}-TAT_{C8} film roughness is less pronounced than TPD_{C8}-TAT_{C8} films. Moreover, the charge transport measurements of TPD_{EH}-TAT_{C8} films reveal that TPD_{EH}-TAT_{C8} crystal grains do not lead to higher SCLC mobility at crystalline state. Image (b) shows that at the film is destroyed by the annealing and no longer continuous, thus, the mobility in the nematic state could not be measured.
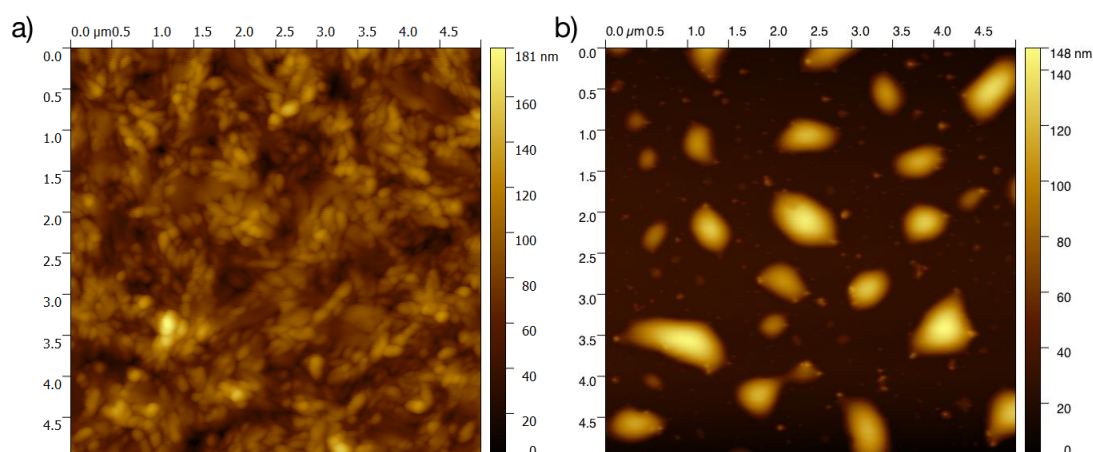
Figure 8-10: (a) AFM images of PEDOT:PSS/TPD$_{EH}$-TAT$_{C8}$ films in cold crystalline state. (B) AFM image of PEDOT:PSS/TPD$_{EH}$-TAT$_{C8}$ films after passing the isotropic phase (180°C), the film is dewetted.

8.2.3 HMDS/TPD$_{C8}$-TAT$_{C8}$ films

The AFM measurements on pure TPD$_{C8}$-TAT$_{C8}$ films in SCLC devices show that needle-like crystals are obtained in the crystalline phase. Those crystals promote the charge transport, leading to the high out-of-plane mobility. Moreover, the crystallization process can be repeated through thermal annealing, with equal charge transport efficiency. However, the in-plane charge transport in the crystalline state is not as efficient as the out-of-plane transport. Therefore, AFM was conducted to explore the differences in film morphology that could possibly be at the origin of this discrepancy.

In OFETs, TPD$_{C8}$-TAT$_{C8}$ films is deposited on top of HMDS with the same cold crystallization process as for SCLC devices (100°C for 5 mins, 120°C for 5 mins and 130°C for 5 mins). Two films with different thicknesses have been scanned by AFM. Figure 8-11a shows a TPD$_{C8}$-TAT$_{C8}$ film in the crystalline state. We observe that micrometer sized crystalline needles are randomly distributed all over the surface and overlap with each other. However, the crystals do not cover the entire surface, leaving 'holes' between them. The density of the crystals is increased in thicker as-deposited films (Figure 8-11b).

The charge transport measurements, reported in chapter 6, have been performed on these two films. For the thicker film, the field-effect mobility

equals $(6.2\pm2) \times 10^{-3}$ cm^2 V^{-1} s^{-1}, which is almost a factor of 3 higher than the mobility for the thinner film $((2.1\pm2) \times 10^{-3}$ cm^2 V^{-1} s^{-1}). Because the channel length is much larger than the size of one single crystal, the charges need to hop among overlapping crystals that connect the source and drain electrodes. A higher crystal density leads to more overlapping crystals, resulting in more paths for charges to traverse through and thus a higher mobility.

Comparing the AFM images obtained on OFET and SCLC devices, it can be seen that the density of crystal needles in SCLC active layer is, as expected, much higher than the OFET films.

The incomplete coverage of the OFET channel leads to an underestimation of the mobility, and therefore contributes to the observed difference between in-plane and out-of-plane transport.

The size of crystal needles depends on the dielectric materials. Image (c) presents the AFM image of TPD$_{C8}$-TAT$_{C8}$ film deposited on a dielectric material developed by Rolic Technologies Ltd. Details on this material cannot be provided for confidentiality reasons. Nevertheless, we can see that the crystals are much bigger, up to 10 μm long. This result points out that the crystal growth is kinetically controlled by the molecular surface diffusion and that the later depends on the interfacial interaction between the molecules and the substrate.

Note that, since the total film volume is conserved during annealing (neglecting possible changes in the material density), larger crystals are necessarily more separated, as can be seen in Figure 8-11.

It would be worth to optimize crystal growth conditions further. Indeed, if crystals large enough to bridge both electrodes could be grown, intra-grain charge transport could be investigated. It is likely that the corresponding mobility would be closer to the mobility measured by SCLC, where a small number of crystals (eventually only one) are connecting both electrodes.
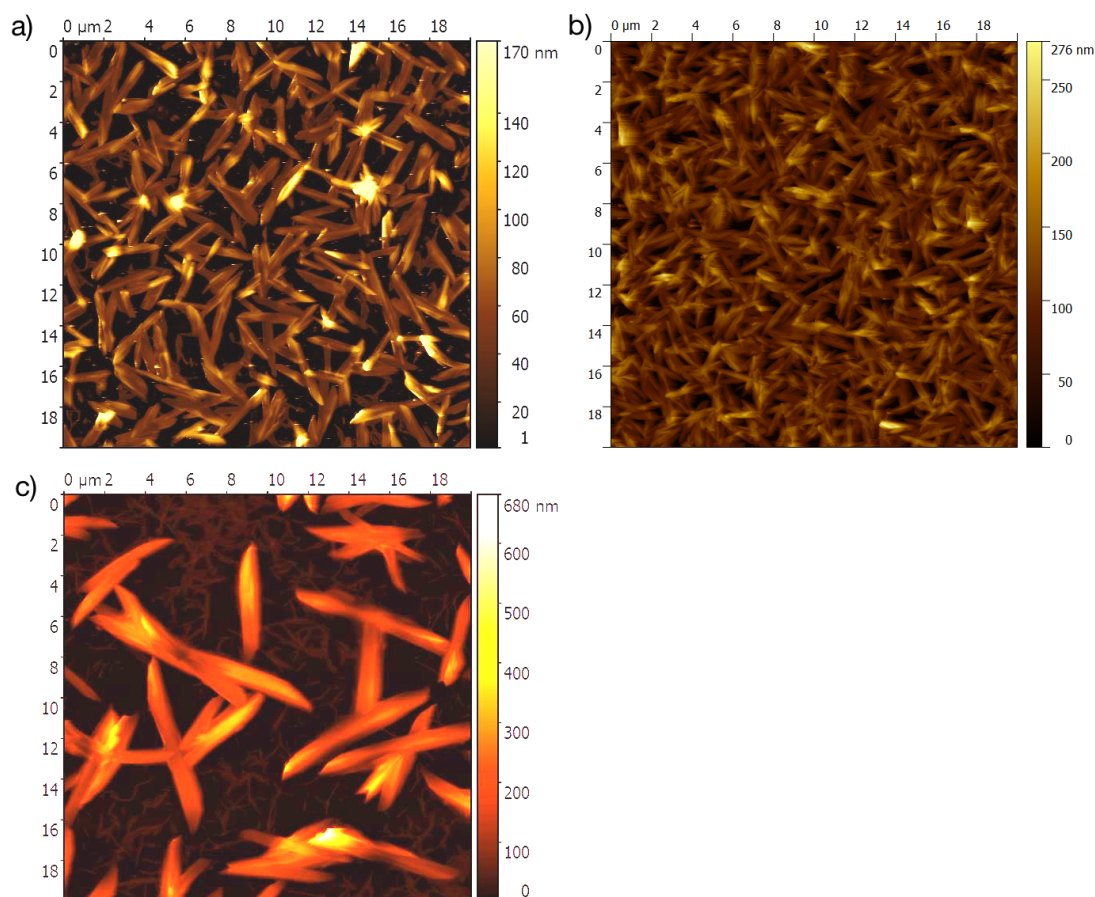
Figure 8-11: Image a) and b) are the AFM images of HMDS/TPD$_{C8}$-TAT$_{C8}$ films in cold crystalline state with different concentration of TPD$_{C8}$-TAT$_{C8}$. Image c) is the AFM image TPD$_{C8}$-TAT$_{C8}$ films on a different dielectric in cold crystalline state.

8.2.4 Conductive-AFM measurement on TPD$_{C8}$-TAT$_{C8}$ films

In the previous section, we found out that the charge transport of TPD$_{C8}$-TAT$_{C8}$ films may be influenced by the connectivity of the crystals. We tried to address this issue further by using conductive-AFM (C-AFM) in a configuration reported previously by Hourani *et al.* to study charge transport along single crystals of (3HT)$_8$[129]. Figure 8-12 shows the schematic of the C-AFM applied to a single crystal in contact with a gold electrode. The AFM tip is used to apply a positive voltage to the crystal with respect the gold electrode, which is kept at the same potential than the substrate.
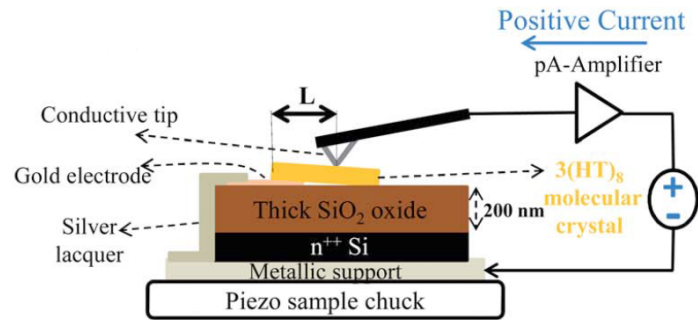
Figure 8-12: Schematic of the C-AFM mode AFM with the single crystal deposited on the FET structure, adapted from reference [128].

Figure 8-13a shows an optical micrograph of three connected crystals. Only crystal number 1 was connected to the gold electrode, while no.2 and 3 are connected to the electrode by crystal no.1. Figure 8-13b and c shows the topography and corresponding current image with applied voltage of -3 V. The current image illustrates that the current along crystal no.1 decreases as the distance from the electrode increases. The authors showed that this evolution can be described in terms of a space-charge limited current with a hole mobility of ~ 1×10^{-3} cm^{2}V^{-1}s^{-1}. Furthermore, the current in crystal no.2 and 3 is lower than the current in crystal no.1, pointing out the "contact resistance" among single crystals (see Figure 8-13d).
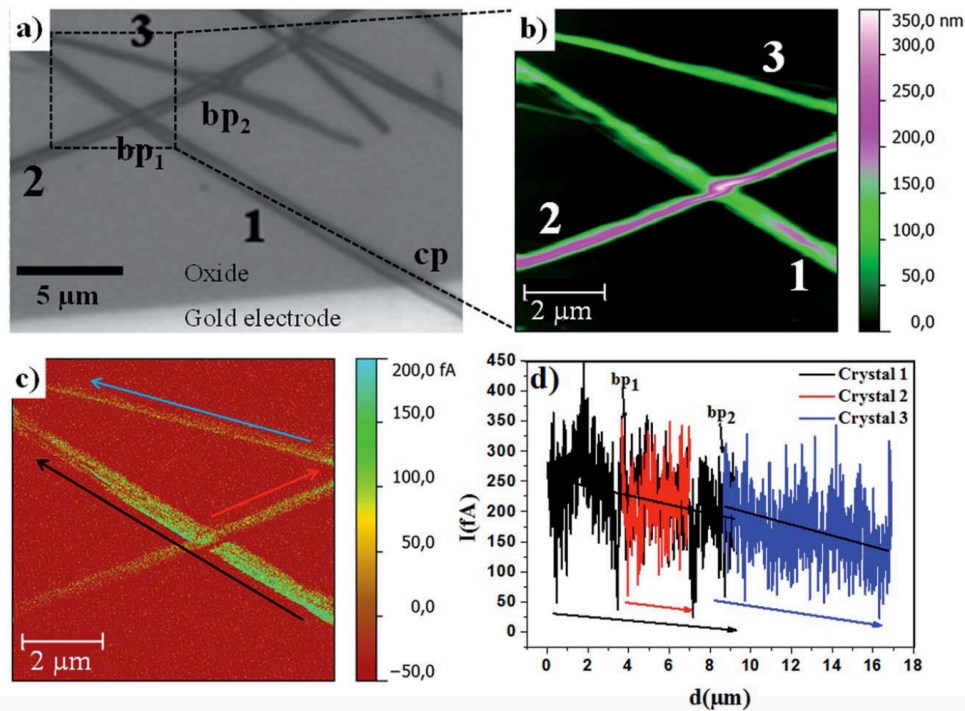
Figure 8-13: Three single crystals based on (3HT)$_8$ connected to each other. a) Optical micrograph showing the three crystals: no.1 connected to the gold electrode and connecting

the other two crystals no.2 and 3, which were completely laid on the oxide, to the electrode. (b) AFM topographic image of the three crystals. (c) Current image of the three crystals for an applied voltage of -3 V on the substrate. bp1: bridging point between crystals no. 1 and 2, bp2: bridging point between crystals no. 2 and 3. (d) Currents measured as a function of the distance d for the 3 inter- connected single crystals no. 1–3 along the arrows indicated in (c). Adapted from Reference [128].

We tried to use the same method to investigate the charge transport in the TPD_{C8}-TAT_{C8} crystalline needles. In our case, the silicon substrate was isolated from the gold electrode, allowing the latter to be used as a gate electrode. The measurements were performed at the IS2M[a] with the help of Dr. Jean-Luc Bubendorff.

Negative voltages (from 0 to -60 V) were applied to both the drain (gold electrode) and substrate (gate electrode), the tip being grounded (source electrode) (see Figure 8-14). Figure 8-15 shows the height topography (left) and corresponding current image at V_d= -300 mV. The electrode is close to the crystals on the right side. It is observed that most crystals are connected to the electrode since the appear bright in the current image. Interestingly, the current remains rather constant along the needle, suggesting that the current is injection-limited rather than space-charge limited, which may occur if the mobility is too high. Unfortunately, at the present stage, we cannot give a quantitative estimate of the corresponding mobility.

Note that the crystals which are not connected to the electrode, appear dark (circled area). This confirms that the current is not due to possible leakage currents.

The maximum current observed on our crystals is on the order of 10 pA (under - an applied voltage of 300 mV), which is much larger than the 200 fA measured on $(3HT)_8$ crystals under V_d= -3 V using the same experimental set-up in reference [128]. These results therefore suggest that the charge transport in TPD_{C8}-TAT_{C8} crystals is much more efficient than in $(3HT)_8$ crystals.

---

[a] Institut de Sciences des Matériaux de Mulhouse, Mulhouse, France
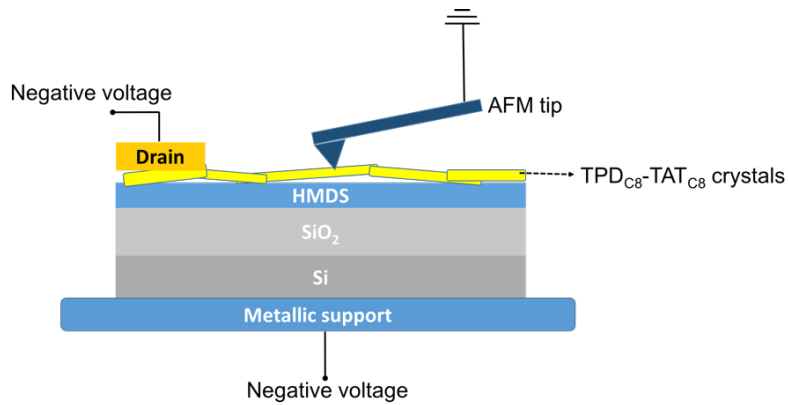
Figure 8-14: Schematic of the Conductive-AFM mode AFM with the TPD_{C8}-TAT_{C8} crystals on the FET structure.
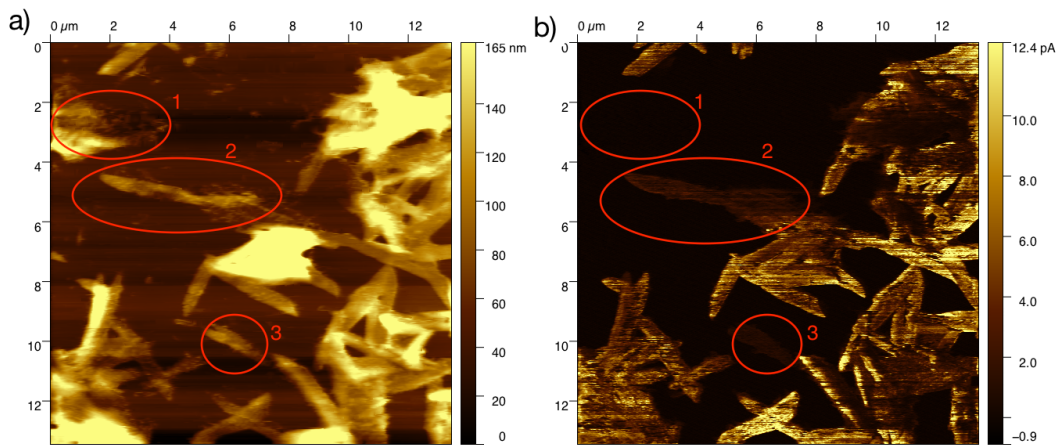
Figure 8-15: (a) AFM topographic image of the needle-like crystals and (b) Current image of the TPD_{C8}-TAT_{C8} crystals for gate voltage V_g=0 V and drain V_{ds}=-300 mV.

We also measured the I-V characteristics for different gate voltage with the goal to observe a field effect and determine the charge carrier mobility. The gate voltage was changed from 0 to -60 V while the drain voltage V_d was swept periodically from 0 to 10 V. The Id-Vd curve is shown below in Figure 8-16. We can clearly observe a field effect, with the drain current increasing with the gate voltage. However, the result was not reproducible: a significant drift in current was measured when the gate voltage was set back to its initial value. It is likely that the crystals are damaged by the AFM tip.
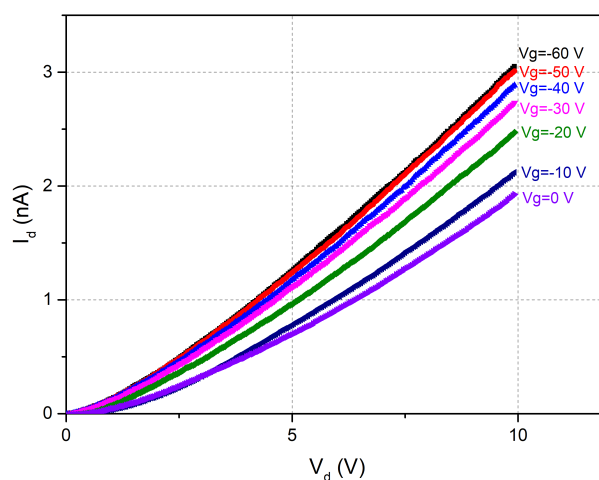
Figure 8-16: I_d-V_d characteristics of connected crystals with Vg varies from 0 to -60 V.

8.3 Conclusion

In conclusion, GIWAXS and AFM measurements have been performed to analyze the film morphologies on TPD-TAT:fullerene blend films and pure TPD_{C8}-TAT_{C8} films at different states. The GIWAXS measurements of TPD-TAT:fullerene blend films with different D:A weight ratio reveal that the presence of $PC_{71}BM$ does not change significantly the molecular packing of the donor molecules. The measurements for HMDS/TPD_{C8}-TAT_{C8} films in different solid states are in agreement with the SAXS pattern of bulk TPD_{C8}-TAT_{C8} and confirm the presence of a nematic columnar phase.

AFM measurements were used to investigate the thin film topography. For BHJ active layers, no macroscopic phase separation between the fullerene and the TPD-TAT molecules has been observed. For TPD_{C8}-TAT_{C8} films in the crystalline state, micrometer sized randomly distributed crystalline needles are observed. Those needles are connected to each other and contribute to the charge transport. Conductive-AFM was also performed to characterize transport across the crystal needles. The results suggest that the charge transport is more efficient than in the monocrystalline $(3HT)_8$ crystals.

CHAPTER 9
Conclusion

The domain of bulk heterojunction organic solar cells has drawn many attention over last two decades and the efficiency has reached remarkable values over 13 % for polymer-based BHJ devices. At the same time, small molecules or molecular semiconductors based solar cells have been developed and achieved PCE is over 10 %. This impressive progress is due to the development of new organic semiconductor materials, better control of morphology of thin-films and improved device architectures.

Compared to π-conjugated polymers, the use of molecular semiconductors for organic solar cells have several advantages: better control of molecular structure, more efficient purification processes and therefore, better reproducibility of performance.

Molecular semiconductors, consisting of an alternation of electron-donor (D) and electron-acceptor (A) groups, to form D-A-D or A-D-A structures, have achieved good photovoltaic performances. This synthesis strategy could precisely adjust the energy of frontier molecular orbitals (FMO). In addition, this type of structure allows better control of the molecular assembly, which is essential for efficient charge transport, and consequently, for high photovoltaic

efficiency. It should be noted that charge transport is a key factor that often limits the photovoltaic performance of organic solar cells.

A possible approach to improve molecular self-assembly for better charge transport is to add planar units to molecules. The planar structure can facilitates the π-π stacking and enhances the intermolecular interactions, resulting in high charge carrier mobility and allowing the efficient charge extraction in solar cells. Using these two strategies, many molecular semiconductors have been synthesized and used in photovoltaic devices. Among them, dumbbell-shaped molecules that combine electron-rich planar end-groups with an electron-deficient central unit have achieved promising photovoltaic performances in BHJ solar cells.

In this context, this thesis focused on the in-depth study of a series of dumbbell-shaped electron-donor molecules, whose planar end-groups is triazatruxene (TAT) and the electron-deficient core is thieo-pyrrole dione (TPD). This series of molecules are distinguished by the nature of the alkyl side-chains attached to the central core and end-groups. More precisely, the relationship between the nature of side-chains and molecular and thermal properties of these dumbbell-shaped molecules have been studied in detail. The impact of alkyl chains on nanoscale thin-film morphology has also been investigated. In order to better understand the influence of the microstructure of thin-films on charge transport, in-plane and out-of-plane mobilities were measured in different solid states of the materials (glassy, crystalline and nematic). BHJ solar cells in blends with fullerene derivatives were also realized.

We first explored the molecular and bulk material properties of all molecules. The characterization of electrochemical properties by cyclic voltammetry showed that those compounds have almost identical HOMO and LUMO levels at - 5.3 and -3.3 eV, respectively, leading to a CV energy-gap of 2.0 eV. This value suggests that these molecules have potentials to be used as electron donors in BHJ solar cells.

The UV-visible absorption spectra in solution (chloroform) overlap perfectly, revealing that the molecular conformation and the related conjugation length in

solution are not affected by the side chains. In the solid-state, all the spectra are red-shifted and broadened. The absorption spectra of TPD_{C8}-TAT_{C8} and TPD_{EH}-TAT_{C8} exhibit larger red-shifts and vibronic peaks than those molecules with ramified side-chains on the TAT units. Those results indicate that linear chains on the TAT units lead to a higher structural order and more pronounced intermolecular interactions in solid-state. On the other hand, the side-chains on the TPD unit do not change notably these properties. We therefore conclude that the intermolecular interactions in these dumbbell-shaped molecules are essentially controlled by the TAT units, which are thus the major driving force for the molecular self-assembly.

This conclusion was further confirmed by the differential scanning calorimetry (DSC) measurements. The molecules having ramified side-chains on TAT units only showed a glass transition, while those having linear side-chains on TAT exhibited a nematic and crystalline phases.

The SAXS measurements on the bulk materials in the glassy states reveal the relationships between self-organization and the side-chains attached to the TAT moieties. When the TAT units possess linear C_8 chains, the SAXS patterns in the frozen nematic phase are typical of a nematic columnar organization. While for the molecules where the TAT is functionalized by EH branched side-chains, the patterns are characteristic of amorphous compounds. This result agrees with the previous observations on UV-vis and DSC measurements. Therefore, one can note that the molecules bearing linear side-chains on TAT have more ordered molecular packing, which lead to efficient intermolecular interactions, and, as a corollary, high photovoltaic performances.

The next part of this thesis focused on the electronic properties of the synthesized molecules. Charge-carrier mobility measurements have been performed on both as-deposited and annealed films using organic field-effect transistors (OFET) and space-charge-limited-current (SCLC) devices. The OFET mobilities in as-deposited state are relatively low for all molecules, except for TPD_{C8}-TAT_{C8}, for which the mobility is almost ten times higher for the others. Moreover, in the crystalline phase, the mobilities is more than ten times higher

than in the glassy state for crystallized molecules, indicating a more ordered molecular packing. The SCLC mobilities show the same tendency, that TPD$_{C8}$-TAT$_{C8}$ exhibit the highest mobility, and is much higher than its OFET mobility, indicating an anisotropic charge transport. Especially in the crystalline phase, the SCLC mobility for TPD$_{C8}$-TAT$_{C8}$ is in the order of 10^{-1} cm^2 V^{-1} s^{-1}, which is an ultra-high value for organic small molecule donors.

The photovoltaic properties were then investigated by blending TPD-TAT derivatives with PC$_{71}$BM. Fill factors exceeding 60 % have been obtained with the most structurally ordered molecule TPD$_{C8}$-TAT$_{C8}$ and a PCE over 4 %, which is close to the one obtained with P$_3$HT, a reference polymer with a similar energy band gap.

The GIWAXS measurement revealed the molecular organization in different solid states for pure molecules and also of the blends with fullerene acceptors. Atomic force microscopy (AFM) analysis showed the surface morphologies of films of those molecules. We found that in the crystalline state, needle-like crystals appeared in the film, which contribute to efficient charge transport.

Overall, these results allowed us to better understand the contribution of various molecular groups on the molecular self-assembly and on the optoelectronic properties. We have thus been able to demonstrate that the impact of the alkyl chains associated with the TAT planar units on the self-assembly properties takes priority over that of the chains on the central group TPD. In other words, the TAT groups play a decisive role in the molecular organization in the solid state.

The study of charge mobility by two complementary techniques confirm the favorable influence of the TAT units on the molecular self-assembly and the resulting opto-electronic and photovoltaic properties. In particular, an extraordinary high hole mobility has been achieved, with the peculiarity of being highest in the direction perpendicular to the plane of the substrate. Since the charge collection within a photovoltaic cell takes place precisely along this direction, these transport properties have given rise to promising photovoltaic performances.

This three years' study has left some open issues, which will need additional investigations of TAT-based dumbbell-shaped molecules. To further understand the relationship between molecular assembly and devices properties, molecules with DPP as central core with TAT end-groups should be investigated, since DPP unit can decrease the energy band-gap, and improve photovoltaic performance.

Bibliography

1. *Based on IEA data from the Key World Energy Statistics © OECD/IEA 2016, www.iea.org/statistics. Licence: www.iea.org/t&c; as modified by Tianyan HAN.*

2. Becquerel, A.-E. Mémoire sur les effets électriques produits sous l'influence des rayons solaires. *Compte Rendu l'Académie des Sci.* 9–561 (1839).

3. Chapin, D. M., Fuller, C. S. & Pearson, G. L. A New Silicon p-n Junction Photocell for Converting Solar Radiation into Electrical Power. *J. Appl. Phys.* **25**, 676–677 (1954).

4. Green, M. A. *et al.* Solar cell efficiency tables (version 50). *Prog. Photovoltaics Res. Appl.* **25**, 668–676 (2017).

5. Mazzio, K. A. & Luscombe, C. K. The future of organic photovoltaics. *Chem. Soc. Rev.* **44**, 78–90 (2014).

6. Yu, G., Gao, J., Hummelen, J. C., Wudl, F. & Heeger, A. J. Polymer Photovoltaic Cells: Enhanced Efficiencies via a Network of Internal Donor-Acceptor Heterojunctions. *Science (80-.).* **270**, 1789–1791 (1995).

7. Zhao, W. *et al.* Molecular Optimization Enables over 13% Efficiency in Organic Solar Cells. *J. Am. Chem. Soc.* **139**, 7148–7151 (2017).

8. Kan, B. *et al.* A series of simple oligomer-like small molecules based on oligothiophenes for solution-processed solar cells with high efficiency. *J. Am. Chem. Soc.* **137**, 3886–3893 (2015).

9. Geraghty, P. B. *et al.* High performance p-type molecular electron donors for OPV applications via alkylthiophene catenation chromophore extension. *Beilstein J. Org. Chem.* **12**, 2298–2314 (2016).

10. Bura, T. *et al.* High-Performance Solution-Processed Solar Cells and Ambipolar Behavior in Organic Field-Effect Transistors with Thienyl-BODIPY Scaffoldings. *JACS* 2–5 (2012).

11. Bura, T. *et al.* Triazatruxene-diketopyrrolopyrrole dumbbell-shaped molecules as photoactive electron donor for high-efficiency solution processed organic solar cells. *Adv. Energy Mater.* **3**, 1118–1124 (2013).

12. Bulut, I. *et al.* Thiazole-based scaffolding for high performance solar cells. *J. Mater. Chem. C* **4,** 4296–4303 (2016).

13. Brutting, W. & Adachi, C. *Physics of Organic Semiconductors*. (2005).

14. Shirakawa, H., Louis, E. J., Macdiarmid, A. G., Chiang, C. K. & Heeger, A. J. Synthesis of Electrically Conducting Organic Polymers : Halogen Derivatives of Polyacetylene, (CH)x. *J.C.S. CHEM. COMM.* 578–580 (1977).

15. Hoppe, H. & Sariciftci, N. S. Organic solar cells : An overview. *J. Mater. Res.* **19,** 1924–1945 (2004).

16. Ostroverkhova, O. Organic Optoelectronic Materials : Mechanisms and Applications. *Chem. Rev.* **116,** 13279–13412 (2016).

17. Kumar, P. *Organic Solar Cells: Device Physics, Processing, Degradation, and Prevention*. (2016).

18. Henson, Z. B., Müllen, K. & Bazan, G. C. Design strategies for organic semiconductors beyond the molecular formula. *Nat. Chem.* **4,** 699–704 (2012).

19. Mishra, A. & Bauerle, P. Small molecule organic semiconductors on the move: Promises for future solar energy technology. *Angew. Chemie - Int. Ed.* **51,** 2020–2067 (2012).

20. Collins, S. D., Ran, N. A., Heiber, M. C. & Nguyen, T. Small is Powerful: Recent Progress in Solution-Processed Small Molecule Solar Cells. *Adv. Energy Mater.* (2017). doi:10.1002/AENM.201602242

21. Roncali, J., Leriche, P. & Blanchard, P. Molecular materials for organic photovoltaics: Small is beautiful. *Adv. Mater.* **26,** 3821–3838 (2014).

22. Hudhomme, P. An overview of molecular acceptors for organic solar cells. *EPJ Photovoltaics* **40401,** (2013).

23. Anthony, J. E., Facchetti, A., Heeney, M., Marder, S. R. & Zhao, X. n-Type Organic Semiconductors in Organic Electronics. *Adv. Mater.* **22,** 3876–3892 (2010).

24. Shockley, W. & Queisser, H. J. Detailed Balance Limit of Efficiency of pn Junction Solar Cells. *J. Appl. Phys.* **32,** 510–519 (1961).

25. Wannier, G. H. The Structure of Electronic Excitation Levels in Insulating Crystals. *Phys. Rev.* **52,** 191–197 (1937).

26. Sariciftci, N. S., Smilowitz, L., Heeger, A. J. & Wudi, F. Photoinduced Electron Transfer from a Conducting Polymer to Buckminsterfullerene. *Science (80-.).* **258,** 1474–1476 (1992).

27. Hwang, I., Moses, D. & Heeger, A. J. Photoinduced Carrier Generation in P3HT / PCBM Bulk Heterojunction Materials. *J. Mater. Chem. C* **17,** 4350–4354 (2008).

28. Mikhnenko, O. V, Blom, P. W. M. & Nguyen, T. Exciton diffusion in organic semiconductors. *Energy Environ. Sci.* **8,** 1867–1888 (2015).

29. Lunt, R. R., Giebink, N. C., Belak, A. a., Benziger, J. B. & Forrest, S. R. Exciton diffusion lengths of organic semiconductor thin films measured by spectrally resolved photoluminescence quenching. *J. Appl. Phys.* **105,** 1–7 (2009).

30. Tamai, Y., Ohkita, H., Benten, H. & Ito, S. Exciton Diffusion in Conjugated Polymers: From Fundamental Understanding to

Improvement in Photovoltaic Conversion Efficiency. *J. Phys. Chem. Lett.* **6,** 3417–3428 (2015).

31. Stübinger, T. & Brütting, W. Exciton diffusion and optical interference in organic donor–acceptor photovoltaic cells. *J. Appl. Phys.* **90,** 3632–3641 (2001).

32. Stübinger, T. & Brütting, W. Exciton diffusion and optical interference in organic donor – acceptor photovoltaic cells. *J. Appl. Phys.* **90,** 3632–3641 (2001).

33. Halls, J. J. M., Pichler, K. & Friend, R. H. Exciton diffusion and dissociation in a poly (p - phenylenevinylene)/C60 heterojunction photovoltaic cell. *Appl. Phys. Lett.* (1996). doi:10.1063/1.115797

34. Markov, D. E., Hummelen, J. C., Blom, P. W. M. & Sieval, A. B. Dynamics of exciton diffusion in poly(p-phenylene vinylene)/fullerene heterostructures. *Phys. Rev. B* **72,** 45216 (2005).

35. Buxton, G. A. & Clarke, N. Predicting structure and property relations in polymeric photovoltaic devices. *Phys. Rev. B* **74,** 085207 1-5 (2006).

36. Mihailetchi, V. D., Koster, L. J. A., Hummelen, J. C. & Blom, P. W. M. Photocurrent Generation in Polymer-Fullerene Bulk Heterojunctions. *Phys. Rev. Lett.* **93,** 19–22 (2004).

37. Deibel, C., Dyakonov, V. & Brabec, C. J. Organic Bulk-Heterojunction Solar Cells. *IEEE J. Sel. Top. QUANTUM Electron.* **16,** 1517–1527 (2010).

38. Lee, J., Kovalenko, M. V, Huang, J., Chung, D. S. & Talapin, D. V. Band-like transport , high electron mobility and high photoconductivity in all-inorganic nanocrystal arrays. *Nat. Nanotechnol.* **6,** 348–352 (2011).

39. Fischetti, M. V. & E., S. Monte Carlo analysis of electron transport in small semiconductor devices including band-structure and space-charge efFects Massimo. *Phys. Rev. B* **38,** (1988).

40. Miller, A. & Abrahams, E. Impurity Conduction at Low Concentrations. *Phys. Rev.* **120,** 745–755 (1960).

41. Marcus, R. A. Electron transfer reactions in chemistry Theory and experiment. *J. Electroanal. Chem.* **438,** 251–259 (1997).

42. Baranovskii, S. D., Cordes, H., Hensel, F. & Leising, G. Charge-carrier transport in disordered organic solids. *Phys. Rev. B* **62,** 7934–7938 (2000).

43. Li, Y., Clevenger, R. G., Jin, L., Kilway, K. V. & Peng, Z. Unusually high SCLC hole mobility in solution-processed thin films of a polycyclic thiophene-based small-molecule semiconductor. *J. Mater. Chem. C* **2,** 7180 (2014).

44. Yuan, Y. *et al.* Ultra-high mobility transparent organic thin film transistors grown by an off-centre spin-coating method. *Nat. Commun.* **5,** 3005 (2014).

45. Coropceanu, V. *et al.* Charge Transport in Organic Semiconductors. *Chem.Rev.* **107,** 926–952 (2007).

46. Bassler, H. Charge Transport in Disordered Organic Photoconductors A Monte Carlo Simulation Study. *Basic Solid State Phys.* **175,** (1993).

47. Foertig, A. *et al.* Nongeminate and Geminate Recombination in PTB7 : PCBM Solar Cells. *Adv. Funct. Mater.* **24,** 1306–1311 (2014).

48. Pal, S. K. *et al.* Geminate Charge Recombination in Polymer/ Fullerene Bulk Heterojunction Films and Implications for Solar Cell Function. *JACS* 12440–12451 (2010).

49. Faist, M. A. *et al.* Understanding the Reduced Efficiencies of Organic Solar Cells Employing Fullerene Multiadducts as Acceptors. *Adv. Energy Mater.* **3,** 744–752 (2013).

50. Shuttle, C. G. *et al.* Bimolecular recombination losses in polythiophene : Fullerene solar cells. *Phys. Rev. B* **78,** 113201 (2008).

51. Burke, T. M., Sweetnam, S., Vandewal, K. & Mcgehee, M. D. Beyond Langevin Recombination : How Equilibrium Between Free Carriers and Charge Transfer States Determines the Open-Circuit Voltage of Organic Solar Cells. *Adv. Energy Mater.* **5,** 1500123 (2015).

52. Bartesaghi, D. *et al.* Competition between recombination and extraction of free charges determines the fill factor of organic solar cells. *Nat. Commun.* **6,** 7083 (2015).

53. Wagenpfahl, A., Rauh, D., Binder, M., Deibel, C. & Dyakonov, V. S-shaped current–voltage characteristics of organic solar devices. *Phys. Rev. B* **82,** 115306 (2010).

54. Wagenpfahl, A. J. Numerical simulations on limitations and optimization strategies of organic solar cells. (2013).

55. Park, Y., Choong, V., Gao, Y., Hsieh, B. R. & Tang, C. W. Work function of indium tin oxide transparent conductor measured by photoelectron spectroscopy. *Appl. Phys. Lett.* **68,** 2699–2701 (1996).

56. Kim, J. S. *et al.* Indium – Tin Oxide Treatments for Single- and Double-Layer Polymeric Light-Emitting Diodes : The Relation Between the anode physical, chemical, and morphological properties and the device performance. *J. Appl. Phys.* **84,** 6859–6870 (1998).

57. Rauh, D., Wagenpfahl, A., Deibel, C. & Dyakonov, V. Relation of open circuit voltage to charge carrier density in organic bulk heterojunction solar cells. *Appl. Phys. Lett.* **98,** 133301 (2011).

58. Shrotriya, B. V. *et al.* Accurate Measurement and Characterization of Organic Solar Cells. *Adv. Funct. Mater.* **16,** 2016–2023 (2006).

59. Dennler, B. G., Scharber, M. C. & Brabec, C. J. Polymer-Fullerene Bulk-Heterojunction Solar Cells. *Adv. Mater.* **21,** 1323–1338 (2009).

60. Lattante, S. Electron and Hole Transport Layers: Their Use in Inverted Bulk Heterojunction Polymer Solar Cells. *electronics* **3,** 132–164 (2014).

61. Chamberlain, G. a., Cooney, P. J. & Dennison, S. Photovoltaic properties of merocyanine solid-state photocells. *Nature* **289,** 45–47 (1981).

62. Antoniadis, H., Hsieh, B. R., Abkowitz, M. A., Jenekhe, S. A. & Stolka, M. Photovoltaic and photoconductive properties of aluminum/poly(p-phenylene vinylene) interfaces. *Synth. Met.* **62,** 265–271 (1994).

63. Ghosh, A. K. & Feng, T. Merocyanine organic solar cells. *J. Appl. Phys.* **49,** 5982–5989 (1978).

64. Glenis, S., Horowitz, G., Tourillon, G. & Garnier, F. 93 electrochemically grown polythiophene and poly(3-methylthiophene) organic photovoltaic cells. *Thin Solid Films* **111,** 93–103 (1984).

65. Ghosh, A. K. & Feng, T. Merocyanine organic solar cells. *J. Appl. Phys.* **49,** 5982–5989 (1978).

66. Tang, C. W. Two-layer organic photovoltaic cell. *Appl. Phys. Lett.* **48,** 183–185 (1986).

67. Sariciftci, N. S. *et al.* Semiconducting polymer?buckminsterfullerene heterojunctions: Diodes, photodiodes, and photovoltaic cells. *Appl. Phys. Lett.* **62,** 585–587 (1993).

68. Heeger, A. J. 25th anniversary article: Bulk heterojunction solar cells: Understanding the mechanism of operation. *Adv. Mater.* **26,** 10–28 (2014).

69. Brabec, C. J. *et al.* Origin of the open circuit voltage of plastic solar cells. *Adv. Funtional Mater.* **11,** 374–380 (2001).

70. Elumalai, N. K. & Uddin, A. Open circuit voltage of organic solar cells: an in-depth review. *Energy Environ. Sci.* **9,** 391–410 (2016).

71. Widmer, J., Tietze, M., Leo, K. & Riede, M. Open-circuit voltage and effective gap of organic solar cells. *Adv. Funct. Mater.* **23,** 5814–5821 (2013).

72. Scharber, M. C. *et al.* Design rules for donors in bulk-heterojunction solar cells - Towards 10 % energy-conversion efficiency. *Adv. Mater.* **18,** 789–794 (2006).

73. Zhang, H. *et al.* Developing high-performance small molecule organic solar cells via a large planar structure and an electron-withdrawing central unit. *Chem. Commun.* **53,** 451–454 (2017).

74. Wolf, J. *et al.* Benzo[1,2-b:4,5-b']dithiophene-Pyrido[3,4-b]pyrazine Small-Molecule Donors for Bulk Heterojunction Solar Cells. *Chem. Mater.* acs.chemmater.5b04726 (2016). doi:10.1021/acs.chemmater.5b04726

75. Green, M. A. *et al.* Solar cell efficiency tables (version 49). *Prog. Photovolt Res. Appl.* **25,** 3–13 (2017).

76. Sun, K. *et al.* The role of solvent vapor annealing in highly efficient air-processed small molecule solar cells. *J. Mater. Chem. A* **2,** 9048 (2014).

77. Wang, J. L. *et al.* Solution-Processed Diketopyrrolopyrrole-Containing Small-Molecule Organic Solar Cells with 7.0% Efficiency: In-Depth Investigation on the Effects of Structure Modification and Solvent Vapor Annealing. *Chem. Mater.* **27,** 4338–4348 (2015).

78. Kumar, C. H. P. *et al.* Influence of thermal and solvent annealing on the morphology and photovoltaic performance of solution processed, D–A–D type small molecule-based bulk heterojunction solar cells. *RSC Adv.* **5,** 93579–93590 (2015).

79. Oniwa, K. *et al.* 2-Positional pyrene end-capped oligothiophenes for high performance organic field effect transistors_supporting information. *Chem. Commun. (Camb).* **52,** 4800–3 (2016).

80. Rajagopal, S. K., Salini, P. S. & Hariharan, M. S···π, π–π, and C–H···π Contacts Regulate Solid State Fluorescence in Regioisomeric Bisthiazolylpyrenes. *Cryst. Growth Des.* **16,** 4567–4573 (2016).

81. Qiao, Y., Zhang, J., Xu, W. & Zhu, D. Novel 2,7-substituted pyrene derivatives: Syntheses, solid-state structures, and properties. *Tetrahedron* **67,** 3395–3405 (2011).

82. Liu, Y., Zhou, J., Wan, X. & Chen, Y. Synthesis and properties of acceptor-donor-acceptor molecules based on oligothiophenes with tunable and low band gap. *Tetrahedron* **65,** 5209–5215 (2009).

83. Liu, Y. *et al.* Spin-coated small molecules for high performance solar cells. *Adv. Energy Mater.* **1,** 771–775 (2011).

84. Long, G. *et al.* A Series of Simple Oligomer-like Small Molecules Based on Oligothiophenes for Solution-Processed Solar Cells with High Efficiency. *J. Am. Chem. Soc.* **137,** 3886–3893 (2015).

85. Lee, O. P. *et al.* Efficient small molecule bulk heterojunction solar cells with high fill factors via pyrene-directed molecular self-assembly. *Adv. Mater.* **23,** 5359–5363 (2011).

86. BERGMAN, J. & Nils, E. Synthesis and studies of tris-indolobenzenes and related compounds. *Tetrahedron* **36,** 1445–1450 (1980).

87. Bergman, J. & Eklund, N. Synthesis of 2, 2'-biindolyls by coupling reactions. *Tetrahedron* **36,** 1439 (1980).

88. Gallego-Gõmez, F. *et al.* Very large photoconduction enhancement upon self-assembly of a new triindole derivative in solution-processed films. *Adv. Funct. Mater.* **21,** 738–745 (2011).

89. Valentine, R. A., Whyte, A., Awaga, K. & Robertson, N. New indole trimers as precursors for molecular electronic materials. *Tetrahedron Lett.* **53,** 657–660 (2012).

90. Rakstys, K. *et al.* Triazatruxene-Based Hole Transporting Materials for Highly Efficient Perovskite Solar Cells. *J. Am. Chem. Soc.* **137,** 16172–16178 (2015).

91. Huaulmé, Q., Cece, E., Mirloup, A. & Ziessel, R. Star-shaped panchromatic absorbing dyes based on a triazatruxene platform with diketopyrrolopyrrole and boron dipyrromethene substituents. *Tetrahedron Lett.* **55,** 4953–4958 (2014).

92. Bura, T. *et al.* Absorption tuning of monosubstituted triazatruxenes for bulk heterojunction solar cells. *Org. Lett.* **13,** 6030–6033 (2011).

93. Bulut, I. *et al.* LUMO's modulation by electron withdrawing unit modification in amorphous TAT dumbbell-shaped molecules. *J. Mater. Chem. A* **3,** 6620–6628 (2015).

94. Min, J. *et al.* Side-Chain Engineering for Enhancing the Properties of Small Molecule Solar Cells: A Trade-off Beyond Efficiency. *Adv. Energy Mater.* 1–9 (2016). doi:10.1002/aenm.201600515

95. Biniek, L. *et al.* Impact of the Alkyl Side Chains on the Optoelectronic Properties of a Series of Photovoltaic Low-Band-Gap Copolymers. *Macromolecules* **43,** 9779–9786 (2010).

96. Glatter, O. & Kratky, O. Small Angle X-ray Scattering. *Acad. Press* (1982).

97. Li, T., Senesi, A. J. & Lee, B. Small Angle X - ray Scattering for Nanoparticle Research. *Chem. Phys. Lett.* **116,** 11128–11180 (2016).

98. Leite, F. L. & Herrmann, P. S. P. Application of atomic force spectroscopy (AFS) to studies of adhesion phenomena : a review. *J. Adhes. Sci. Technol.* **19,** 365–405 (2005).

99. Principles, B. *Semiconductor physics and devices. Materials Today* **9,** (2006).

100.   Zaumseil, J. & Sirringhaus, H. Electron and Ambipolar Transport in Organic Field-Effect Transistors. *Chem. Rev.* **107,** 1296–1323 (2007).

101.   Fall, S. *et al.* Tailoring the microstructure and charge transport in conjugated polymers by alkyl side-chain engineering. *J. Mater. Chem.* **2,** 303 (2014).

102.   Vasimalla, S., Subbarao, N. V. V, Gedda, M., Goswami, D. K. & Iyer, P. K. Effects of Dielectric Material, HMDS Layer, and Channel Length on the Performance of the Perylenediimide-Based Organic Field-E ff ect Transistors. *ACS OMEGA* **2,** 2552–2560 (2017).

103.   Lampert, M. A. & Schilling, R. B. *Current Injection in Solids : The Regional Approximation Method.* (1970).

104.   Kutsarov, D. I. *et al.* Achieving 6.7% Efficiency in P3HT/Indene-C70 Bisadduct Solar Cells through the Control of Vertical Volume Fraction Distribution and Optimized Regio-Isomer Ratios. *Adv. Electron. Mater.* **2,** 1–28 (2016).

105.   Holliday, S. *et al.* High-efficiency and air-stable P3HT-based polymer solar cells with a new non-fullerene acceptor. *Nat. Commun.* **7,** 11585 (2016).

106.   Ruiz, C., López Navarrete, J. T., Ruiz Delgado, M. C. & Gómez-Lor, B. Triindole-bridge-triindole dimers as models for two dimensional microporous polymers. *Org. Lett.* **17,** 2258–2261 (2015).

107.   Bao, Z. & Locklin, J. J. *Organic field-effect transistors.* (CRC Press, 2007). at <https://books.google.fr/books?id=h-YzIELlTG8C&pg=PA151&lpg=PA151&dq=contact+resistance+in+OFET&source=bl&ots=TyybvXTLO2&sig=qttIfpLC7Hh6MUaKT3D2y-NyOIo&hl=fr&sa=X&ved=0ahUKEwjPtNiUop_WAhVHWhQKHb7oAGAQ6AEIZjAK#v=onepage&q=contact resistance in OFET&f=false>

108.   Roichman, Y. & Tessler, N. Charge transport in conjugated polymers - The influence of charge concentration. *Synth. Met.* **135–136,** 443–444 (2003).

109.   Wetzelaer, G. a H. & Blom, P. W. M. Ohmic current in organic metal-insulator-metal diodes revisited. *Phys. Rev. B - Condens. Matter Mater. Phys.* **89,** 1–5 (2014).

110.   García-Frutos, E. M. *et al.* High charge mobility in discotic liquid-crystalline triindoles: Just a core business? *Angew. Chemie - Int. Ed.* **50,** 7399–7402 (2011).

111.   Many, A., Harnik, E. & Gerlich, D. On the Semiconductivity of Crystalline Aromatic Substances. *J. Chem. Phys.* **23,** 1733–1734 (1955).

112.   Stallinga, P. *Electrical characterization of organic electronic materials and devices.* (John Wiley & Sons, 2009).

113.   Mao, L.-F., Ning, H., Hu, C., Lu, Z. & Wang, G. Physical Modeling of Activation Energy in Organic Semiconductor Devices based on Energy and Momentum Conservations. *Sci. Rep.* **6,** 24777 (2016).

114.   Phthalocyanine, I. On the Electric and Thermoelectric Properties of Copper Phthalocyanine Single Crystals ' 1. *phys. stat. sol.* **20,** 481 (1967).

115. Murdey, R. & Sato, N. Interpretation of the thermal activation energy of conduction for molecular semiconductor thin films with blocking contacts. *Jpn. J. Appl. Phys.* **53,** (2014).

116. Fielding, P. E. & Gutman, F. Electrical Properties of Phthalocyanines. *J. Chem. Phys.* **26,** 411–419 (1957).

117. Craciun, N. I., Wildeman, J. & Blom, P. W. M. Universal arrhenius temperature activated charge transport in diodes from disordered organic semiconductors. *Phys. Rev. Lett.* **100,** 1–4 (2008).

118. Proctor, C. M. *et al.* Understanding Charge Transport in Molecular Blend Films in Terms of Structural Order and Connectivity of Conductive Pathways. *Adv. Energy Mater.* 1–7 (2016). doi:10.1002/aenm.201502285

119. Vongsaysy, U. *et al.* Formulation strategies for optimizing the morphology of polymeric bulk heterojunction organic solar cells: a brief review. *J. Photonics Energy* **4,** 40998 (2014).

120. Arca, F., Loch, M. & Lugli, P. Enhancing efficiency of organic bulkheterojunction solar cells by using 1,8-diiodooctane as processing additive. *IEEE J. Photovoltaics* **4,** 1560–1565 (2014).

121. Wang, Z. *et al.* The underlying reason of DIO additive on the improvement polymer solar cells performance. *Appl. Surf. Sci.* **305,** 221–226 (2014).

122. Blom, P. W. M., Mihailetchi, V. D., Koster, L. J. A. & Markov, D. E. Device physics of polymer:Fullerene bulk heterojunction solar cells. *Adv. Mater.* **19,** 1551–1566 (2007).

123. He, Z. *et al.* Enhanced power-conversion efficiency in polymer solar cells using an inverted device structure. *Nat. Photonics* **6,** 593–597 (2012).

124. Dang, M. T., Hirsch, L. & Wantz, G. P3HT:PCBM, best seller in polymer photovoltaic research. *Adv. Mater.* **23,** 3597–3602 (2011).

125. Kumar, C. V. *et al.* Solvent Annealing Control of Bulk Heterojunction Organic Solar Cells with 6.6% Efficiency Based on a Benzodithiophene Donor Core and Dicyano Acceptor Units. *J. Phys. Chem. C* **119,** 20871–20879 (2015).

126. Colsmann, A., Junge, J., Kayser, C. & Lemmer, U. Organic tandem solar cells comprising polymer and small-molecule subcells. *Appl. Phys. Lett.* **89,** 2004–2007 (2006).

127. Ameri, T., Dennler, G., Lungenschmied, C. & Brabec, C. J. Organic tandem solar cells: A review. *Energy Environ. Sci.* **2,** 347 (2009).

128. Bura, T. *et al.* High-performance solution-processed solar cells and ambipolar behavior in organic field-effect transistors with thienyl-BODIPY scaffoldings. *J. Am. Chem. Soc.* **134,** 17404–17407 (2012).

129. Hourani, W. *et al.* Anisotropic charge transport in large single crystals of π-conjugated organic molecules. *Nanoscale* **6,** 4774–80 (2014).

136

Résumé en français

1. Introduction

La conception de cellules solaires organiques de type hétérojonction en volume (BHJ pour « Bulk Heterojunction ») a été proposée pour la première fois en 1990. Ces dispositifs sont composés d'un mélange de polymères conjugués, donneurs d'électrons, et de fullerènes, accepteur d'électrons, et ont pour la première fois permis d'atteindre un rendement de conversion énergétique significatif (de l'ordre de 2%) (PCE pour « Power Conversion Efficiency ») avec des semi-conducteurs organiques [1]. Depuis ce temps-là, l'intérêt pour ce domaine a augmenté continuellement et l'efficacité des dispositifs BHJ a connu une forte évolution, atteignant des valeurs remarquables de plus de 13 % pour des cellules solaires BHJ à base de polymères optimisés[2]. Dans le même temps, des cellules solaires organiques à base de « petites molécules » ou « semi-conducteurs moléculaires » (i.e. sans polymère), ont été développées et ont vu leur PCE atteindre 10% [3–5]. Ce progrès impressionnant doit beaucoup au développement de nouveaux matériaux semi-conducteurs organiques, à un meilleur contrôle de la morphologie des films minces ainsi qu'à l'amélioration de l'architecture des dispositifs[6–9].

Par rapport aux polymères π-conjugués, l'utilisation de semi-conducteurs moléculaires pour des cellules solaires organiques présente plusieurs avantages :

meilleur contrôle de la structure moléculaire, des procédures de purification plus efficaces et par conséquent une meilleure reproductibilité des performances[7,10,11].

Les semi-conducteurs moléculaires, constitués d'une alternance de groupements donneur d'électrons (D) et accepteur d'électrons (A), pour former des structures D-A-D ou A-D-A, ont donné lieu à de bons résultats dans les dispositifs photovoltaïques. Cette stratégie de synthèse permet en effet d'ajuster précisément l'énergie des orbitales moléculaires frontières (FMO pour « Frontier Molecular Orbitals »). En outre, ce type de structures peuvent permettre un meilleur contrôle de l'assemblage moléculaire, indispensable pour un transport de charge efficace, et par conséquent, une efficacité photovoltaïque élevée[3]. Il convient de noter que le transport de charges est un facteur clef qui limite souvent les performances photovoltaïques des cellules solaires organiques.

Une approche possible pour améliorer l'auto-assemblage moléculaire pour un meilleur transport de charge consiste à intégrer des unités planes aux molécules. La structure planaire facilite l'empilement π-π et renforce les interactions intermoléculaires, donnant lieu à une mobilité des porteurs de charge élevée et permettant l'extraction efficace des charges photo-générées dans une cellule solaire[12–14]. En utilisant ces deux stratégies, de nombreux semi-conducteurs moléculaires ont été synthétisés et utilisés dans des dispositifs photovoltaïques. Parmi ceux-ci, des petites molécules en forme d'haltère, qui associent des groupes terminaux planaires riches en électrons à une unité centrale déficiente en électrons, ont permis d'atteindre de résultats prometteurs dans les cellules solaires BHJ[12–15].

Dans ce contexte, cette thèse a porté sur l'étude approfondie d'une série de molécules donneurs d'électrons de forme d'haltère, dont le groupement planaire est l'unité triazatruxène (TAT) et le cœur déficient en électrons le thienopyrroledione (TPD). Les molécules de cette série se différencient par la nature des chaînes alkyles, attachées à l'unité centrale et aux unités TAT. Plus précisément, la relation entre la nature des chaînes latérales et les propriétés moléculaires et thermiques de ces molécules en forme d'haltère ont été étudiées

en détail. L'impact des chaînes alkyles sur la morphologie en film mince à l'échelle nanométrique a également été étudié. Afin de mieux comprendre l'influence de la microstructure des films minces (constitués soit uniquement des molécules donneuses soit de mélanges molécules/fullerènes), le transport de charge dans le plan du film et perpendiculairement au plan ont été mesurées en fonction de la phase (amorphe, cristalline, ...) du matériau. Des cellules solaires BHJ en mélange avec le dérivé de fullerène ont également été réalisées.

Cette thèse fait partie du projet ORION (efficient s**O**luble small molecules fo**R** photovolta**I**c applicati**ON**s). Ce projet multidisciplinaire est réalisé par trois équipes de recherches de Strasbourg. Toutes les molécules étudiées dans cette thèse ont été synthétisées par le groupe de N. Leclerc de l'Institut de Chimie et Procédés pour l'Energie, l'Environnement et la Santé (ICPEES). L'analyse structurale par diffusion des rayons X aux grands angles en incidence rasante (GIWAXS) et petits angles (SAXS) (GIWAXS pour « Grazing-incidence Wide Angle X-Ray Scattering » et SAXS pour « Small Angle X-rays Scattering ») ont été effectuées par le Dr B. Heinrich de l'Institut de Physique et Chimie des Matériaux de Strasbourg (IPCMS).

2. Semi-conducteurs moléculaires à la base de triazatruxene

Les structures moléculaires des molécules étudiées sont illustrées sur la Figure (1). L'unité TAT, donatrice d'électrons, est une unité planaire de symétrie C3. Le caractère planaire de TAT devait favoriser l'empilement moléculaire, et se traduire par un bon transport de charges et de bonnes performances photovoltaïques. Par ailleurs, les unités TAT peuvent être facilement fonctionnalisés par des chaînes alkyles grâce aux trois groupes amines inclus dans sa structure [16]. Cette fonctionnalisation est indispensable pour atteindre une bonne solubilité dans les solvants. L'unité TPD est, quant à elle, un excellent accepteur d'électrons et peut être facilement alkylée, indépendamment des unités TAT. Par conséquent, différentes combinaisons de chaînes latérales ont pu être explorées : soit avec toutes les chaînes alkyles ramifiées 2-éthylhexyl

(EH) (TPD$_{EH}$-TAT$_{EH}$, Figure 1 d)), soit avec uniquement des chaînes linéaires n-octyles (C$_8$) (TPD$_{C8}$-TAT$_{C8}$, Figure 1 a)), soit avec une combinaison des chaînes ramifiées et linéaires (TPD$_{EH}$-TAT$_{C8}$ Figure 1 b) ou TPD$_{C8}$-TAT$_{EH}$ Figure 1 (c)).
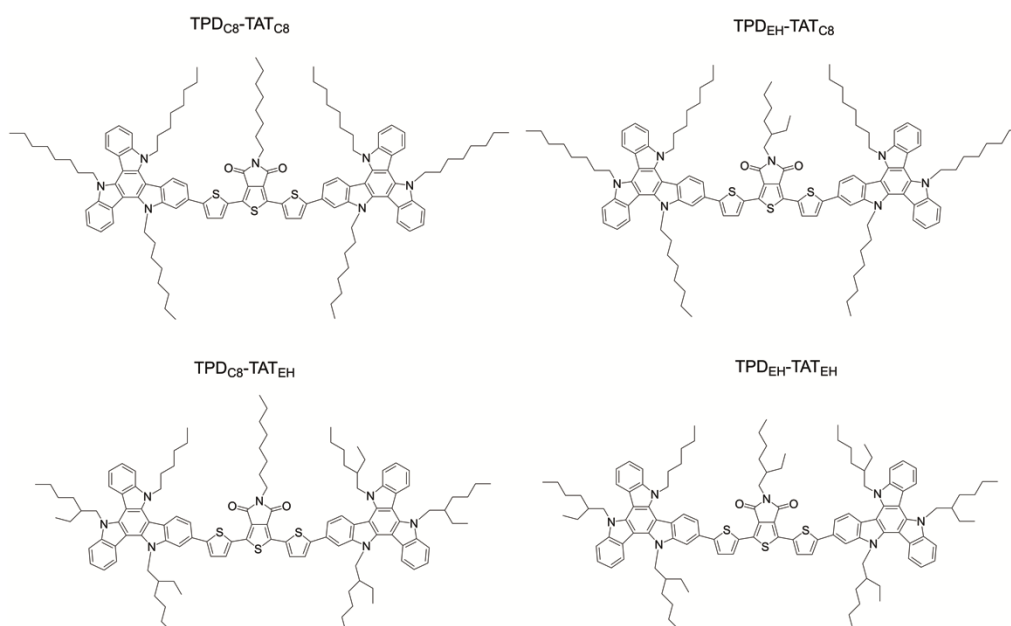

Figure 17: Les structures chimiques des quatre molécules en forme d'haltère étudiées dans cette thèse. a) TPD$_{C8}$-TAT$_{C8}$: avec les chaînes latérales linéaires n-octyle (C$_8$) sur les unités TPD et TAT. b) TPD$_{EH}$-TAT$_{C8}$: avec des chaînes latérales ramifiées 2-éthylhexyl (EH) sur TPD et des chaînes latérales linéaires C$_8$ sur TAT. c) TPD$_{C8}$-TAT$_{EH}$: avec des chaînes latérales linéaires C$_8$ sur TPD et les chaînes latérales ramifiées EH sur TAT. d) TPD$_{EH}$-TAT$_{C8}$: avec les chaînes latérales ramifiées EH sur les unités TPD et TAT.

3. Propriétés des matériaux moléculaires

Tout d'abord, les propriétés électrochimiques ont été analysées par voltampérométrie cyclique (CV pour « cyclic voltammertry »). Ces mesures ont montré que ces quatre matériaux ont des niveaux HOMO et LUMO quasi-identiques situés, respectivement, à - 5,3 et -3,3 eV sous le niveau du vide, ce qui conduit à un « gap optique » de 2,0 eV. Cette valeur est proche du gap optique du P3HT, un polymère de référence.

Les spectres d'absorption mesurés par spectroscopie UV-visible en solution (chloroforme) se chevauchent parfaitement, révélant que la conformation moléculaire et la longueur de conjugaison en solution ne sont pas affectées par les chaînes latérales. À l'état solide, tous les spectres sont déplacés vers rouge et sont élargis. Cependant, les spectres d'absorption de TPD$_{C8}$-TAT$_{C8}$ et de TPD$_{EH}$-

TAT$_{C8}$ sont déplacés plus loin et présentent des pics vibroniques par rapport aux molécules avec des chaînes ramifiées sur les unités TAT. Ces résultats suggèrent que les unités TAT jouent un rôle essentiel dans l'organisation structurale. En effet, lorsque les TATs sont fonctionnalisées par des chaînes linéaires, les interactions intermoléculaires sont plus prononcées (comme en témoigne les pics vibroniques) qu'avec des chaînes EH. En revanche, les chaînes latérales sur l'unité TPD, qu'elles soient linéaires ou branchées, n'influencent pas les propriétés optiques. Cette conclusion a été confirmée en mesurant les propriétés thermiques du matériau par calorimétrie différentielle à balayage (DSC pour « Differential Scanning Calorimetry »). Les molécules ayant des chaînes ramifiées sur le TAT ne présentent qu'une transition vitreuse, tandis que celles ayant des chaînes linéaires présentent des phases cristal-liquide et cristalline.

Par ailleurs, les mesures de diffraction aux rayons X (SAXS), effectuées sur les quatre molécules à l'état solide (poudre), clarifient les relations entre l'auto-organisation et les chaînes latérales attachées aux TAT. Les TAT possédant des chaînes linéaires, adoptent une organisation colonnaire nématique, tandis que les molécules où les TAT ont des chaînes ramifiées restent dans une phase amorphe. Par conséquent, les molécules portant des chaînes linéaires sur les TAT ont des structures moléculaires plus ordonnées et des interactions intermoléculaires plus efficaces, et corollairement, des performances photovoltaïques plus élevées.

4. Morphologie en film mince

Des mesures GIWAXS et des analyses par microscopie à force atomique (AFM) ont également été effectués pour étudier l'organisation moléculaire en films minces, avec ou sans fullerène, en fonction de l'histoire thermique du film. La microstructure des films minces des molécules TPD$_{C8}$-TAT$_{C8}$ est similaire à celle observée en poudre, toute en ayant une longueur de corrélation plus grande.

5. Transport de charge

Pour étudier les propriétés électroniques des molécules TPD-TAT, des mesures du transport de charge ont été effectuées sur des films après dépôt et après divers traitements thermiques. Des transistors organiques à effet de champ (OFET pour « Organic Field-Effect Transistors ») ont été élaborés et utilisés pour mesurer le transport de charge parallèle au plan du substrat, et des diodes Métal/Semiconducteur/Métal dont le courant est limité par la charge d'espace (ou diodes SCLC pour « space-charge-limited-current ») ont été développés pour mesurer le transport de charge perpendiculaire au plan du film. Les mobilités de trous obtenues avec les OFETs dans les films à l'état vitreux sont relativement faibles (de l'ordre de 10^{-4} à 10^{-5} cm^2 V^{-1} s^{-1}) pour toutes les molécules, à l'exception de la molécule TPD$_{C8}$-TAT$_{C8}$, pour laquelle la mobilité mesurée est dix fois plus élevée. De plus, après recuit, les mobilités augmentent d'un ordre de grandeur pour toutes les molécules à chaînes linéaires sur le TAT, et sont en accord avec l'organisation moléculaire plus ordonnée dans l'état cristallin.

Des mobilités SCLC présentent la même tendance. Quelque soit la phase (nématique ou cristalline), le TPD$_{C8}$-TAT$_{C8}$ a une mobilité plus grande que les autres. En plus, les résultats révèlent une anisotropie de transport très marquée, avec des mobilités verticales beaucoup plus grande que des mobilités horizontales. Ainsi, en phase cristalline, la mobilité SCLC pour le TPD$_{C8}$-TAT$_{C8}$ est proche de 10^{-1} cm^2 V^{-1} s^{-1}. Ce résultat figure parmi les valeurs les plus élevées publiées à ce jour dans la littérature sur des semi-conducteurs moléculaires.

Ces observations sont en accord avec les résultats de SAXS et de spectroscopie UV-visible, et confirment que l'empilement des unités TAT renforcent les interactions intermoléculaires.

6. Propriétés photovoltaïques

Les propriétés photovoltaïques ont ensuite été étudiées en utilisant nos molécules en tant que matériau donneur d'électrons en mélange avec un dérivé fullerène (le PC$_{71}$BM) comme l'accepteur d'électrons. Grâce aux excellentes

propriétés de transport de charge (voir ci-dessus), le facteur de forme (FF) des dispositifs photovoltaïques élaborés à partir des molécules portant des chaînes linéaires sur les TAT, était supérieur à 60% et le rendement de conversion a atteint 4 %, une valeur égale à celle obtenue avec le P3HT, le polymère de référence.

7. Conclusion

Dans le cadre de cette thèse, des études approfondies du transport de charge, de l'organisation moléculaire, de la morphologie de films minces et des performances photovoltaïques ont été effectuées sur une série de semi-conducteurs moléculaires composées d'un cœur centrale à base de thienopyrroledione et de deux groupements latéraux à base de triazatruxène (TAT). Les résultats nous ont permis de mieux comprendre la contribution des divers groupements moléculaires sur l'auto-assemblage moléculaires et sur les propriétés optoélectroniques qui en résultent. Nous avons ainsi pu démontrer que, l'impact des chaînes alkyles associées aux unités planaires TAT sur les propriétés d'auto-assemblage prime sur celui des chaînes du groupement central TPD. En d'autres termes, les groupements TAT jouent un rôle déterminant dans l'organisation moléculaire à l'état solide.

Les résultats de l'étude de la mobilité des charges par deux techniques complémentaires confirment l'influence (favorable) des unités TAT sur l'auto-assemblage moléculaire et sur les propriétés opto-électroniques et photovoltaïques qui en découlent. En particulier, une mobilité de trous à l'état de l'art du domaine a pu être atteinte, avec la particularité d'être la plus élevée dans la direction perpendiculaire au plan du film. La collecte des charges au sein d'une cellule photovoltaïque se faisant précisément le long de cette direction, ces propriétés de transport ont donné lieu à des performances photovoltaïques prometteuses.

8. Contribution scientifique

i.   Présentation Poster

1)   <u>T. HAN</u>, B. HEINRICH, I. BULUT, S. MERY, N. LECLERC, P. LEVEQUE, S. FALL and T. HEISER,

Triazatruxene Derivatives as Donor Materials for Bulk Heterojunction Solar Cells, International Research Training Group (IRTG) "Soft Matter Science", Mittelwihr (France), July 2-7th, 2017

2)   <u>T. HAN</u>, B. HEINRICH, I. BULUT, S. MERY, N. LECLERC, P. LEVEQUE, S. FALL and T. HEISER,

Bulk Heterojunction Solar Cells Based on soluble Low Molecular Weight Molecules, Journée Nationale sur l'Energie Solaire (JNES2017), Perpignan (France), June 13-15th 2017

3)   <u>T. HAN</u>, I. BULUT, N. LECLERC, P. LEVEQUE, B. HEINRICH, S. MERY, R. ZIESSEL and T. HEISER,

Triazatruxene Derivatives as Donor Materials for Bulk Heterojunction Solar Cells, Workshop "Science and Technology of Pi-Conjugated Systems" (SPIC 2015), Anger (France), October 12-16th, 2015

4)   <u>T. HAN</u>, I. BULUT, N. LECLERC, P. LEVEQUE, B. HEINRICH, S. MERY, R. ZIESSEL and T. HEISER,

Triazatruxene Derivatives as Donor Materials for Bulk Heterojunction Solar Cells,

13th European Conference on Molecular Electronics (ECME 2015), Strasbourg (France), September 1-5th, 2015

5)   <u>T. HAN</u>, I. BULUT, N. LECLERC, P. LEVEQUE, B. HEINRICH, S. MERY, R. ZIESSEL and T. HEISER,

Triazatruxene Derivatives as Donor Materials for Bulk Heterojunction Solar Cells, MatHero Summer School on organic photovoltaics, Freudenstadt (Germany), August 23-27th, 2015

6) <u>T. HAN</u>, I. BULUT, N. LECLERC, P. LEVEQUE, B. HEINRICH, S. MERY, R. ZIESSEL and T. HEISER,
Triazatruxene Derivatives as Donor Materials for Bulk Heterojunction Solar Cells, Journée Nationale du Photovoltaïque (JNPV 2014), Dourdan (France), December 2-5th, 2014

ii. Présentation Orale

1) <u>T. HAN</u>, B. HEINRICH, I. BULUT, S. MERY, N. LECLERC, P. LEVEQUE, S. FALL and T. HEISER,
Dumbbell-shaped Triazatruxene derivatives as electron donor materials for organic solar cells,

Workshop for condensed materials (JMC15 2016), Bordeaux (France), August 22-26th, 2016

2) T. HAN, B. HEINRICH, I. BULUT, S. MERY, N. LECLERC, P. LEVEQUE, S. FALL and <u>T. HEISER</u>,
Efficient charge transport and high photovoltaic performances using dumbbell-shaped molecules,

International Conference on Science and Technology of Synthetic Metals (ICSM 2016), Guangzhou (China), June 26-July 1, 2016

3) T. HAN, B. HEINRICH, I. BULUT, S. MERY, N. LECLERC, P. LEVEQUE, S. FALL and <u>T. HEISER</u>,
Triazatruxene derivatives as donor materials for bulk heterojunction solar cells PCBM, 11th International Conference on Organic Electronics 2015 (ICOE 2015), Erlangen (Germany), June 15-17th, 2015

iii. Publication

9. Reference

1. Yu, G., Gao, J., Hummelen, J. C., Wudl, F. & Heeger, A. J. Polymer Photovoltaic Cells: Enhanced Efficiencies via a Network of Internal Donor-Acceptor Heterojunctions. *Science (80-.).* **270,** 1789–1791 (1995).

2. Zhao, W. *et al.* Molecular Optimization Enables over 13% Efficiency in Organic Solar Cells. *J. Am. Chem. Soc.* **139,** 7148–7151 (2017).

3. Kan, B. *et al.* A series of simple oligomer-like small molecules based on oligothiophenes for solution-processed solar cells with high efficiency. *J. Am. Chem. Soc.* **137,** 3886–3893 (2015).

4. Zhang, H. *et al.* Developing high-performance small molecule organic solar cells via a large planar structure and an electron-withdrawing central unit. *Chem. Commun.* **53,** 451–454 (2017).

5. Geraghty, P. B. *et al.* High performance p-type molecular electron donors for OPV applications via alkylthiophene catenation chromophore extension. *Beilstein J. Org. Chem.* **12,** 2298–2314 (2016).

6. Cao, W. & Xue, J. Recent progress in organic photovoltaics: device architecture and optical design. *Energy Environ. Sci.* **7,** 2123–2144 (2014).

7. Collins, S. D., Ran, N. A., Heiber, M. C. & Nguyen, T. Small is Powerful: Recent Progress in Solution-Processed Small Molecule Solar Cells. *Adv. Energy Mater.* (2017). doi:10.1002/AENM.201602242

8. Leclerc, N., Chávez, P., Ibraikulov, O. A., Heiser, T. & Lévêque, P. Impact of backbone fluorination on π-conjugated polymers in organic photovoltaic devices: A review. *Polymers (Basel).* **8,** (2016).

9. Etxebarria, I., Ajuria, J. & Pacios, R. Solution-processable polymeric solar cells : A review on materials , strategies and cell architectures to overcome 10 %. *Org. Electron.* **19,** 34–60 (2015).

10. Roncali, J., Leriche, P. & Blanchard, P. Molecular materials for organic photovoltaics: Small is beautiful. *Adv. Mater.* **26,** 3821–3838 (2014).

11. Mishra, A. & Bauerle, P. Small molecule organic semiconductors on the move: Promises for future solar energy technology. *Angew. Chemie - Int. Ed.* **51,** 2020–2067 (2012).

12. Bura, T. *et al.* High-Performance Solution-Processed Solar Cells and Ambipolar Behavior in Organic Field-Effect Transistors with Thienyl-BODIPY Scaffoldings. *JACS* 2–5 (2012).

13. Bulut, I. *et al.* Thiazole-based scaffolding for high performance solar cells. *J. Mater. Chem. C* **4,** 4296–4303 (2016).

14. Bulut, I. *et al.* LUMO's modulation by electron withdrawing unit modification in amorphous TAT dumbbell-shaped molecules. *J. Mater. Chem. A* **3,** 6620–6628 (2015).

15. Huaulmé, Q., Cece, E., Mirloup, A. & Ziessel, R. Star-shaped panchromatic absorbing dyes based on a triazatruxene platform with diketopyrrolopyrrole and boron dipyrromethene substituents. *Tetrahedron Lett.* **55,** 4953–4958 (2014).

16. Li, X.-C., Wang, C.-Y., Lai, W.-Y. & Huang, W. Triazatruxene-based materials for organic electronics and optoelectronics. *J. Mater. Chem. C* **4,** 10574–10587 (2016).